Université de Toulouse

THÈSE

En vue de l'obtention du

DOCTORAT DE L'UNIVERSITÉ DE TOULOUSE

Délivré par :

Université Toulouse 3 Paul Sabatier (UT3 Paul Sabatier)

Présentée et soutenue par :

Thomas LORNE

Le mardi 12 décembre 2017

Titre :

Contribution of inelastic neutron scattering to the characterization of the grafting of fluorophores onto double-walled carbon nanotubes

---

ED SDM : Sciences et génie des matériaux - CO034

Unité de recherche :

CIRIMAT - ILL

Directeur(s) de Thèse :

Emmanuel Flahaut (Directeur)
Mónica Jiménez-Ruiz (Co-directrice)

Rapporteurs :

Jean-Louis Bantignies
Marie Plazanet

Autre(s) membre(s) du jury :

Montserrat Gómez-Simon
Jean-Marc Escudier
Lucyna Firlej

Acknowledgements

Comme pour la plupart des projets, une thèse ne se réalise pas seul. Et, bien souvent, la réussite d'un travail tient aussi aux personnes qui y participent, qui nous soutiennent et qui nous entourent. C'est pourquoi j'aimerais remercier toutes les personnes qui ont participé, de près ou de loin, à la réussite de ce projet.

J'aimerais tout d'abord remercier mes encadrants Mónica Jiménez-Ruiz et Emmanuel Flahaut pour leurs conseils, leurs corrections et le temps qu'ils m'ont accordé quand j'en avais besoin. J'aimerais remercier particulièrement Mónica qui a été très présente durant les moments les plus difficiles de cette thèse, et qui a su me donner le soutien nécessaire pour surmonter les obstacles rencontrés. Merci également aux membres du jury, Jean-Louis Bantignies, Marie Plazanet, Montserrat Gómez-Simon, Jean-Marc Escudier et Lucyna Firlej, pour avoir accepté d'évaluer mon travail, et de l'avoir fait avec bienveillance. Merci aussi à toutes les personnes qui m'ont aidé sur des parties plus spécifiques de mes travaux, Stéphane Rols, Jean-Marc Escudier, Corinne Payrastre, Jean-Louis Bantignies, Rozenn Leparc, Mohammed Zbiri, Juan Rubio-Zuazo et Miguel Angel Gonzalez, pour leurs contributions essentielles à la réalisation de ce travail. Merci ensuite aux hommes de l'ombre, Pierre Lonchambon, Alain Bertoni, Simon Baudoin et Raymond Aznar pour leurs compétences techniques et leur aide précieuse tout au long de ces trois années. Un grand merci bien sûr à mes collègues de travail, Jean-François Guillet, Cyril Sarrieu, Martin Boehm et Nikolaos Biniskos, pour leur soutien moral, et les discussions riches et parfois très drôles que nous avons eues. Et enfin, merci à toute ma famille et tous mes amis, pour leur soutien inconditionnel durant cette thèse, mais aussi depuis mes plus jeunes années.

Contents

List of Figures

List of Tables

À mon grand-père, Anicet Freissinier

Chapter 1

Introduction

1.1 Nanomaterials : General introduction

Contrary to what one might think, the use of Nanomaterials is not new in mankind's history. Indeed, according to literature the usage of nanomaterials dates back to traditional Chinese medicine [1] and, Mayan [2] and medieval painting [3]. Nanomaterials such as colorful inks made of colloid-sized gold nanoparticles were, for example, used in artistic applications such as the famous Lycurgus cup [4] (Figure 1.1-a and -b). Even carbon nanotubes have been found in the steel of ancient Damascus blades that may explain the exceptional mechanical properties of these materials at that time and has been the object of a Nature publication in 2006 [5] (Figure 1.1-c). Back then, of course craftsmen were not aware of the existence of a nanoscale, but by empirically optimizing their processes, they ended up making the firsts man-made nanomaterials.

Nevertheless, we had to wait until the 1950's and Richard Feynman's famous talk entitled "There is Plenty of Room at the Bottom", where he established the possibility to build materials atom by atom [6], to hear for the first time the first words on what later became known as Nanotechnology. Eventually, it was with the discovery of the fullerenes [7], and the possibility to characterize and synthesize them, by Richard Smalley *et al.* in 1985 that the concept of nanomaterials became a reality. Ever since, there is a real effort

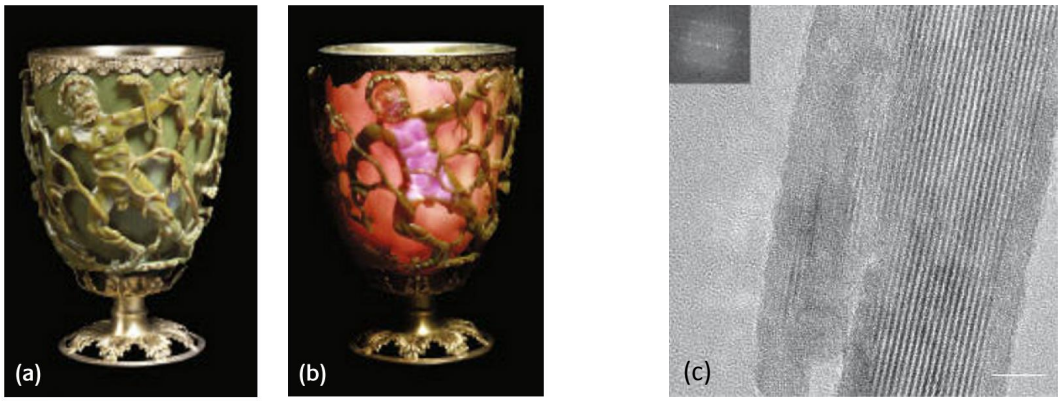

FIGURE 1.1: *Pictures of the Lycurgus cup in reflected (a) and transmitted (b) light [4]. And (c), high-resolution transmission electron microscopy image of carbon nanotubes in a genuine Damascus sabre [5].*

from the scientist community to conquer this nano-scale world.

Indeed, in the size range below 100 nm the materials we know from bulk behave very differently and offer a large amount of possibilities in terms of resulting properties. First because multiple atoms or molecules behave differently from individual ones; larger size results in different behaviors in collisions with atoms. Secondly, because increasing the number of atoms in a system includes perturbations of the atomic energy levels leading to energy bands with fine structures [8]. Indeed, below 100 nm size the emergence of the effects of quantum confinement modifies the energy spectra of the materials and leads to new electrical, thermal and optical properties. For example, Charles H. Olk and Joseph P. Heremans have shown experimental evidence that the outstanding electrical properties of carbon nanotubes (CNTs) were diameter dependent and were consistent with a density of states containing Van Hove-type singularities due to quantum-confinement [9]. Finally, another very important feature of nanomaterials is that they present a very high specific surface area. This implies that they have a very high fraction of their atoms at the surface and these atoms act very differently from the ones located in the bulk of a material [10]. Indeed, the atoms at the surface own

a higher energy and, therefore, the integrated energy of those atoms provides a surface tension that changes the mechanical, electrical and thermal properties as well as the way these nanomaterials interact with their environment. Looking at the particular features mentioned above it is easy to understand why there has been such a growing interest for making new materials at the nanoscale over the past decades. It is therefore not surprising that they have found, nowadays, applications in many fields such as Materials science, Biotechnology, Energy storage, Microelectronics, Nanomedicine, etc. For example, carbon nanotubes are commonly used for mechanical reinforcement of composite materials (Figure 1.2-a and -b) and progresses in that field allow good compatibility with a large variety of polymer matrices, as it has been summarized by J.N. Coleman *et al.* in 2006 [11], and even for other types of matrices such as metals [12] or ceramics [13].

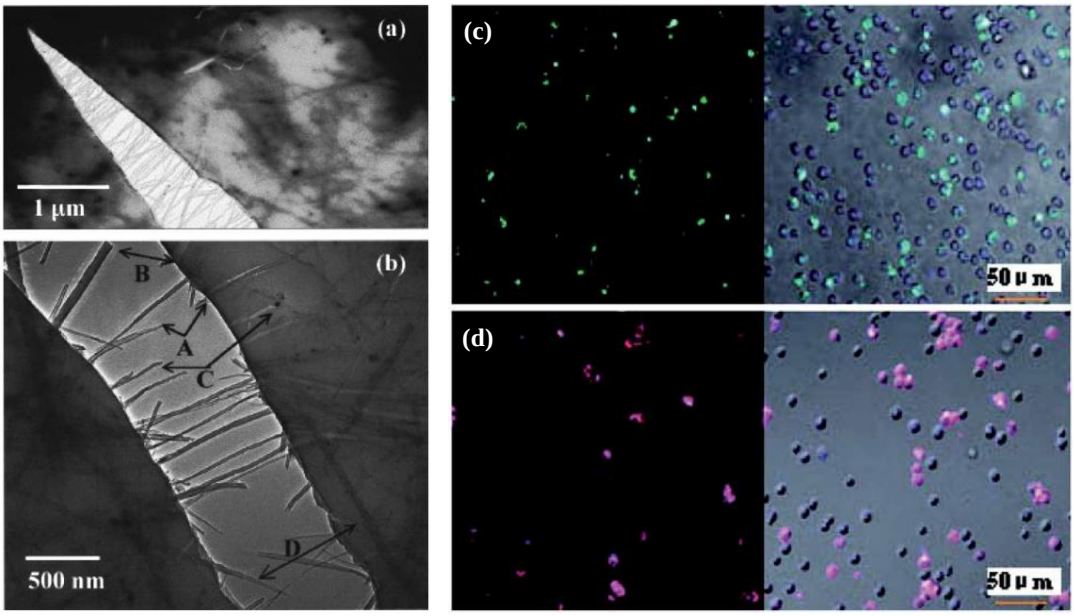

FIGURE 1.2: *(a) and (b) are in situ observations of crack nucleation and propagation in CNTs reinforced polystyrene (PS) composite thin films. The presence of the CNTs (A-D arrows) allowed an increase in tensile strength for the PS of about 3 MPa [11]. (c) and (d) are confocal microscopy images of aptamer-conjugated dye-doped silica nanoparticles in a mixture of three different cells allowing to sort the cells via molecular recognition [14].*

Various Nanomaterials are also used as biosensors for molecular recognition (Figure 1.2-c and -d) or signal transductions [14, 15] for bioanalysis, and are studied in order to develop more selective ways to deliver drugs by using them as carriers targeting specific cells within tissues [15–18]. Concerning research on energy storage, the surface properties of the nanomaterials described above make them good candidates for fast reversible storage processes and very different types of compounds (carbon-based, metal oxides, polymers, etc.) are studied [19–23]. Eventually, nanomaterials find as well applications in electronic devices or information storage [24] where their use allows for example to make flexible or transparent transistors [25, 26], to enhance the charges transport inside semiconducting materials or to develop new fast-making processes for the microelectronics industry such as inkjet printing or spray-coating [27–29] (see figure 1.3).

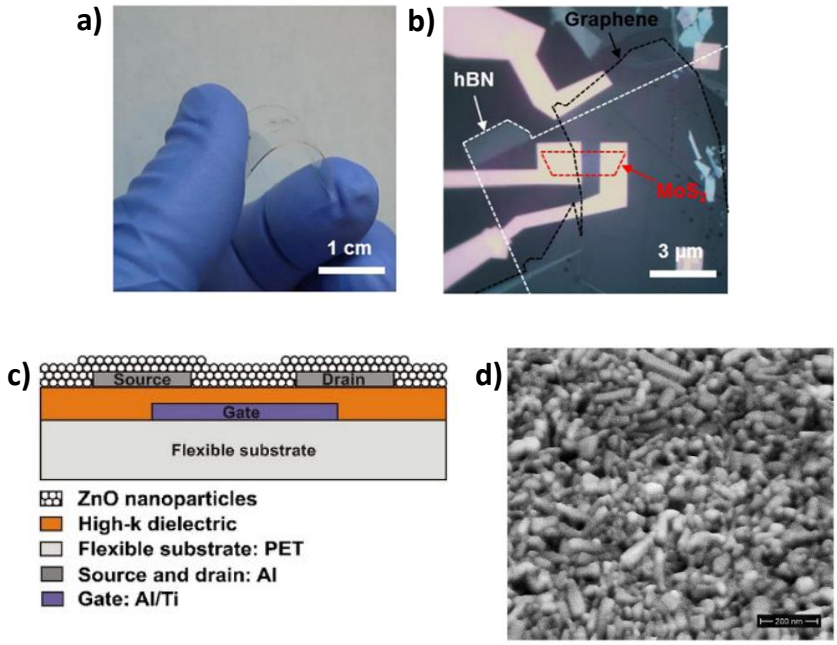

FIGURE 1.3: *(a) Photograph of a flexible and transparent MoS_2 field-effect transistor device. (b) Reflection-mode optical micrograph of the same flexible and transparent device [26]. (c) Schematic of a ZnO nanoparticle-based spray-coated transitor. (d) Scanning electron microscope images of the ZnO nanoparticle-based spray-coated layer [29].*

Many of the properties described above are based on the high specific surface area of the nanomaterials, that make them systems with a total energy generally higher than their corresponding bulk materials. If this higher energy is a major asset in terms of resulting properties, it is at the same time a major drawback in terms of stability. Indeed, all systems have a tendency to minimize their total energy and, an easy way to do it in the case of nanomaterials is often to reduce their surface tension by agglomerating/aggregating over time, losing consequently the properties related to their high specific surface area. One of the common way to overcome this issue is through the functionalization of the surface of the nanomaterials in order to maintain their dispersion and homogeneity.

1.2 Functionalization of nanoparticles

The functionalization of nanoparticles is actually the cornerstone of the development of nanotechnologies. First of all because, as we mentioned previously, the properties of such materials result directly from the individualization of these nanoscale objects, individualization that requires to overcome their natural tendency to agglomerate. Then, because the vast majority of the applications deriving from these outstanding properties implies interactions with other types of materials (*e.g.* other nanoparticles, matrix, layers, molecules, etc.) in order to be integrated in larger size devices. And finally, because the functionalization is also one way of tuning and monitoring the intrinsic properties of nanoparticles. We distinguish nowadays two different approaches for these purposes: the non-covalent functionalisation and the covalent functionalization of the nanoparticles.

One of the many goals driving the study of the functionalization of nanoparticles is thus to prevent their agglomeration, improving their individualization and consequently maintaining their outstanding properties within a material or a device. Concerning the non-covalent functionalisation, lots of studies have demonstrated that the use of surfactants for non-covalent functionalization of nanoparticles provides very stable and homogeneous dispersions in common solvents, including water. Stable suspentions of CNTs have thus been obtained by compensating the effects of attracting weak interactions with ionic surfactants such as sodium dodecyl sulfate (SDS) [30], dodecylbenzene sodium sulfonate (NaDDBS) [31], and other types of surfactants [32, 33]. Literature also shows that covalent functionalization can be used for dispersion stability improvement. For instance, the covalent functionalization of silica nanoparticles with amino-terminated alkoxysilan, poly(ethylene glycol)-terminated alkoxysilan or oleic acids have shown strong evidence of dispersion stability improvement [34, 35] (see figure 1.4).

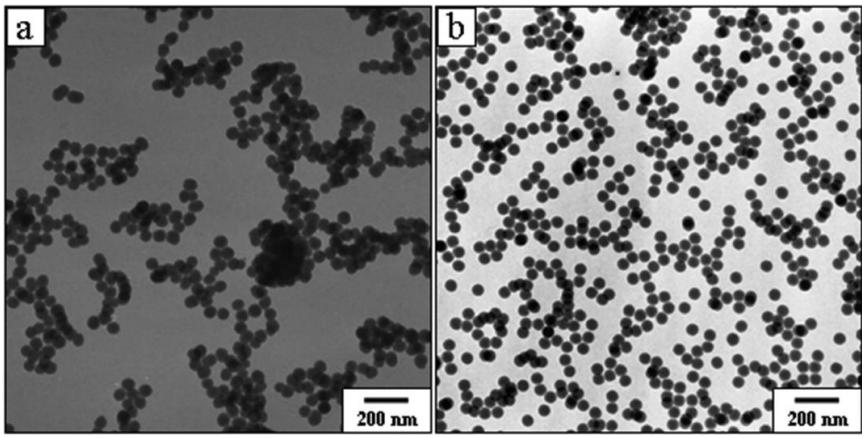

FIGURE 1.4: *Transmission electron microscopy images of (a) non-functionalized, (b) aminopropyltrimethoxilane functionalized silica nanoparticles, illustrating the effect of the covalent functionalization on the dispersion of the particles [34].*

Another important aspect of the functionalization in the literature is to ensure the good compatibility of the nanoparticles when integrated in devices or materials. The aim of this type of functionalization is often twofold. First

it plays the role of interface between the nanoparticles and any other type of materials of interest that would not be naturally compatible, but it also ensures that the nanoparticles keep their properties once integrated in more complex systems. For example, the effective use of carbon nanotubes in composite applications strongly depends on the ability to disperse the NTs homogeneously throughout the matrix without destroying their integrity [36] (see figure 1.5). Good interfacial bonding is required to achieve load transfer across the CNT-matrix interface, a necessary condition for improving the mechanical properties of polymer composites [37–39].

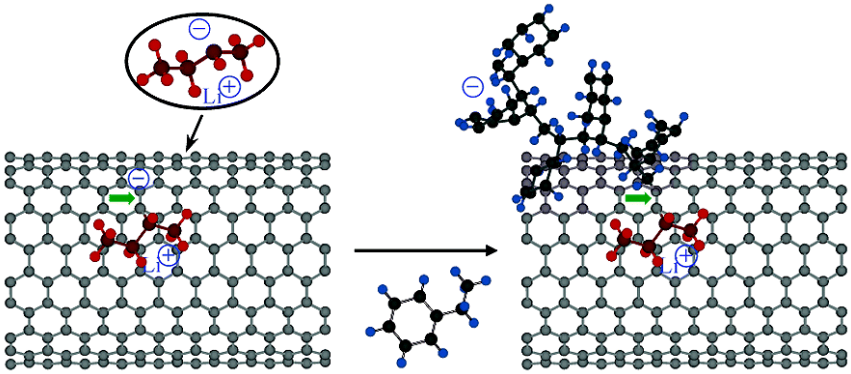

FIGURE 1.5: *Schematic of In Situ Synthesis of Polystyrene-Grafted Single-Wall Nanotube Composites using carbanions interfacing the polymer matrix and the nanotubes, allowing to preserve the integrity of the SWNTs [36].*

Finally, the studies on the functionalization of nanoparticles present also a strong interest concerning the modification of the nanoparticles properties. Indeed several studies report the tunability or the enhancement of the original nanoparticles properties, or even the emergence of new properties through their functionalization. For example, in 2005, Kolmakov *et al.* functionalized SnO_2 nanowires with Pd nanoparticules for gaz sensing application. They discovered an enhancement of the exchanges on the SnO_2 nanostructure surface, increasing the sensivity of the sensor, promoted by

the catalytically-active Pd nanoparticles [40]. In 2011, del Carmen Giménez-López *et al.* have evidenced that when encapsulated, single-molecule magnets inside nanotubes underwent a large degree of orientational ordering, and the magnetic guest molecules influenced the electrical resistance of the host nanotubes [41].

Due to their outstanding properties and the tremendous effort made in improving their functionalization in order to find new applications, the popularity of nanomaterials kept on increasing for the past decades and they are nowadays a major actor in materials science. This increase of both popularity and, consequently, new applications came with the beginning of their large scale production. As they are today more and more used in state-of-the-art materials and devices, and are already used in many consumer products [42], the questions of their toxicity and their potential impact on health and environment inevitably raised within the scientific community.

1.3 Toxicity of nanomaterials

The rapid expansion of nanotechnology promises to have great benefits for society, yet there is increasing concern that human and environmental exposure to manufactured nanomaterials may result in significant detrimental effects. We could wonder why such materials raised questions about their potential impact on health and environment. First of all, the very basic definition of a nano-object is to have at least one of its dimension in the range below 100 nm. Objects of this size can easily cross the physiological barriers of any living being and may be able to penetrate into cells, or even into their nuclei. It is even because of this specific property that they stand as excellent candidates for targeted drug delivery. Then, as it has been already discussed

previously, they exhibit new outstanding properties that are not yet fully understood or discovered, and these properties can be changed when they interact with other types of materials or molecules. These latter facts make their behavior very difficult to predict when they interact with a complex environment (e.g. inside human body, inside living cells, in aquatic media, etc.) and could lead to potential harmful effects on living beings by interfering with biological processes. Finally, and with respect to the previous points, we witnessed a huge increase in interest, studies, publications and new applications related to the nanomaterials over the past decades. In particular since 2000 (see figure 1.6), and their large scale production, nanomaterials became easier and easier to produce, increasing the risk of finding these materials in contact with the public and/or to be released, at some point along their life cycle into the environment.

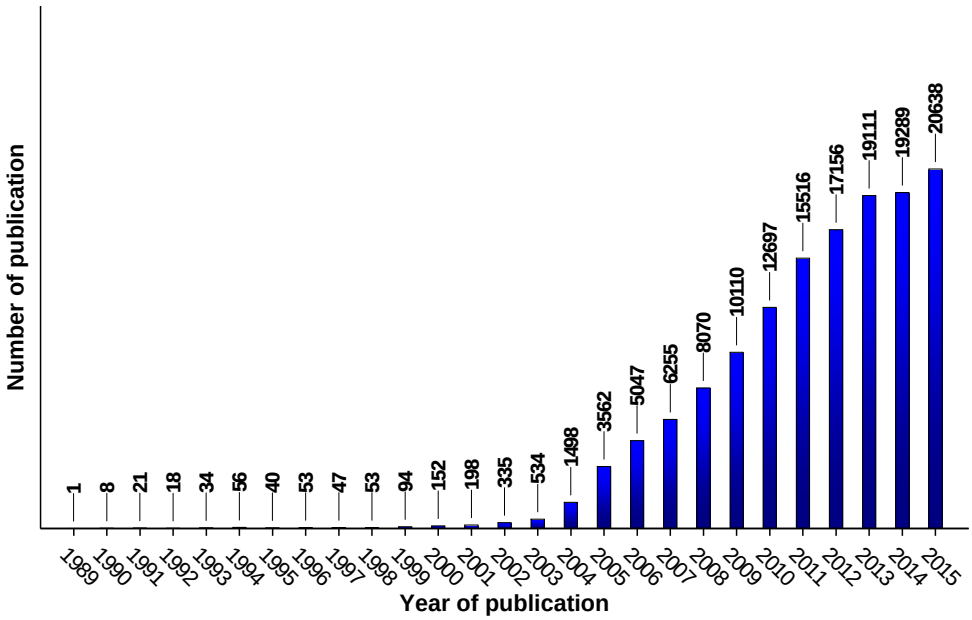

FIGURE 1.6: *Evolution of the number of scientific publications in between 1989 and 2015 (using the keyword "nanomaterials" on the website PubMed.org specialized in Biomedical and Life Science literature).*

Nevertheless the question of the toxicity of nanomaterials is a very complex one, and is still today at the center of a vigorous debate. To begin with,

there is a lack of rules and regulations surrounding the use and the production of nanomaterials. The European Union (E.U.), encouraged by France, is leading the joint endeavor to establish a coherent regulation around this delicate topic. In 2006, the "Agence française de sécurité sanitaire de l'environment et du travail" (Afsset) produced a first public report [43] inventoring the different types of known nanomaterials and their corresponding potential risks. This report paved the way toward a better evaluation of the nanomaterials hazards and encouraged the research effort on the topic. In 2010, the ministers and representatives of member states in the European region of the World Health Organization (WHO) included nanomaterials in the «key environment and health challenges of our time», in the Parma Declaration on Environment and Health [44]. In 2014, the french "Agence nationale de sécurité sanitaire de l'alimentation, de l'environnement et du travail" (Anses), based on the previous work of the Afsset, presented a report [45] updating the knowledge on the risks related to nanomaterials, and advising their inclusion in the "registration, evaluation, authorisation and restriction of chemicals" (REACh) E.U. regulation. Despite the many attempts to improve the safe handling of nanotechnology, there is still considerable doubt and uncertainty on this very hot topic, and there is still no definitive framework set up for their regulation.

First of all because the effectiveness of specific frameworks such as REACh is still discussed [46, 47], slowing down the implementation of such regulation frameworks. Then, because to fully understand the impact of a specific nanomaterial over its whole life cycle requires a large amount of studies (and therefore a tremendous amount of time and money), while on the other hand the number of new nanomaterials keeps on increasing, making very hard for the toxicity studies to catch up. Finally, because the toxicity studies sometimes end up with contradictory conclusions, leaving the scientific community not able to find a consensus on the matter.

In order to illustrate all the complexity depicted in the previous remarks, lets focus, as an example, on the case of one of the most widely used nanoparticles: the Titanium dioxide (TiO_2). The TiO_2 nanoparticles find nowadays many applications in various domain, such as pearlescent or "metallic" paint formulations used in cosmetics, hard coatings, plastics, and self-cleaning additives for porcelain, ceramics, and specialty coating [48]. Other TiO_2 applications include filters that exhibit strong germicidal properties and remove odors, and TiO_2 has been used in conjunction with silver as an anti-microbial agent [48]. Furthermore, due to its photocatalytic activity, TiO_2 has also been used in waste water treatment [49]. Finally, it is a common additive in many food [50] personal care, and other consumer products [51] (known as the additive E171). One very concerning use of the TiO_2 nanoparticles is in commercial transparent sunscreen protections, because of its capacity to absorb UV light although remaining transparent to visible light [48]. When used in such conditions, the TiO_2 nanoparticles are in direct contact with the human skin but don't seem to penetrate the body through an intact (undammaged) epidermis (see figure 1.7) [52, 53].

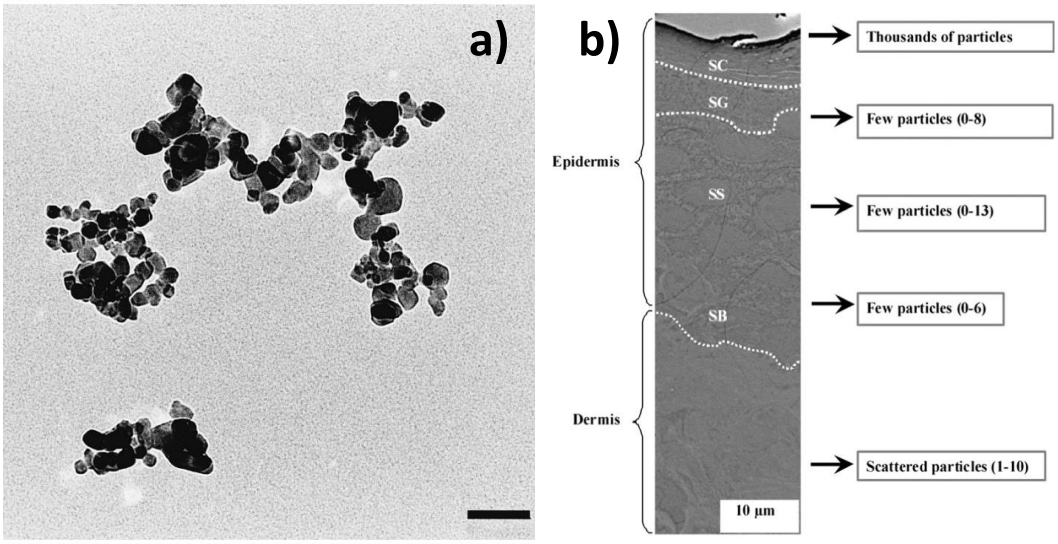

FIGURE 1.7: *(a) TEM image showing the morphological aspects of the particles of TiO_2 found in sunscreen commercial products (Bar = 100 nm) [52]. (b) Representation of TiO_2 particle distribution in different layers of minipig abdominal skin (longitudinal slice of skin), showing the results from the cross section analysis of each skin layer. Numbers in parentheses are estimates of the numbers of TiO_2 particles observed in each layer, 24h post-exposure to the product. [53].*

Nevertheless, this type of products are often sprayed and released in the air, and are very likely to end up in the water after the users bathed in the seas or rivers. Yet, many data suggest that TiO_2 nanoparticles could be absorbed through respiratory tract, digestive tract and damaged skin, into the body and distributed in organs such as lungs [54, 55], lymph nodes [56], liver [55, 57], kidneys [55] and the brain [58] (see figure 1.8). As we know, nano-TiO_2 has to travel along the body within blood before reaching at target organs. However, there is still today no regulation concerning the permitted use of this nanomaterial. Furthermore, when we look specifically at the literature concerning the toxicity of the TiO_2 nanoparticles, we find both studies evidencing their toxicity [59, 60] and studies evidencing the absence of toxicity [61–63]. Eventually, even by comparing only the studies demonstrating the toxicity of the nano-TiO_2 we see that it is very hard to find a consensus about the parameter on which depends its impact on health or environment. Indeed, some studies define its toxicity to be size-dependent [58, 64–66] while

some others conclude that the toxicity of this nanomaterial is rather depending on its crystal structure [67–69].

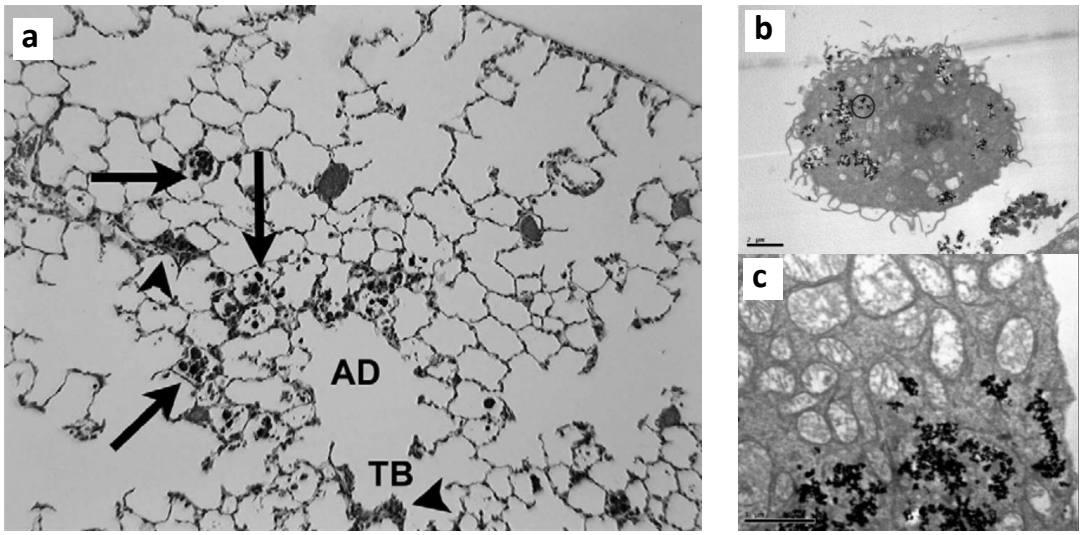

FIGURE 1.8: *(a) Light micrograph of lung tissue of a rat exposed to TiO_2 nanoparticles at 3 months after exposure. This micrograph demonstrates accumulation of TiO_2 -containing macrophage aggregates (arrows) [54]. (b) microspcopy image of a brain macrophage within 18 h postexposure to TiO_2. We see multiple vacuoles containing TiO_2 aggregates. (c) higher magnification of (b) showing swelling and disruption of mitochondria in close proximity to the aggregates [58].*

Other types of nanoparticles that happened to be more and more used in state-of-the-art materials and devices for the past decades, are the carbon nanotubes [70]. Of course in the case of carbon nanotubes the situation is less complex because there are applications neither in the food industry (although it may be possible for food packaging) nor in cosmetics (to the best of our knowledge), so a direct contact with consumers seems, for the moment, rather limited. However, for the same reasons why apparently contradictory results are published for TiO_2 nanoparticles because their shape, surface chemistry, crystal phase, dispersion protocol and animal/cell models and exposure conditions usually vary from one study to another, the literature dealing with the toxicity of CNTs is also difficult to properly analyse. We will now introduce basics about carbon nanotubes before discussing again later toxicity of CNTs in particular.

1.4 Carbon nanotubes

In the landscape of nanomaterials, the CNTs own a special position. Indeed, since their discovery in 1991 by Iijima [71], and their first synthesis in 1993 by Bethune *et al.* [72] and Iijima *et al.* [73], CNTs have evolved into one of the most intensively studied nanomaterials. They are held in part responsible for launching the nanotechnology revolution and have had motivated both fundamental scientists and engineers interested in applications due to the unique combination of their properties.

First, these molecular systems are nanometer-sized in diameter, but up to centimeters long, yielding an unprecedented length/diameter aspect ratio. Carbon nanotubes can be thought of as narrow strips of graphene rolled up into seamless tubes (figure 1.9). They form spontaneously and efficiently under well-defined conditions either as single-wall nanotubes (SWNTs) or multiwall nanotubes (MWNTs). Under tension, nanotubes are two orders of magnitude stronger than steel at 1/6th of the weight. The melting point of nanotubes have been calculated from computer simulations to be about 4000 K in "ideal vacuum" [70]. Depending on the atomic structure of nanotubes, including diameter, single-wall nanotubes act as ballistic conductors of electrons or show semiconducting behavior [74, 75]. Carbon nanotubes seem to be also excellent conductors of heat [76].

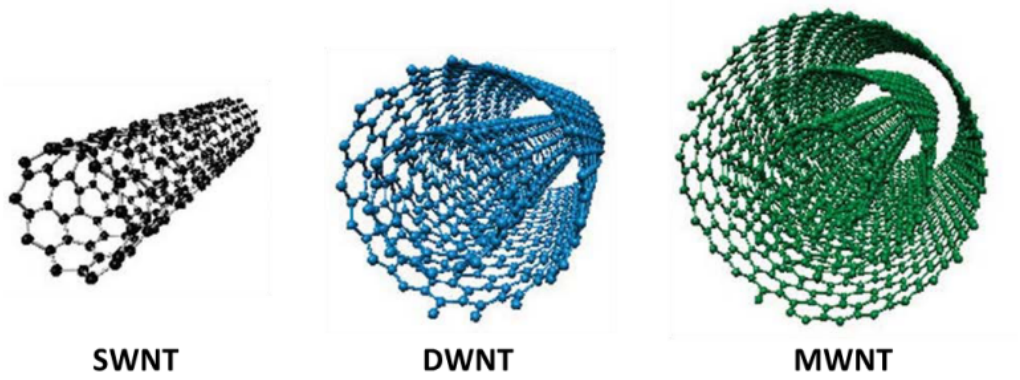

FIGURE 1.9: *Representation of the main categories of carbon nanotubes. The single-walled (SWNT), the double-walled (DWNT) and the multi-walled (MWNT) carbon nanotubes.*

The SWNTs usually have diameters comprised between 0.4 and 2.5 nm [77]. The MWNTs are constituted of several concentric tubes, and their number can vary from 2 to 50 concentric tubes. We usually distinguish the double-walled carbone nanotubes (DWNTs), owning only two walls, from the MWNTs (figure 1.9). The MWNTs present inner and outer diameters comprised respectivelly between 0.5 and 50 nm, and between 1.2 and more than 100 nm. The distance in between the walls of the MWNTs is equal to 3.4 Å [78, 79], which corresponds to the distance between the layers of graphene constituing the graphite. SWNTs and DWNTs have a tendency to naturaly form bundles that can reach a size in diameter above 30 nm and a length of several micrometers, and in some cases up to the order of the centimeter. The MWNTs often tend rather to form disorganized tangles.

Nevertheless, as peculiar as they can be, compared to the rest of the nanomaterials, carbon nanotubes are no exception to the rule: on the one hand, their functionalization have been widely studied leading to several application in several domains [10] and, on the other hand, the question of their toxicity is as well at the center of the current debate on the nanotoxicity [80].

1.4.1 Functionalization of carbon nanotubes

As for any other type of nanoparticles, we find two ways of functionalization for the CNTs: the covalent functionalization and the non-covalent one. The covalent functionalization allows to graft molecules to the outer walls and to the tips of the nanotubes *via* the creation of a strong bond (covalent bond). The formation of such bond modifies the structure of the CNT and therefore its properties. This is often the reason why the DWNTs are used instead of SWNTs, indeed they allow to use their outer walls for the covalent grafting of molecules while their inner wall remains unchanged and maintain its properties. The non-covalent functionalization, on the other hand, is based on weak interactions ($\pi - \pi$, Van der Waals, hydrophobic, ionic, etc.) that have no impact on the structure of the CNTs [81] while it can still impact the properties of the CNTs [82].

Covalent functionalization

We can distinguish different categories of covalent functionalization depending on the chemical reactions involved in the grafting process.

Esterification-amidation. This type of functionalization requires to use CNTs that own carboxyl (-COOH) groups at their surface, usually achieved prior to the grafting *via* their oxidation. The direct reactions between the carboxyl groups and the alcool/amide groups that forms esters/amides groups are slow and reversible. Nevertheless, when the carboxyl groups are first turned into acyle chloride groups the reactions are fast and non reversible. This is why the functionalization by means of esterification/amidation always requires a first "activation" step using either thionyle chloride or oxalyle chloride, before addition of the alcool or the amine to graft (see figure 2.2). Tao et al. [83] functionalized this way MWNTs with a poly(amidoamine) and deposited afterwards silver nanoparticles that have been visualized by

TEM (see figure 2.2). With the same process Gul et al. [84] grafted a diamine, the 2-(2-aminoethoxy)ethoxy)ethanamine, before to graft a fluorophore, the fluorescein isothiocyanate (FITC), on the diamine and therefore were able to track the CNTs in *in vitro* experiments. Singh et al. [85] functionalized SWNTs and MWNTs with other types of polyamines (putrescine, spermidine, spermine) in order to graft afterwards siRNA. Delgado et al. [86] succeeded to graft fullerenes owning amine groups onto oxidized SWNTs extremities. Finally, biological molecules such as enzymes [87] or DNA [88], can also be grafted on CNTs by means of this process.

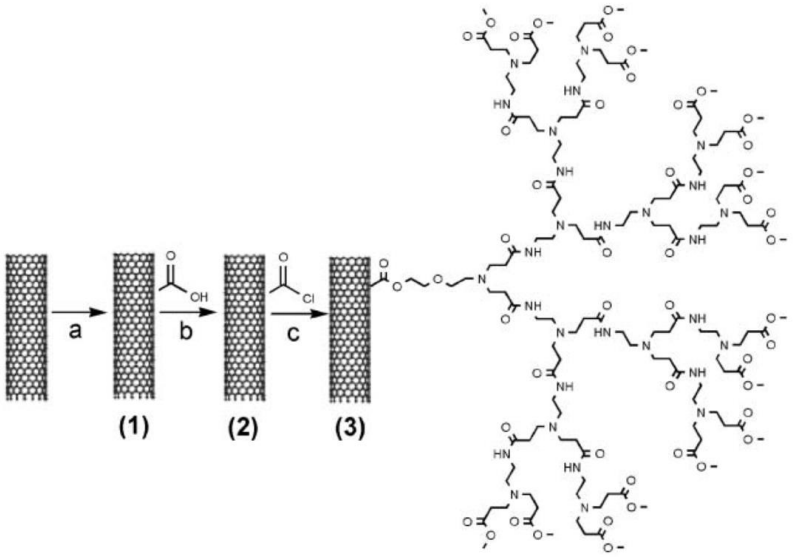

FIGURE 1.10: *Example of the grafting of poly(amidoamine) dendrons on MWNTs using the amidation functionalization process with previous carboxyl groups activation [83]. 3-steps process with: 1) the oxidized, 2) the activated, and 3) the functionnalized MWNTs.*

Halogenation. Another approach to graft molecules onto CNTs can be *via* halogenation. For instance, the fluoration of walls of CNTs increase their reactivity allowing the grafting of amines [89] or alkyles. Fluorated SWNTs have been thus obtained using different techniques [90, 91]. Same for the DWNTs where several techniques have been studied [92, 93].

Cycloaddition. The cycloaddition allows to create pyrrolidine cycles on the CNTs walls by the reaction of a 1,3-dipolar compound (generally azomethine ylides) on a dipolarophile (6-carbon rings of the CNTs, for instance). Bianco et al. [94] functionalized MWNTs with a diaminotriethyleneglycol chain with this 1,3-dipolar cycloaddition process (Figure 1.11). They also grafted anti-cancer and antifungal molecules such as the methotrexate [95] and the amphotericine B [96]. We find also other types of cycloaddition that have been perfomed on CNT [97–100].

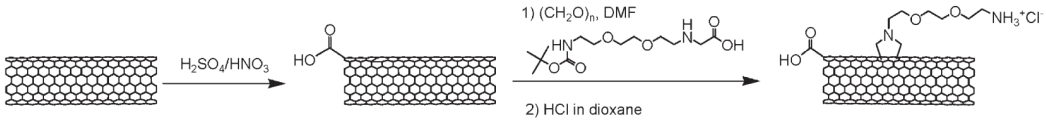

FIGURE 1.11: *Example of the functionalization of MWNTs with a diaminotriethyleneglycol by means of 1,3-dipolar cycloaddition [94].*

Free-radical addition The free-radical addition is a method widely used because of its simplicity and efficiency. The common way to perform it is to use diazonium salts which are very unstable and turn easily into radical intermediates that spontaneously react with the carbon atoms constituting the CNTs. Tour et al. [101] were the first to describe this type of functionalzation on CNTs using aryldiazonium salts. Later this same team improved the process by adding ionic liquids and potassium carbonate [102]. Ménard-Moyon et al. [103] developed a method of triple functionnalization using this process that allows to graft afterwards three different molecules with different functions on the same CNTs : Antibodies targeting, treatment of the targeted disease and marking of the CNTs for imagery purposes.

Non-covalent functionalization

This second way of functionalizing the CNTs is as well quite studied and commonly used. We find various types of non-covalent functionalization in the literature.

Surfactant and polymers. Examples of non-covalent functionalisation of CNTs using surfactant for dispersion purposes have been described earlier in the chapter 1.2. Similarly, several examples of functionalization of CNTs with polymers in order to make nanocomposites materials can be found as well in the chapter 1.2.

Polycyclic aromatic compounds. The Polycyclic aromatic compounds owning an hydrophilic or hydrophobic function can help the dispertion of the CNTs. One of the most widely used molecules is thus the pyrene and its derivatives. Indeed, the pyrene is able to be adsorb on the walls of the CNTs (see figure 1.12). For instance, Baek et al. [104] used pyrene derivatives, owning carboxyl and amine groups to fix DNA molecules on SWNTs, to make biodetectors (Figure 1.13). Salice et al. [105] fixed gold nanoparticles onto SWNTs *via* the use of pyrene molecules presenting a carbon chain containing a thiol group (-SH). The fluorescent molecules are as well good candidates for non-covalent grafting onto CNTs. One of the most commonly used fluorophore, because of its very low cost, is the fluorescein isothiocyantate (FITC). We find then examples of oxidized SWNTs that were functionalized with FITC molecules simply adsorbed [106, 107]. The goal was not to improve the dispersion of the nanotubes, but to mark them in order to be able to easily track them in *in vivo* studies. Finally, we find also examples of aromatic medicines that were adsorbed onto the CNTs [108–111].

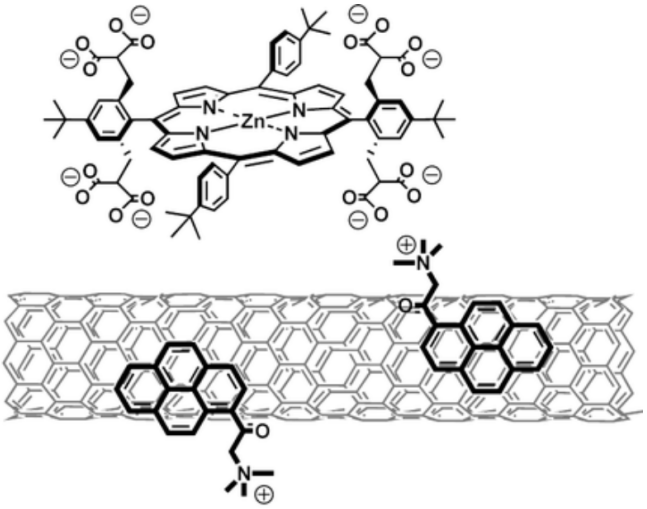

FIGURE 1.12: *Example of non-covalent functionalization of NTCs using pyrene molecules adsorption to connect with porphirin derivatives [112].*

Biomolecules. In order to use the CNTs for biological applications, the interactions of the latter with different biomolecules such as proteins, nucleic acids, carbohydrates and lipids have been studied. For example, proteins were used for the CNTs dispersions in water [113–115]. We find also studies that used single-stranded DNA to perform the dispersion of the NTCs [116–118].

Encapsulation

Another form of non-covalent functionalization of the CNTs is also performed by encapsulating molecules inside the nanotubes. Indeed once they are opened the CNTs can by filled by different types of compounds. A famous example of encapsulation is attributed to Khlobystov et al. [119] after succeeded at filling SWNTs with fullerenes C_{60}. We also find in literature several examples of medicines encapsulated in the CNTs [120–122]. MWNTs filled with iron atoms demonstrated that they could be used as medecine vectors by gathering at a specific location using a magnet [123], and also that they could be used for experimental cancer treatment using the magnetic

hyperthermia thechnique [124]. Finally, the encapsulation is also commonly studied for tuning the properties of both encapsulated molecules and host carbon nanotubes. For example, L. Alvarez *et al.* have widely studied the reciprocal influence of different compounds, such as polyiodides [125, 126] or π-conjugated molecules [127–131], encapsulated inside CNTs.

1.4.2 Toxicity of carbon nanotubes

One of the major preoccupation related to the use of the CNTs concerns their potential toxicity toward living beings. As any other nanomaterial the potential risks on the health and environment due to their large scale production are not yet fully determined, even if several research groups are trying to answer this very complex question.

First of all, the functionnalized CNTs can be internalized by living cells without showing any evidence of toxicity for them [132]. Two different routes of penetration have been found, and depend on the functionalization of the CNTs and their size : the endocytosis [132, 133] (see figure 1.13) and the passive diffusion, *i.e.* the CNTs pass through the cell's membrane by perforating it such as needles [134]. Jin et al. [135] have even shown that the CNTs entered *via* endocytosis could be expelled by means of exocytosis.

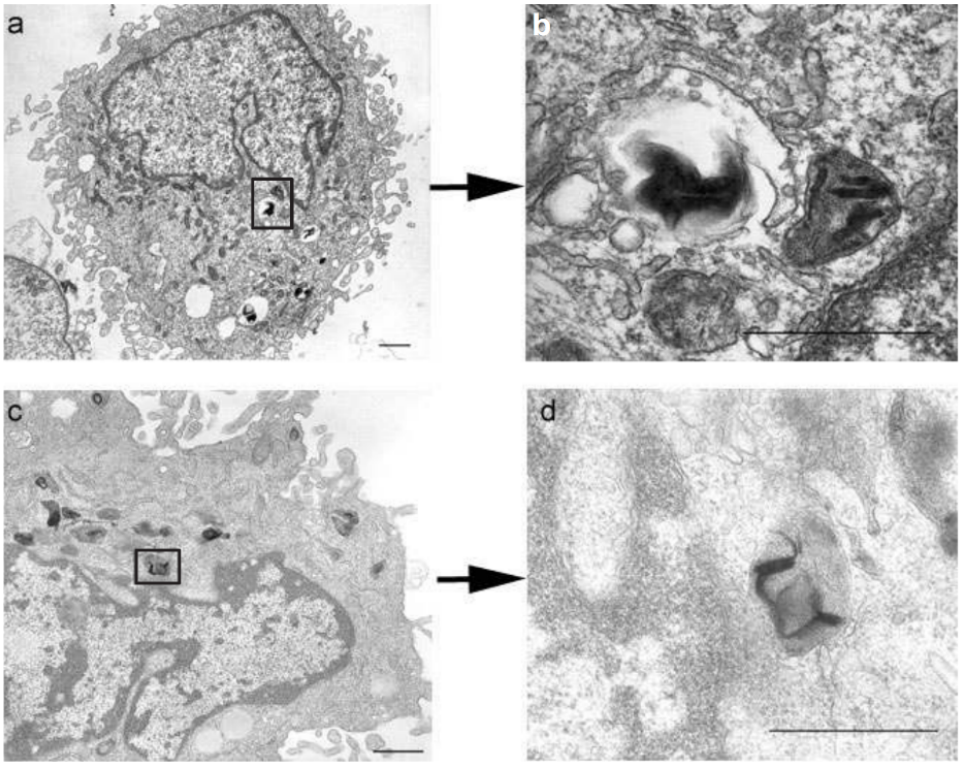

FIGURE 1.13: *TEM images of CNTs internalized in murine myoblast stem cells[133]. (a) and (b) show inclusion bodies containing aggregated SWNTs. (c) and (d) show a vesicle containing an aggregate of carbon nanotubes*

However, the remaining catalytic compounds (metal nanoparticles) used for the synthesis of the CNTs are suspected to be toxic for the organisms, by forming free-radicals that could damage the proteins, lipids and the genetic materials contained by the cells. For example, the residual cobalt can damage the chromosomes [136] and Fe ions can be responsible for oxidative stress. Then, the CNTs have a tendency to agglomerate in aqueous media (and therefore in biological media), phenomenon that could render particularly hard for the organisms to eliminate them. Furthermore, the chemical modification of the walls of the CNTs (i.e. their functionalization) can influence drastically their potential toxicity [136], being directly in contact with their near-environment. As well as the state of their walls influences directly the integration of the CNTs in biological media, and their interactions with the cells and the tissues. For example, the higher rate of functionnalization

of the CNTs, the better their dispersion, the easier seemed to be their elimination through the kidneys [137]. On the contrary, CNTs with a low rate of functionalization appeared to accumulate in the organs (liver, spleen, lungs, etc.). We find also evidences that the CNTs diameter and length [138] can influence their toxicity. Indeed, the longer the tubes, the more intense are the inflammatory responses because their elimination from the body becomes difficult or impossible. Concerning the influence of their diameter, studies suggest that the SWNT exhibits a higher toxicity than the DWNTs [139] and the MWNTs [140]. Finally, both the purification and the functionalization of the CNTs seem to play a crucial role on the damages they can cause to organisms and the way they are eliminated.

The question of the characterization of CNTs within cells or organisms is central, especially to assess their presence in particular cell compartments. As illustrated above, images are often shown at relatively low magnification and can only reveal the presence of agglomerates. The challenge comes from the fact that the contrast of single CNTs (and in particular single- or double-walled CNTs) is extremely low (carbon in a carbon environment). The question of the in vivo detection of CNTs is developed in the next paragraph.

In vitro and in vivo detection of the CNTs

In order to visualize the internalization of the CNTs by the cells, the more used technique is by far the functionalization with fluorescent molecules. FITC is a good example as it is very cheap, and therefore widely used, for the covalent or non-covalent functionalization of CNTs by fluorophores. The fluorescence emitted by the molecule is therefore directly visible by means of confocal microscopy (Figure 1.14) [106, 132, 141]. Nevertheless, using this technique requires to consider some important points : the covalent bonds between the CNTs and the fluorescent molecules must be able to resist to enzymatic cleavages. The non-covalent bonds have to be strong enough to

prevent the fluorescent molecule to be released during the experiment. Finally, the functionalization is very likely to modify the CNTs behavior in the studied biological environment, as discussed earlier.

For all these reasons, which illustrate the drawbacks of the fluorescence techniques, other techniques have been developed for the *in vitro* and *in vivo* detection of the CNTs, such as the Infra-Red fluorescence microscopy [142–144] (intrinsic fluorescence of the SWNTs only), the Raman spectroscopy [145, 146](for any type of CNTs but for given chiralities only [147]), or the two-photon excitation microscopy [148] but requires the use of very expensive ultra-fast lasers and can also cause thermal damage to certain cells or tissues [149].

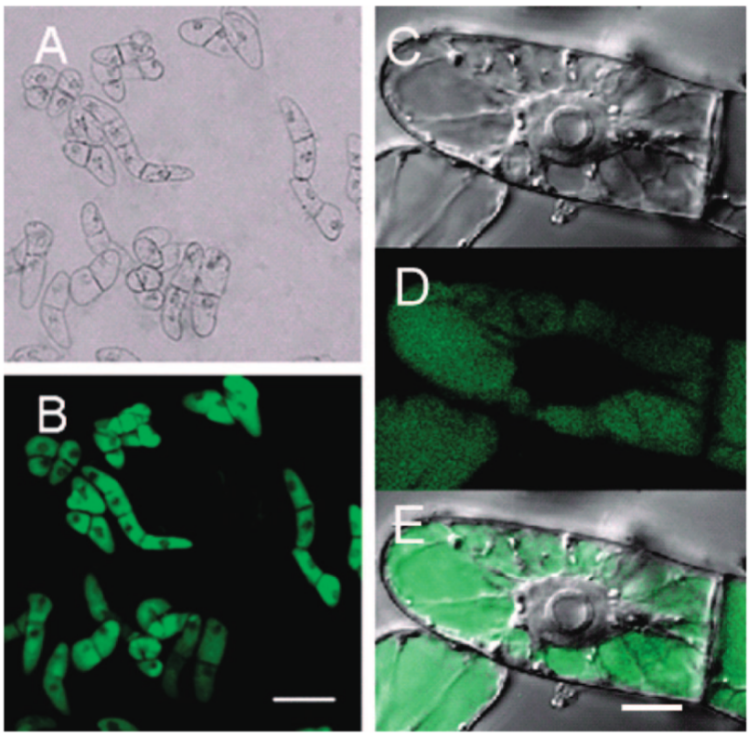

FIGURE 1.14: *Confocal microscopy images of cells incubated with SWNT/FITC: (A) bright field image; (B) fluorescence image; (C) Differential interference contrast image under high magnification; (D) fluorescence image under high magnification; (E) overlay of C and D. Scale bars are 100 μm for (A) and (B) and 10 μm for (C-E) [106].*

Therefore, as the fluorescence techniques are widely used, cheap, easy to

operate and allows to track any type of CNTs, and as the alternative techniques present significant drawbacks (type of CNTs-dependent, expensive or damaging for the samples), it is very relevant to deeper investigate the assumptions inherent in the use of fluorophores for CNTs toxicity studies.

1.5 General motivation of the thesis

Like many other nanomaterials, carbon nanotubes (CNTs) have found applications in many fields because of their outstanding chemical and physical properties, and are nowadays widely studied from materials science to nanoelectronics [77], and even in nanomedecine, where they have been used to elaborate drug delivery systems for cancer therapy, biosensors or contrast agents for magnetic resonance imaging [150–152]. The direct consequence of these modern applications is a growing interest in such nanomaterials and the increase in their large scale production [153], leading to an increasing risk of environmental and human exposure. It becomes therefore more and more relevant to evaluate their potential impact on the health and the environment, and the toxicity studies on this topic are multiplying over the past decade [154–160]. For those toxicity studies it is often required to know the exact location of the CNTs accumulating, or simply circulating, inside organisms or cells. A very common way to track them in such conditions is to functionalize the CNTs with fluorescent molecules which would be illuminated afterwards under a light with the appropriate excitation wavelength. Despite the fact that these fluorescence strategies are very cheap and easy to operate, they suffer from a major drawback: they assume that the fluorescent molecule would be permanently linked to the CNTs. It is however reasonable to question this assumption as the fluorescent molecules are usually constituted by one or more 6-carbon rings which can interact with the delocalized electron cloud of the CNTs. These non-covalent bonds could

later lead to the desorption of the fluorophore once the CNTs reach the complex chemical environment of a living cell and even before entering the cell (formation of a corona of proteins or phospholipids competing with the adsorbed dye, pH decrease within lysosomes, etc.). Therefore, the fluorescence data could lead to wrong information about the CNT's location. The consequence is that a number of published results may be questioned in terms of the actual distribution of the CNTs within cells or at the whole organism level (biodistribution), and the kinetics of this distribution. This may have very important consequences regarding the conclusions about their fate (accumulation, excretion) and thus their toxicity in general. It is thus fundamental to understand the grafting mechanisms and estimate the efficiency of the covalent functionalization of the CNTs as well as the amount of simply adsorbed fluorophores. In order to answer to these questions, we proposed a new approach based on both qualitative and quantitative evaluation of the way the fluorophores are bonded to the DWNTs, by means of two different spectroscopic techniques. First, we performed X-ray photoelectron spectroscopy (XPS) which allowed to probe the surface of the samples and to understand the different types of interactions between the fluorophores and the DWNTs. Then we characterized the bulk of our samples with the help of inelastic neutron scattering (INS) techniques. Indeed, neutron techniques are especially sensitive to the Hydrogen atoms while they have a low sensitivity to the carbon ones. This property makes them a perfect probe of our samples, allowing to highlight the organic molecules since the information on the contribution of CNTs is much reduced. In addition to neutron techniques we used computational techniques such as density functional theory (DFT) calculations (lattice dynamics) in order to gain a better understanding of our samples, provide hypothesis to strengthen data analysis and to be able to derive quantitative information from our experimental results.

This work presents our investigations on the functionalization of double-walled carbon nanotubes (DWNTs) with fluorophores.

First, we chose to study the functionalization of double-walled carbon nanotubes (DWNTs) with a very common fluorophore, fluorescein isothiocyanate (FITC), widely used in toxicity studies for its very low cost and easy visualization by fluorescence microscopy. We also used a well-known three step functionalization process to graft the FITC on oxidized DWNTs [161, 162].

In addition, we investigated the influence of the fluorophore's geometry by studying a second fluorescent molecule, the cyanine $5\mathrm{Me}(\mathrm{NEt}_2)_2)$, which is not commercialized but presents a very different geometry compared to the FITC, allowing to compare how this parameter influences the functionalization when performed in the same conditions.

We also used models of these fluorophores and simulated their behavior in the surrounding of CNTs, providing more insights to the way they can be adsorbed on such nanoparticles.

Finally, it is important to add that the question of the nature of the grafting of a molecule onto CNTs is also interesting for the field of materials science in general and not only relevant for toxicity studies (stability of sensors including functionalized CNTs, functionalized CNTs dispersed within a nanocomposites, etc.).

Chapter 2

Equipments and methods

2.1 Sample preparation

2.1.1 Synthesis of the double-walled carbon nanotubes by CCVD

Synthesis from a catalytic powder

The double-walled carbon nanotubes (DWNTs) are synthetized by catalytic chemical vapor deposition (CCVD) from an oxide catalytic powder ($Mg_{0.99}Co_{0.0075}Mo_{0.0025}O$). After the synthesis a composite powder is obtained. Its composition is well known and, typically contains around 12 $\%_m$ of CNTs (80 % DWNTs) and desorganized carbon. Concerning the DWNTs so-produced, their inner and outer diameters range from 0.5 to 2.5 nm and from 1.2 to 3.2 nm, respectively. The median inner diameter is 1.3 nm and the median outer diameter is 2.0 nm. The composite powder also contains 88 $\%_m$ of unmodified magnesia, plus some carbon-coated metalic nanoparticules. It is thus necessary to further purify by applying several chemical treatments (extraction, purification, etc...) in order to obtain samples with high contents of DWNTs and low rates of impurities. These different steps are described hereafter.

Extraction of the DWNTs from the composite powder

The extraction treatment aims at dissolving the magnesia and the accessible Cobalt an Molybdenum nanoparticules. To do so, 1 g of nanocomposite powder is placed in an erlenmeyer flask, and is wet with 3-4 g of deionized water, then completely immersed in 15 mL of Chloridric acid (HCl) 37%. The opening of the flask is closed with para-film and the mixture is sonicated for 10 min in an ultrasonic bath. The solution has a blue-green coloration at that point, related to the dissolution of the Co and Mo. After one night, the mixture is filtered using a cellulose nitrate membrane (0.45 μm pore size), and the first filtrate exhibits the blue-green characteristic coloration. The CNTs are then washed with deionized water until the filtrate becomes neutral. At this point, the extracted CNTs can be either kept wet for immediate chemical treatments or can be dried using freeze-drying for later use. Concerning the freeze-drying, the CNTs are placed in a glass bottle which is filled with deionized water. They are then sonicated for 10 minutes in order to be well dispersed and are placed in a freezer, waiting for the freeze-drying procedure. The extraction efficiency is estimated around 12% of the nanocomposite starting material (in weight).

2.1.2 Purification of the DWNTs

The raw DWNTs sample obtained with the extraction treatment still contains remaining Co (3.5 %) and Mo (1.0 %), mainly in the form of nanoparticles tightly encapsulated inside carbon shells. When the DWNTs undergo oxidative treatments the carbon shells are as well chemically attacked allowing the acids to enter the shells and to dissolve the entrapped metallic nanoparticules.

Double oxidation

The double oxidation treatment is a two-step oxidative process (see Figure 2.1) that has been widely studied at the CIRIMAT [163]. We mainly use this process today for DWNTs purification because it presents many advantages. Indeed, not only it enables the elimination of the metallic impurities as it has been mentioned above, but also it leads to the degradation the amorphous carbon produced during the CCVD synthesis. It also allows the opening of the extremities of the CNTs. Finally, the double oxidation treatment has the property of creating functional oxygenated groups, mainly in the form of carboxyle (-COOH), at the tips but also on the sidewall of the CNTs due to the presence of surface defects. Strictly speaking, the creation of those groups at the surface is already considered as a first step of functionalization, and will be used as anchor points for the further steps of the grafting process.

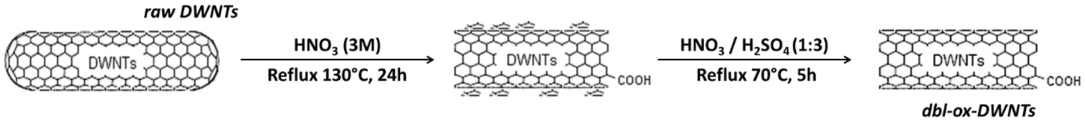

FIGURE 2.1: *Illustration of the two steps of the double oxidation treatment.*

Step 1: Oxydation with Nitric acid. To begin, 100 mg of raw DWNTs are put in a 250 mL round-bottom flask. Then, 100 mL of a Nitric acid (HNO_3) solution with a concentration of 3M is added. The suspension is sonicated in an ultrasonic bath for 10 minutes in order to break the agglomerates and disperse the raw DWNTs. The suspension is then stirred and heated under reflux conditions at 130 °C for 24 hours, and then cooled down to the room temperature, the stirring is switched off in order to allow the decantation of the DWNTs. The suspension is filtered with a polypropylene membrane, the filtrate has a pale yellow coloration. Finally, the DWNTs on the membrane

are washed with deionized water until the filtrate becomes colorless and neutral. The yield of the oxidation step with Nitric acid is around 82 % so, 100mg of raw dry DWNTs usually lead to *ca.* 82g of oxidized material.

Step 2: Oxidation with a Nitric and Sulfuric acid mixture. Right after the first step of the double oxidation treatment, 100 mg of wet DWNTs are placed in a 250 mL round-bottom flask, and 100 mL of a mixture solution of Nitric acid and Sulfuric acid HNO_3 65% / H_2SO_4 95% (1:3) are added. The suspension is sonicated for 10 minutes in an ultrasonic bath for dispersion purposes. It is then heated at 70 °C under reflux conditions for 5 hours. When the reaction is over, the suspension is cooled down to room temperature. The content of the round-bottom flask is diluted very slowly in deionized water (exothermic chemical reaction and NOx vapor release), and then it is put aside for a night of decantation. Finally, the suspension is filtered on a polypropylene membrane (0.45 μm pore size). Please note that the filtrate shows a brown-orange coloration and the filtration is really slow. The so obtained oxidized DWNTs, are then washed with deionized water until the filtrate becomes colorless and neutral. At this point the DWNTs can once again be kept wet for an immediate chemical treatment or freeze-dried. The efficiency of the oxidation with this Nitric acid and Sulfuric acid mixture is around 18 % (for a 5-hour treatment).

Washing with NaOH

After the oxidation treatments, an additional procedure is necessary in order to obtain high purity DWNTs. Indeed, during the oxidation treatments, carboxylated carbon fragments (CCFs) are produced and coat the walls of the DWNTs. The CCFs must be removed before any further steps because they are highly chemically reactive. To do so, 100 mg of double-oxidized DWNTs are introduced in a round-bottom flask containing 200 mL of a NaOH (4M)

solution. The mixture is sonicated for one hour at room temperature in an ultrasonic bath and finally put aside at room temperature overnight. After the night, the suspension is filtered on a polypropylene membrane. The filtrate typically has a brown-pink coloration. The DWNTs obtained are then washed with deionized water until the filtrate becomes colorless and neutral. As for the previous steps, the so obtained DWNTs can either be kept wet for further treatment or can be freeze-dried before storage. At this step the sample will be refered as "**DWNT-dbl-ox**".

2.1.3 Steps toward the covalent grafting of the Fluorophore

Few changes have been made to the protocol established by Bortolamiol in a previous Ph.D. Thesis [161], in order to improve the efficiency of the grafting process. First of all, FITC, because of its high reactivity, can be degraded in water solution by reacting slowly with the solvent. However the last step of the functionalization process was originally performed using a water-based buffer solution of sodium hydrogen carbonate (0.1M ; pH=8.4). In order to avoid any risk of degradation of the FITC in this aqueous solution, the water has been replaced by anhydrous Tetrahydrofurane (THF) buffered with a "Hünig's base" : N,N-diisopropylethylamine (DIEA). Finally, the freeze-drying of the DWNTs between the different functionalization steps leads to a significant agglomeration of the nanotubes, thus decreasing their dispersion and consequently hindering the surface chemical reactivity with FITC. In order to avoid this issue, the different following steps of the process were performed directly, without any intermediate drying step of the sample.

Carboxyl groups activation

An amidation chemical reaction involve two functional groups : a carboxyl group and an amine group (see Fig. 2.2). The carboxyl group is provided

by the oxidized carbon nanotubes (DWNT-dbl-ox) while the amine group is provided by the selected linker, 1,4-diaminobutane in our case.

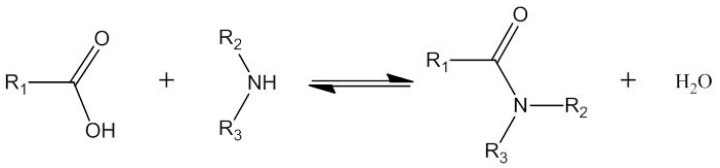

FIGURE 2.2: *Amidation chemical equilibrium.*

The amidation equilibrium presented above is naturally shifted toward the formation of the carboxyl and amine groups. Nevertheless the carboxyl groups can be "activated" and be turned into an acyl chloride group (-COCl), a more reactive compound. This has been done using the oxalyle chloride through the mechanism detailed on figure 2.3.

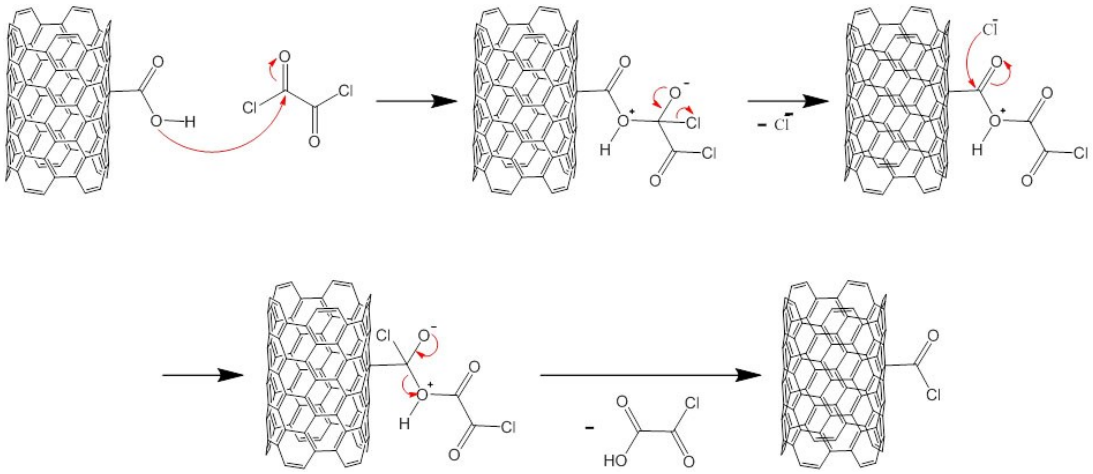

FIGURE 2.3: *Carboxyl groups activation mechanism via the use of oxalyle chloride.*

The DWNTs are directly suspended in pure (no solvent) oxalyl chloride (20 minutes in an ultrasonic bath), then the suspension is heated at 55 °C under reflux for 24 hours in an argon atmosphere. By performing the chemical reaction directly in undiluted oxalyl chloride, the chances to activate all the carboxyl groups are increased. Moreover, the oxalyl chloride is very sensitive to water (expectable traces in dry DWNT), and working in large excess of reactant prevents any degradation of the activation process. After the reaction the DWNT are not dried, the oxalyl chloride is slowly eliminated by

distillation and replaced by anhydrous THF (about 100 mL) in anticipation of the following functionalization steps.

Grafting of a diamine : 1,4-diaminobutane

The grafting of the linker (1,4-diaminobutane in our case) onto the activated DWNT is performed through a nucleophilic substitution grafting mechanism leading to the creation of an amide bond between the activated nanotubes and the linker, as described in Figure 2.4 below.

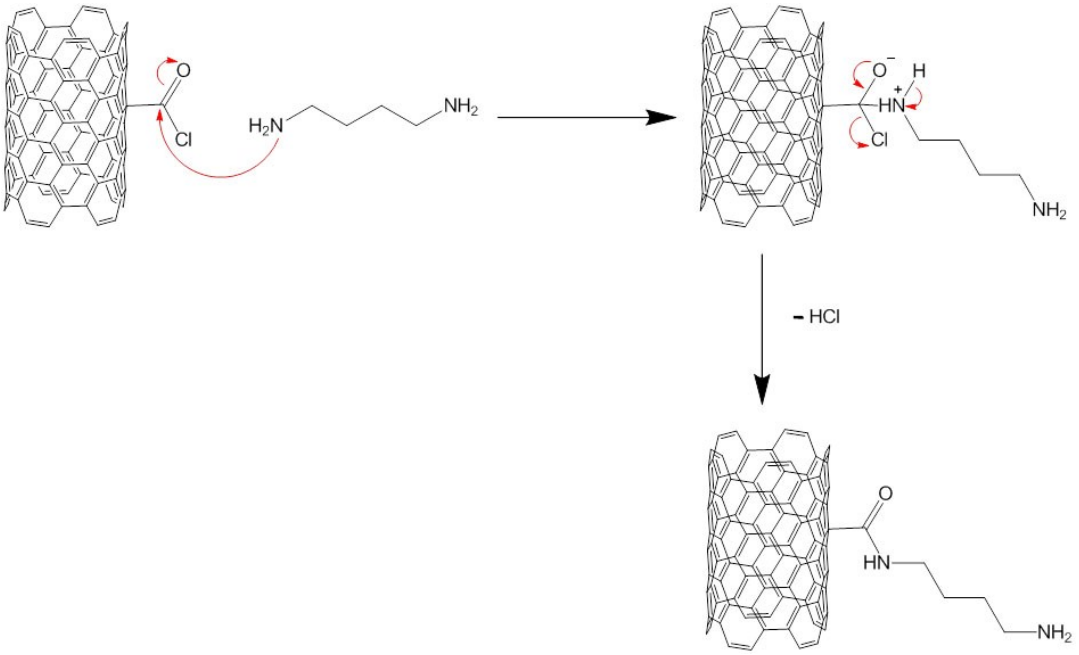

FIGURE 2.4: *Grafting mechanism of the 1,4-diaminobutane via amide bond creation.*

100 mg of activated DWNT in 100 mL THF suspension are first sonicated in an ultrasonic bath for 10 minutes. Then, 22.7 mmol of 1,4-diaminobutane and 22.7 mmol of N,N-diisopropylethylamine (DIEA) are added to the suspension. Indeed, the DIEA is a rather strong base (pKa= 10.1) and non-nucleophilic, commonly used in organic chemistry. Its role is to increase the pH of the suspension, and therefore favor the $-NH_2$ form of the primary amine fonctional group (and not the $-NH_3^+$ form which does not participate to the nucleophilic substitution reaction), and to trap the hydrochloric acid

formed during the reaction (see Fig. 2.5).

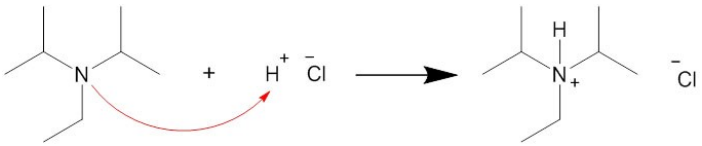

FIGURE 2.5: *Proton trapping mechanism of the the DIEA.*

The mixture is bath sonicated for 10 minutes and then stirred 96 hours at 30 °C. It is crucial to work in excess of amine in order, on the one hand, to be able to functionalize all acyl groups at the DWNT surface and, on the other hand, to avoid the risk of bridge formation through the fixation of one diamine on two close carboxyl groups, either on the same or in between two different DWNTs. Moreover, the use of an organic solvent such as the THF allows a better homogenization and stirring of the suspension. THF has been chosen instead of N,N-dimethylformamyde (DMF) (commonly use for this type of reaction) in order to avoid the introduction of residual Nitrogen in the samples, that could interfere with our attempt to quantify the efficiency of the grafting process. After the 96 hours, the mixture is filtered on a polypropylene membrane (0.45 μm pore size) in order to remove the remaining reactants. The DWNTs are finally washed 10 times with anhydrous THF.

After this step, the DWNTs can be freeze-dried in order to constitute the sample referenced as "**DWNT-diamine**", or they can be dispersed in 80 mL of THF in anticipation of the last step of the grafting process. **Please note that the diamine that react with the DWNTs become an "1-amide,4-aminobutane" in a strict sens but will nevertheless be referred as a "diamine" in the rest of the manuscript for a better understanding.**

Grafting of the Fluorophore : Fluorescein Isothiocyanate

Once the diamine has been grafted on the DWNTs, it is possible to graft different fluorophores which allow potential tracking for in vivo experiments. In biology several fluorescent molecules are commonly used, and notably the fluorescein (see Fig. 2.6).

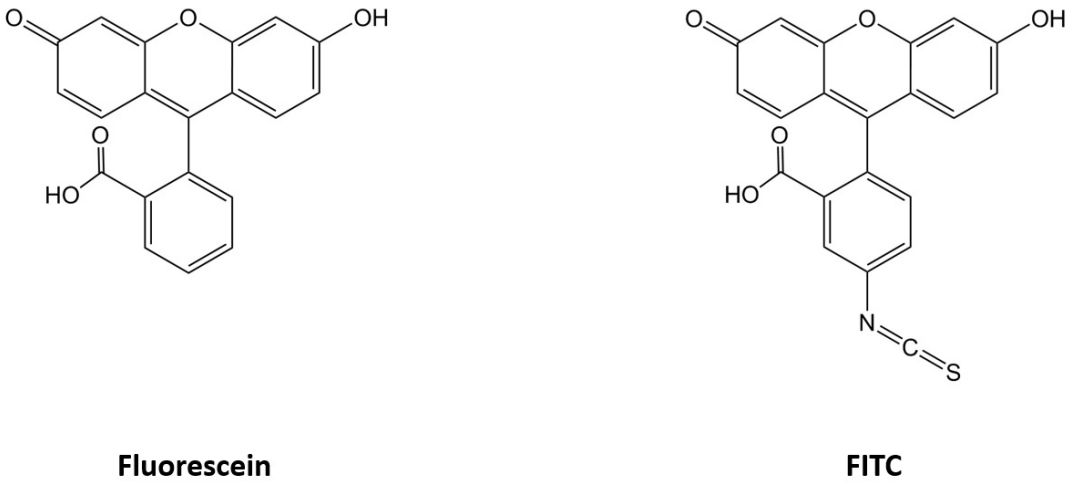

FIGURE 2.6: *Molecular structures of the Fluorescein and the Fluorescein Isothiocyanate (FITC).*

In order to be grafted onto the DWNT-diamine, the fluorescein has to be used under its derivative avtivated form : the Fluorecein Isothiocyanate, or FITC (see Fig. 2.6). Indeed, the isothiocyanate functional group presents a high reactivity with the primary amine functionnal groups, and end up forming a thiourea group (see figure 2.7). Its common use in biology comes from the fact that it is very cheap and easily found on the market.

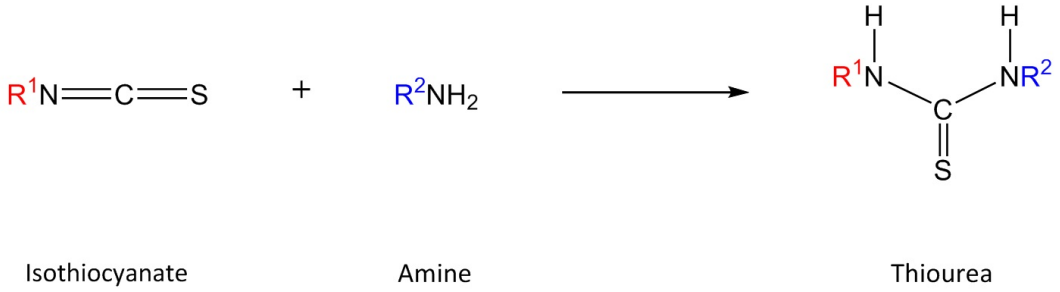

FIGURE 2.7: *Grafting mechanism of the FITC on the DWNT-diamine via thiourea group formation.*

Concerning the grafting of the FITC, 100 mg of DWNT-diamine are dispersed in 100 mL of anhydrous THF with the help of sonication, Sonotrode (15min, 5s On/3s Off/30% amplitude) and Bath (15 min). Then, $1.5.10^{-4}$ moles of DIEA is added to the suspension, and it is sonicated for 10 minutes. The FITC ($1.5.10^{-4}$ moles) dissolved in 10 mL of anhydrous THF is added such as the quantity of fluorophores represent twice the quantity of estimated diamine onto the DWNTs. The suspension is first sonicated with the help of a sonotrode (15min, 5s On, 3s Off, 20% of amplitude) and then with an ultrasonic bath for 45 minutes. The container is finally sealed with parafilm and kept away from light for 72h under stirring at room temperature. Then, the suspension is filtered, the functionalized DWNTs are washed with THF, then water, and freeze-dried. This constitutes the sample named "**DWNT-diamine-FITC**" (see figure 2.8). **Please note again that the amine group that react with the FITC become an amide group in a strict sens but we will nevertheless refer to the linker as a "diamine" in the rest of the manuscript for a better understanding.**

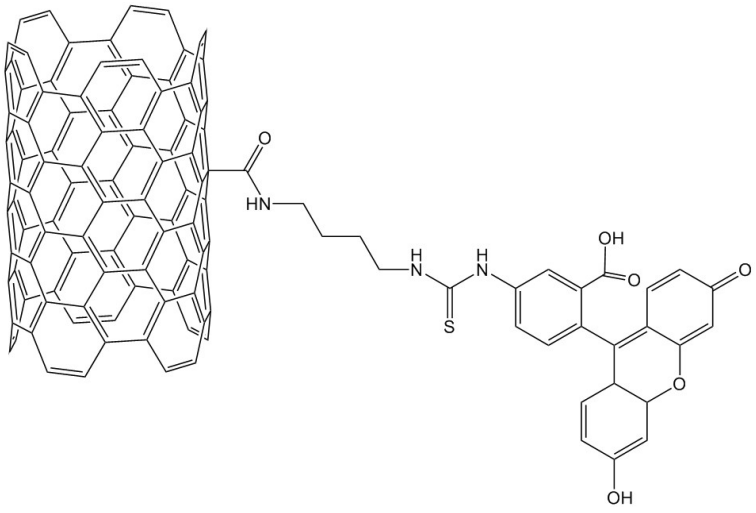

FIGURE 2.8: *Representation of the sample DWNT-diamine-FITC, after the grafting process of the FITC onto the DWNT-diamine.*

Grafting of the Fluorophore : the streptocyanine

The cyanines are widely used for medical imaging, notably for nucleic acids and protein marking [164, 165]. In the framework of this thesis project, we chose to study more specifically the Streptocyanine $5\mathrm{Me}(\mathrm{NEt}_2)_2$ (open-chain Cyanine), because it presents some advantages compared to the other Cyanines. Indeed, under its initial form of Hemicarboxonium, the molecule is not fluorescent. Once this Hemicarboxonium reacts with an amine function, creating a covalent bond, we obtain the final streptocyanine $5\mathrm{Me}(\mathrm{NEt}_2)(\mathrm{NHR}')$. The latter owns a form very close to the $5\mathrm{Me}(\mathrm{NEt}_2)_2$ and is fluorescent (see Figure 2.9). It means that if the fluorescence is observed, we can be sure that a certain ratio of the molecule is covalently bonded. Another advantage is that this streptocyanine exhibits two parallel aromatic 6-carbon rings that are perpendicular to the main carbon chain in witch both nitrogen atoms are not included in conjugated heterocycles, and therefore makes it a worse candidate for its adsorption (particularly *via* π-π interactions) onto the DWNTs when compared to FITC that has a planar geometry. Nevertheless, it presents the disadvantage not being available commercially and needs to be synthesized on demand [166]. The synthesis of the Hemicarboxonium and the streptocyanine $5\mathrm{Me}(\mathrm{NEt}_2)_2$ were performed by Corinne Payrastre from the team *Acides Nucléiques Modifiés* of the laboratory of *Synthèse et Physico-Chimie de Molécules d'Intérêt Biologique* (SPCMIB) in Toulouse.

Concerning the grafting protocol itself, we used the same protocol as for the grafting of the FITC, except the THF was replaced by the dimethylsulfoxide (DMSO) which is a better solvent for the streptocyanine. We started from 100 mg of the DWNT-diamine sample and used twice the quantity of estimated diamine onto the DWNTs for the number of moles of Hemicarboxonium and DIEA. We then obtained a sample constituted of DWNTs-diamine

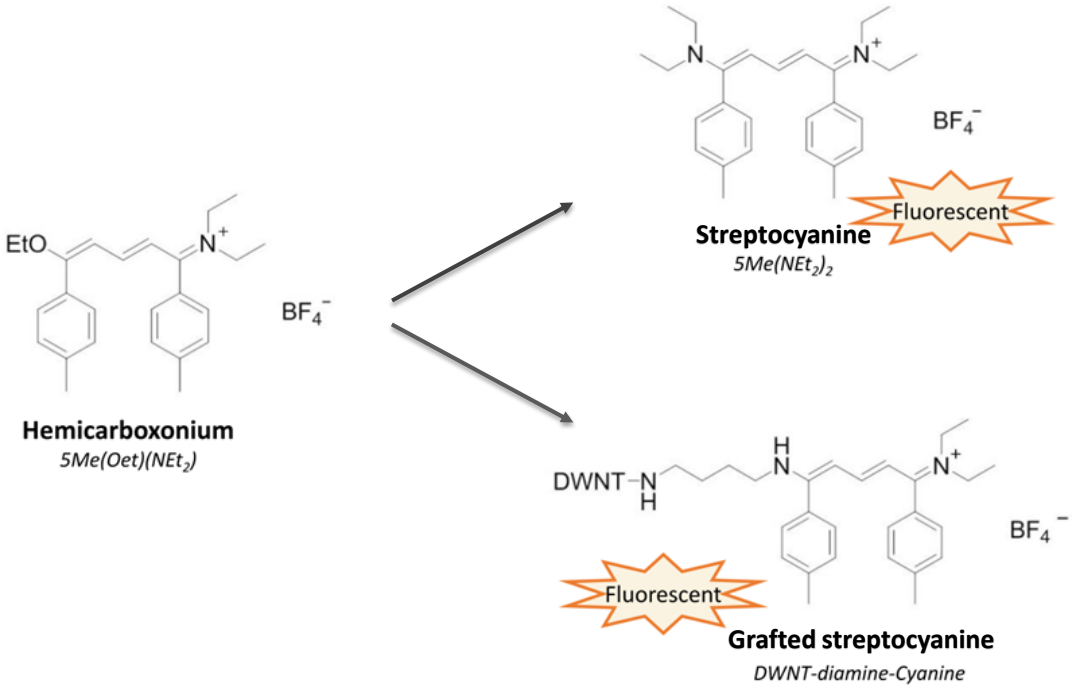

FIGURE 2.9: *Molecular structures of the Hemicarboxonium the Cyanine and the covalently grafted Cyanine.*

with covalently grafted streptocyanine that will be referred as "**DWNT-diamine-Cyanine**".

Please note that, for clarity reasons, the streptocyanine $5\mathrm{Me}(\mathrm{NEt}_2)_2$ **and its grafted form, the streptocyanine** $5\mathrm{Me}(\mathrm{NEt}_2)(\mathrm{NHR}')$**, will be respectively called "cyanine" and "grafted cyanine" for the rest of the manuscript.**

2.1.4 Reference samples

In order to be able to understand the grafting efficiency of our covalent grafting process, several reference sample were chosen and were used for the analysis of the experimental results.

Individual molecules

We used three different reference individual molecules. First, we used 1.35 g of commercial 1,4-diaminobutane (reference for the linker). The 1,4-diaminobutane is liquid at ambient temperature and the rather large quantity used for the experiments comes from the need of filling the aluminium cylindrical tube in order to have the maximum of neutrons reaching the sample. Then, we used 100 mg of commercial FITC for the reference of our first fluorophore. And finally, we used 100 mg of the cyanine $5\mathrm{Me}(\mathrm{NEt}_2)_2$ as a reference for the grafted cyanine. We were limited by the synthesis of the $5\mathrm{Me}(\mathrm{NEt}_2)_2$ and the Hemicarboxonium by the SPCMIB, which are both expensive and time consuming to prepare. We had thus to be very careful with the quantities that were given to us and to save all the Hemicarboxonium for the preparations of the sample that, later, required a grafting process.

Those three samples will be referred respectively as "**Diamine**", "**FITC**" and "**Cyanine**".

Linker-fluorophores covalent bonding

In order to have references for the covalent grafting of the fluorophores onto the DWNTs , we synthesized two samples where we performed the grafting process without the presence of the nanotubes, *i.e.* we performed the grafting chemical reaction in between the 1,4-diaminobutane and our two fluorophores. For this purpose we remained in the same conditions as established previously for the grafting process onto the DWNTs. But, as the 1,4-diaminobutane owns two $-\mathrm{NH}_2$ functional groups in its individual form we choose to remain in stochiometric conditions in order to avoid having fluorophore molecules that did not react in our reference samples. We took then two moles of fluorophores for one mole of 1,4-diaminobutane. We finally obtained 100 mg of the product of reaction between the 1,4-diaminobutane

and the FITC, this sample will be named "**Diamine-FITC**". And, because of the limitations in terms of quantity of Hemicarboxonium (mainly used for the grafting process onto the DWNTs), we were only able to produce 13.5 mg of the product of reaction between the 1,4-diaminobutane and the Hemicarboxonium. Despite this low quantity, the sample contains a lot of hydrogen atoms and can still provide us information by neutron spectroscopy analysis. This sample will be referred as "**Diamine-Cyanine**".

DWNT-fluorophores non-covalent grafting

To evaluate the non-covalent grafting of the fluorophores onto the DWNTs, we also prepared two samples that are references for the non-covalent grafting. To do so, 100 mg of DWNT-dbl-ox are placed in THF or DMSO, and are sonicated for 10 minutes. Then, the fluorophore grafting processes were reproduced in the same way, in order to be as close as possible to the reality of the grafting process. In the absence of linker onto the DWNT, the fluorophore is then not able to react and all the fluorophores remaining in the sample after the washing procedure can be attributed to the non-covalent grafting (adsorption). We thus obtain two different samples. The first one contains 100 mg of DWNTs with FITC adsorbed at their surface and will be named as "**DWNT@FITC**". The second one contains 100 mg of DWNTs with Cyanine $5\mathrm{Me(NEt_2)_2}$ adsorbed at their surface and will be referred as "**DWNT@Cyanine"**. Once again we were limited by the quantities of Hemicarboxonium we were able to obtain. Even if it is the Hemicarboxonium that is supposed to be adsorbed at the surface after the grafting process, we choose to use the extra quantity of the cyanine $5\mathrm{Me(NEt_2)_2}$ and save the Hemicarboxonium for the covalent grafting processes.

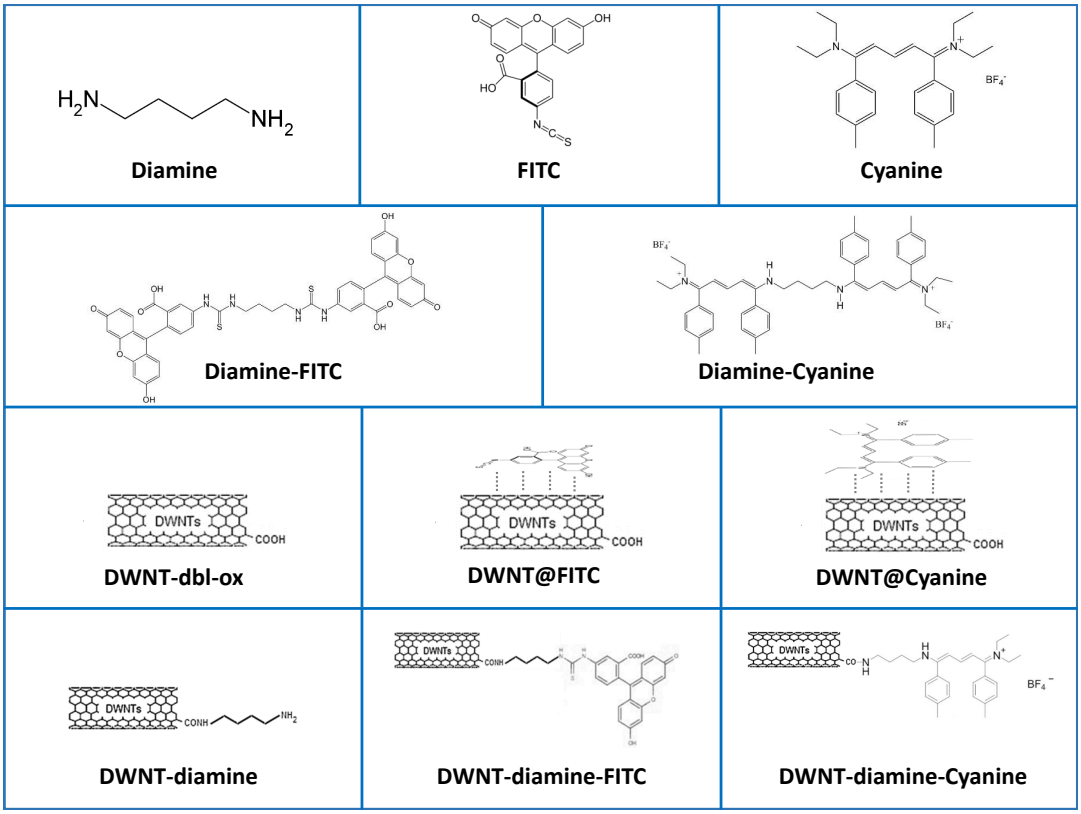

FIGURE 2.10: *Representation of the 11 samples selected for studying the grafting of fluorophores onto double-walled carbon nanotubes.*

2.1.5 Sample Summary

Please note that the samples' names may differ from the names used in our publications. Indeed, some changes were made for the clarity of the articles related to this work. Nevertheless, for the coherence of this manuscript the names of the samples remained unchanged.

2.2 Inelastic Neutron Scattering spectroscopy

Various neutron techniques are available nowadays. In this section we will voluntarily skip the neutron techniques that were not used during this thesis, such as neutron diffraction or elastic neutron scattering, and focus on the inelastic neutron scattering (INS) spectroscopy which was relevant for the project.

2.2.1 Neutrons: properties and interest

Neutrons are particles, they own a mass of 1,675.10^{-27}kg, no electric charge and an 1/2 spin. The energy of a neutron E is linked to its velocity v with the relation $E = \frac{1}{2}mv^2$, and can be expressed as a function of its temperature T with the relation $E = \frac{3}{2}k_BT$, with k_B is the Boltzmann constant. To this particle is associated a plane wave (wave-particle duality) described by a wave vector $\overrightarrow{k}$, collinear to the direction of propagation, and a wavelength λ. The modulus of the wave vector is related to the wavelength by the relation $|\overrightarrow{k}| = \frac{2\pi}{\lambda}$. Their energy E is also expressed as:

$$E = \frac{\hbar^2 k^2}{2m} = \frac{h^2}{2m\lambda^2} \tag{2.1}$$

Where h is the Plank constant and $\hbar$ is the reduced Plank constant. Working with the wavevectors instead of the wavelengths often makes the equations easier to handle, but the price to pay for this is that we need to think in terms of reciprocal space rather than real space.

The neutrons present actually a large variety of properties that make their use as a characterization tool particularly interesting. First of all, their energy can be monitored by the control of their temperature. Indeed, by using different moderation materials temperature it is possible to tune the neutrons energies, and have access to a wide range of energy that matches the typical energies of the elementary excitations found in solids and liquids (phonon, molecular vibrations...). These peculiar properties make neutron scattering a very natural and powerful **probe for studying both the structure and the fluctuations of the atomic positions in condensed matter**. Secondly, the pecular properties of INS techniques, particularly interesting, are their **high sensitivity to hydrogen atoms vibrations**. Indeed, contrarily to the

photon-based spectroscopic techniques (Infra-Red, Raman, X-ray ...), generally most sensitive to vibrations involving heavier atoms with larger number of electrons, the INS techniques present a cross section of hydrogen uniquely high, making it about ten times more visible than any other atoms. Figure 2.11 compares the relative size of the X-ray and thermal neutron scattering cross section σ for various elements, and give an illustration of this INS spectroscopy peculiar feature. Thirdly, the neutrons interact with the nuclei of the atoms, which allows isotopic labeling, and are very penetrating. Indeed, they are able to penetrate deeply into typical samples and pass readily through the walls of containment vessels (generally aluminium or steel), and are thus naturally weighted to the measurement of bulk properties. Fourthly, the INS spectroscopy techniques are not subject to the rules of optical selection. Indeed, all vibrations are active in INS spectroscopy and, in principle, measurable. When scattered, the neutron transfers momentum to the atom and the INS measurements are not limited at the Brillouin zone centre, as are photon techniques. Also, the measured INS intensities are proportional to both the concentration and the atomic displacement of the atoms in the sample. Finally, INS spectra are **easily and accurately modelled by computers**. Indeed, the complications arising from the electro-optic parameters are avoided and the band positions and intensities of most molecular models can be calculated using well-established computational methods.

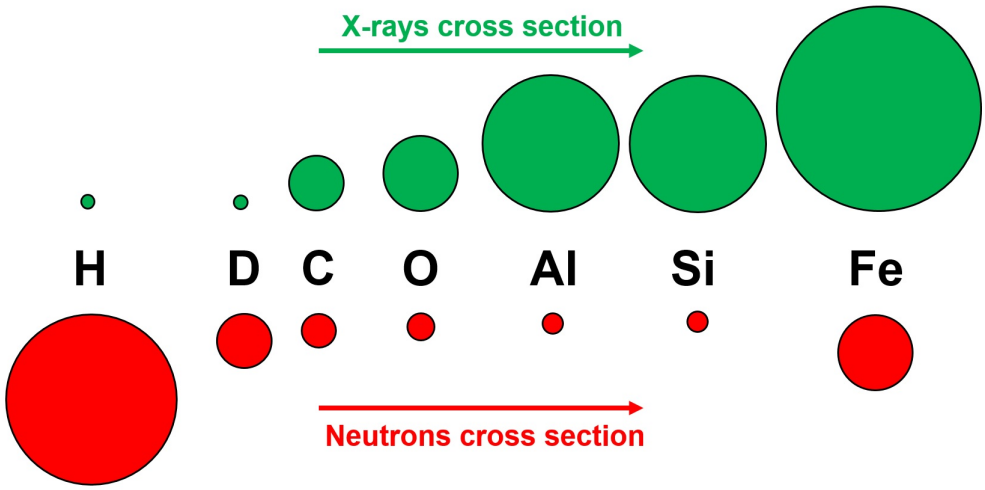

FIGURE 2.11: *Comparison of the relative size of the X-ray and thermal neutron scattering cross section σ for various elements.*

2.2.2 Basics of inelastic neutron scattering

The aim of this section is, for obvious reasons, not to develop the whole theory of neutron scattering but, instead, is to provide the reader every basic notion to understand the rest of the manuscript. If the reader intends to go further in the understanding of the concepts treated in the following sections, he can refer to the general textbooks of neutron scattering and neutron vibrational spectroscopy [167–169].

The scattering cross section

In order to understand the basics of inelastic neutron scattering, and therefore to understand the concepts bridging the neutron-sample interaction and the associated measurement, we need to start from a simplified scattering experiment. Consider a monochromatic beam of thermal neutrons with an energy E_i, incident on a target (Fig 2.12). The target is a collection of atoms (crystal, amorphous solid, liquid or gas), and will be referred as the sample. In the case of inelastic neutron scattering the neutrons interacts with the sample by exchanging both energy and momentum. According to the laws of conservation, the total amount of energy and momentum remain unchanged

during the interaction, and we can then define the energy transfer $\hbar\omega$ and the momentum transfer $\hbar\overrightarrow{Q}$ as : $\hbar\omega = E_i - E_f$ and $\overrightarrow{Q} = \overrightarrow{k_i} - \overrightarrow{k_f}$. With E_i and E_f the energies of the neutron, respectively before and after the interaction with the sample, and $\overrightarrow{k_i}$ and $\overrightarrow{k_f}$ the wavevectors on the neutron, again, before and after being scattered.

Suppose we set up a neutron counter of small surface area dS and measure the number of neutrons scattered in the direction θ, ϕ as a function of their energy E_f. The distance of the counter from the sample is assumed to be large compared to the dimension of the counter and the sample, so the small solid angle $d\Omega$ is well defined. We can thus define that the intensity measured by the counter (*i.e.* the count rate) is equal to the partial differential scattering cross-section, and is defined by :

$$I_{counter} = \frac{N}{\Phi d\Omega dE_f} = \frac{d^2\sigma}{d\Omega dE_f} \tag{2.2}$$

Where N is the number of neutrons scattered per second onto the small solid angle $d\Omega$ with final energy between E_f and $E_f + dE_f$. Φ the flux of the incident neutrons in $\mathrm{neutron.cm^{-2}.s^{-1}}$.

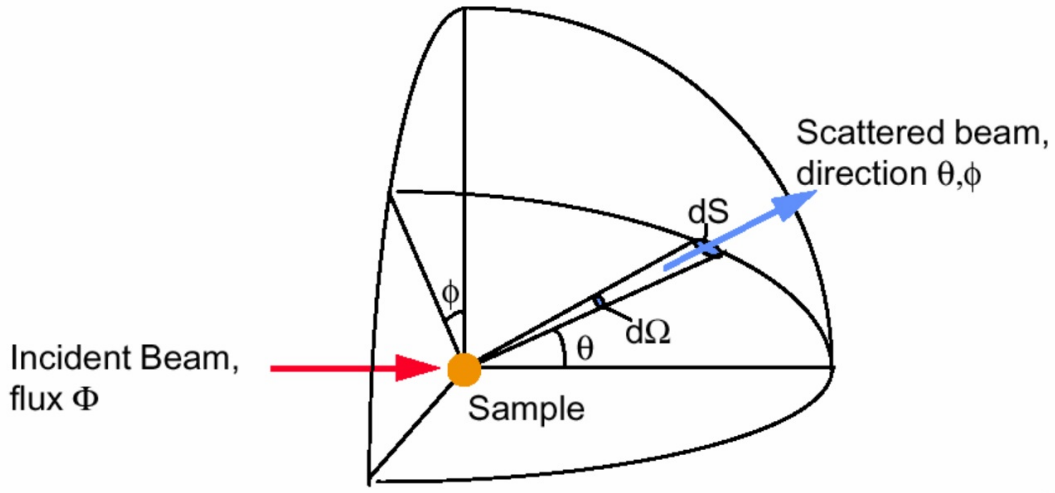

FIGURE 2.12: *A representation of a simple scattering experiment. The incident neutrons strike a sample and some neutrons are scattered in the direction θ, ϕ, toward a detector of small area (dS).*

The partial differential scattering cross-section $\frac{d^2\sigma}{d\Omega dE_f}$ represents the flux of neutrons per small solid angle $d\Omega$ that interact with a certain energy transfer $\hbar\omega$ and momentum transfer $\hbar\overrightarrow{Q}$. The partial differential cross-sections are the quantities actually measured in the scattering experiment. Therefore, we need theoretical expressions that allow to derive, from the latter, quantities of energy transfer and momentum transfer which would provide information about the structure and the dynamic of the studied sample.

Scattering from a single fixed nucleus

We consider the simple case of a nuclear scattering by a single nucleus fixed in position (elastic scattering). The nuclear forces which cause the scattering have a range of 10^{-14} to 10^{-15} m while the wavelength of thermal neutrons is in the order of 10^{-10} m. We take the origin to be at the position of the nucleus and the z axis along the direction of $\overrightarrow{k_i}$, the wavevector of incident neutrons. Then the latter can be represented by their wavefunction: $\Psi_{inc} = exp(ik_iz)$. The neutrons are plane waves and as any other kind of plane waves, the neutrons scattered by an object small compared to their wavelength, are scattered in the form of spherically symmetric waves. As the scattering is spherically symmetric, the wave function of the neutrons at the point **r** can be written as: $\Psi_{sc} = -\frac{b}{r}exp(ik_ir)$.

Where b is a constant known as the *scattering length* varying from one type of nucleus to an other and depends on their spin states as well. In this simple case it is shown that the total cross-section σ_{tot}, *i.e.* the cross section of the neutrons scattered in all direction and for all energies, is defined by :

$$\sigma_{tot} = \int_0^\infty \int_{all\,directions} \left(\frac{d^2\sigma}{d\Omega dE_f}\right) d\Omega dE_f = 4\pi b^2 \tag{2.3}$$

Fermi's golden rule

We consider now the nuclear scattering by a general system of particles, we consider the differential cross-section $\left(\frac{d\sigma}{d\Omega}\right)_{\lambda_i \to \lambda_f}$ representing the sum of all processes in which the state of the scattering system changes from λ_i to λ_f, and the state of the neutron changes from k_i to k_f (we voluntarily ignore the spin of the neutron so that its state is entirely defined by its momentum, and we don't have to account for magnetic interactions). The sum is taken for all the values of k_f in the small solid angle $d\Omega$, and we have thus :

$$\left(\frac{d\sigma}{d\Omega}\right)_{\lambda_i \to \lambda_f} = \frac{1}{\Phi}\frac{1}{d\Omega}\sum_{k_f} W_{k_i,\lambda_i \to k_f,\lambda_f} \tag{2.4}$$

Where, $W_{k_i,\lambda_i \to k_f,\lambda_f}$ is the number of transitions per second from the state k_i, λ_i to the state k_f, λ_f, and Φ is the flux of incident neutrons. In order to evaluate the expression on the right side of this equation we use a fundamental result of quantum mechanics known as the *Fermi's golden rule* that gives us :

$$\sum_{k_f} W_{k_i,\lambda_i \to k_f,\lambda_f} = \frac{2\pi}{\hbar}\rho_{k_f}|\langle k_f\lambda_f|V|k_i\lambda_i\rangle|^2, \tag{2.5}$$

where $\rho_{k'}$ is the number of momentum states in $d\Omega$ per unit energy range for neutrons in the state k'. The term between brackets represents the probability of transition from the eigenstate $|k_i\lambda_i\rangle$ to $|k_f\lambda_f\rangle$ under a perturbation. Finally, V is the interaction potential which represents the interaction between the neutron and the sample, and is obtained as the sum over all the atoms in the sample.

Expression for the double differential cross-section

We can rewrite the expression of the double differential cross section $\frac{d^2\sigma}{d\Omega dE_f}$ taking into account the exchange of energy and momentum in the simple

case of all the scattered neutrons have the same final energy:

$$\left(\frac{d^2\sigma}{d\Omega dE_f}\right)_{\lambda_i\to\lambda_f} = \frac{k_f}{k_i}\left(\frac{m}{2\pi\hbar^2}\right)^2 |\langle k_f\lambda_f|V|k_i\lambda_i\rangle|^2\ \delta\left(E_{\lambda_i} - E_{\lambda_f} + E_i - E_f\right) \tag{2.6}$$

Where, E_{λ_i} and E_{λ_f} are the initial and final energies of the scattering system and the δ-function is a mathematical term representing the energy distribution of the scattered neutrons.

We now insert a specific function for V. The core-neutron interaction is a short range force and can be described with the *Fermi pseudopotential* and can thus be expressed as :

$$V_j(\overrightarrow{Q}) = \frac{2\pi\hbar^2}{m} b_j \tag{2.7}$$

Where $V_j(\overrightarrow{Q})$ is the Fourier transform of the Fermi pseudopotential function $V_j(\overrightarrow{x_j})$ of the j^{th} nucleus, and b_j is the scattering length of the latter.

Using the definition of the pseudopotential $V(\overrightarrow{Q})$ and the Born approximation, that assumes that the interaction with a scatterer point is independent of the scattering of the other scatterers in the system, the probability for a neutron with a wavevector $\overrightarrow{k_i}$ being scattered by a potential $V(\overrightarrow{r})$ is proportional to :

$$\left|\int e^{i\overrightarrow{k_i}.\overrightarrow{r}}\ V(\overrightarrow{r})\ e^{i\overrightarrow{k_f}.\overrightarrow{r}}\ d\overrightarrow{r}\right|^2 = \left|\int e^{i\overrightarrow{Q}.\overrightarrow{r}}\ V(\overrightarrow{r})\ d\overrightarrow{r}\right|^2 \tag{2.8}$$

And we can then generalize equation 2.6, for all the processes and not only for the process where the system goes from a specific state λ to another λ':

$$\frac{d^2\sigma}{d\Omega dE_f} = \frac{k_f}{k_i}\frac{1}{2\pi\hbar}\sum_{jj'} b_{j'}b_j \int_{-\infty}^{\infty} \langle e^{-iQ.\overrightarrow{R_{j'}}(0)} e^{iQ.\overrightarrow{R_j}(t)}\rangle \times e^{-i\omega t} dt \tag{2.9}$$

Where $\overrightarrow{R_j}(t)$ and $\overrightarrow{R_{j'}}(t)$ are time-dependent Heisenberg operators containing H the Hamiltonian of the scattering system, and $\overrightarrow{R_{j'}}(0) = \overrightarrow{R_{j'}}$.

The equation 2.9 is the basic expression that bridge the measurements and the informations on the studied system. Indeed, we have related the measured cross-section $\frac{d^2\sigma}{d\Omega dE_f}$ to Heisenberg operators that contain Hamiltonians, containing themselves the properties of the scattering system. Moreover we expressed the cross section such as it depends on $\overrightarrow{Q}$ and ω which are quantities that can be known *via* the laws of conservation, $\hbar\omega = E_i - E_f$ and $\overrightarrow{Q} = \overrightarrow{k_i} - \overrightarrow{k_f}$.

Coherent and incoherent scattering

The coherent and incoherent scattering are important notions in neutron scattering and depend on the nature of the scattering nuclei. Consider a scattering system consisting of a single element where the scattering length b varies from one nucleus to another depending on the nuclear spin or the presence of isotopes or both. We define f_i the relative frequency with which the value b_i occurs. Then, the average value of b for the system is $\overline{b} = \sum_i f_i b_i$ and the average value of b^2 is $\overline{b^2} = \sum_i f_i b_i^2$. We can rewrite equation 2.9:

$$\frac{d^2\sigma}{d\Omega dE_f} = \frac{k_f}{k_i}\frac{1}{2\pi\hbar}\sum_{jj'}\overline{b_{j'}b_j}\int\langle j', j\rangle e^{-i\omega t}dt \tag{2.10}$$

where

$$\langle j', j\rangle = \langle e^{-i\overrightarrow{Q}.\overrightarrow{R_{j'}}(0)}e^{i\overrightarrow{Q}.\overrightarrow{R_j}(t)}\rangle \tag{2.11}$$

On the assumption there is no correlation between the b values of the different nuclei we can define that :

$$\overline{b_{j'}b_j} = (\overline{b})^2, \qquad \text{for} \quad j' \neq j.$$

$$\overline{b_{j'}b_j} = \overline{b^2}, \qquad \text{for} \quad j' = j.$$

so

$$\frac{d^2\sigma}{d\Omega dE_f} = \frac{k_f}{k_i}\frac{1}{2\pi\hbar}(\bar{b})^2 \sum_{jj'} \int \langle j', j\rangle e^{-i\omega t} dt + \frac{k_f}{k_i}\frac{1}{2\pi\hbar}\{\overline{b^2} - (\bar{b})^2\} \sum_{j} \int \langle j, j\rangle e^{-i\omega t} dt \quad (2.12)$$

$$= \left(\frac{d^2\sigma}{d\Omega dE_f}\right)_{coh} + \left(\frac{d^2\sigma}{d\Omega dE_f}\right)_{inc} \quad (2.13)$$

We see that the cross-section can be expressed such as it is composed of two terms, the first one which is know as the *coherent* and the second one as the *incoherent* scattering cross-section. We can then write :

$$\left(\frac{d^2\sigma}{d\Omega dE_f}\right)_{coh} = \frac{\sigma_{coh}}{4\pi}\frac{k_f}{k_i}\frac{1}{2\pi\hbar}\sum_{jj'}\int_{-\infty}^{\infty} \langle e^{-i\vec{Q}.\vec{R_{j'}}(0)} e^{i\vec{Q}.\vec{R_j}(t)}\rangle \times e^{-i\omega t} dt, \quad (2.14)$$

$$\left(\frac{d^2\sigma}{d\Omega dE_f}\right)_{inc} = \frac{\sigma_{inc}}{4\pi}\frac{k_f}{k_i}\frac{1}{2\pi\hbar}\sum_{j}\int_{-\infty}^{\infty} \langle e^{-i\vec{Q}.\vec{R_j}(0)} e^{i\vec{Q}.\vec{R_j}(t)}\rangle \times e^{-i\omega t} dt, \quad (2.15)$$

where $\sigma_{coh} = 4\pi(\bar{b})^2$ and $\sigma_{inc} = 4\pi\{\overline{b^2} - (\bar{b})^2\}$.

A real scattering system has different scattering lengths associated with different nuclei. The coherent scattering is thus the scattering the same nuclei (with the same positions and motions) would give if all the scattering lengths were equal to $\bar{b}$. While the incoherent scattering is the term that must be added to obtain the scattering of the real scattering system. In other words, the incoherent scattering arises from the random distribution of the scattering lengths from their mean value.

It is conventional to give the values $\bar{b}$ and $\overline{b^2}$ in terms of the two quantities σ_{coh} and σ_{inc}. Table 2.1 shows few values of σ_{coh} and σ_{inc} as examples for some elements. Those few values have been taken from the complete list of elements provided by Koester (1977)[170]. By looking at those values we understand why the neutron techniques are especially sensitive to hydrogen

Element	Z	σ_{coh}	σ_{inc}
^{1}H	1	**1.8**	**80.2**
^{2}H	1	5.6	2.0
C	6	**5.6**	**0.0**
O	8	4.2	0.0
Mg	12	3.6	0.1
Al	13	1.5	0.0

TABLE 2.1: Values of σ_{coh} and σ_{inc} for few elements. The units of σ_{coh} and σ_{inc} are *barns* ($10^{-28}\mathrm{m}^2$) and the values are taken from Koester (1977)[170].

atoms. Indeed, we see that the hydrogen owns a scattering cross-section of 82 barns (which is the largest among the periodic table of the element) and is mainly an incoherent scatterer ($\sigma_H^{inc} = 80.2$ barns). Comparatively, the carbon atoms, which are pure coherent scatterers, own a very small cross-section ($\sigma_C = \sigma_C^{coh} = 5.6$ barns). In the rest of the manuscript we will often consider that, as our samples all contains hydrogen atoms, the contributions of the other elements and the hydrogen coherent cross-section to the total cross-section are negligible. From now we will thus focus on the theory of INS concerning the incoherent scattering.

Incoherent inelastic scattering by crystals

We consider now the scattering system is a Bravais crystal (one atom per unit cell). Due to thermal motion, the nucleus is displaced form its equilibrium position l. Its position is $R_l(t) = l + u_l(t)$, where $u_l(t)$ is the Heinsenberg operator of u_l, the displacement from the equilibrium position. We assume that the interatomic forces in the crystal are harmonic. For such forces u_l can be expressed as the sum of displacements due to a set of normal modes.
Then part of the equation 2.15 can be expressed as:

$$\begin{aligned}\sum_j \int \langle e^{-i\vec{Q}.\vec{R_l}(0)} e^{-i\vec{Q}.\vec{R_l}(t)} \rangle \times e^{-i\omega t} dt \\ = N \int \langle e^U e^{V_0} \rangle e^{-i\omega t} dt, \end{aligned} \tag{2.16}$$

where N is the number of nuclei in the crystal, $U = -i\overrightarrow{Q}.\overrightarrow{u_0}(0)$, and $V_0 = i\overrightarrow{Q}.\overrightarrow{u_0}(t)$.

We find then the expression for the incoherent cross-section to be :

$$\left(\frac{d^2\sigma}{d\Omega dE_f}\right)_{inc} = \frac{\sigma_{inc}}{4\pi}\frac{k_f}{k_i}\frac{N}{2\pi\hbar}\, e^{\langle U^2\rangle}\int e^{\langle UV_0\rangle}e^{-i\omega t}dt \tag{2.17}$$

In the case the neutrons interact with the scattering system *via* a simple one-phonon process, *i.e.* the case of one neutron interact with one phonon, it is shown (from phonon expansion) that $e^{\langle UV_0\rangle} = \langle UV_0\rangle$.

The one-phonon incoherent cross-section is then defined by :

$$\begin{aligned}\left(\frac{d^2\sigma}{d\Omega dE_f}\right)_{inc\ 1\ ph} =& \frac{\sigma_{inc}}{4\pi}\frac{k_f}{k_i}\frac{N}{2\pi\hbar}e^{-2W}\sum_s \frac{(\overrightarrow{Q}\ .\ \overrightarrow{e_s})^2}{\omega_s} \\ &\times\{\langle n_s+1\rangle\delta\left(\omega-\omega_s\right)+\langle n_s\rangle\delta\left(\omega+\omega_s\right)\},\end{aligned} \tag{2.18}$$

where M is the mass of the scattering atom, ω_s is the angular frequency of mode s, e_s is its polarization vector, and n_s its quantum number. The exponential term $2W$ is known as the *Debye-Waller factor*, it is equal to $-\langle U^2\rangle$. The first term in the curly brackets corresponds to phonon emission (the scattering process in which the neutron creates a phonon in the s^{th} normal mode) and the second term corresponds to phonon annihilation (the scattering process in which the neutron annihilates a phonon in the s^{th} normal mode).

We may note that as the temperature tends to zero, $\langle n_s+1\rangle$ tends to one and $\langle n_s\rangle$ tends to zero. This is because when the crystal is at zero temperature all the normal-mode oscillators are at their ground states. Thus, there are no phonon to be annihilated.

Finally, for a given k_f, we get scattering from all the normal modes whose ω_s values satisfy $\omega = \omega_s$. The cross-section therefore depends on the number of modes that have the correct frequency, and we can express the incoherent

one-phonon cross-section in terms of the phonon density of states $g(\omega)$:

$$\left(\frac{d^2\sigma}{d\Omega dE_f}\right)_{inc\pm1} = \frac{\sigma_{inc}}{4\pi}\frac{k_f}{k_i}\frac{N}{4M}Q^2e^{-2W}\frac{g(\omega)}{\omega}\{\coth(\frac{1}{2}\hbar\omega\beta)\pm1\}, \tag{2.19}$$

where $\beta = \frac{1}{k_bT}$. With the equation 2.19, we see that by measuring the incoherent one-phonon scattering as a function of E_f we can determine the phonon density of state $g(\omega)$ of our scattering system.

Correlation functions in neutron scattering

The correlation functions are widely used in neutron scattering. They are not only useful for calculating various properties of the scattering system, but they also provide insight into the physical significance of the terms that occur in the scattering cross-section. For clarity we will focus on the incoherent scattering but the same principles apply to the coherent scattering. We define a function $I_{inc}(Q,t)$, known as the the *intermediate function*, by :

$$I_{inc}(\overrightarrow{Q},t) = \frac{1}{N}\sum_j \langle e^{-i\overrightarrow{Q}.\overrightarrow{R_j}(0)}e^{i\overrightarrow{Q}.\overrightarrow{R_j}(t)}\rangle \tag{2.20}$$

Similarly we define $S_{inc}(\overrightarrow{Q},\omega)$ the *incoherent scattering function*, by :

$$S_{inc}(\overrightarrow{Q},\omega) = \frac{1}{2\pi\hbar}\int_{-\infty}^{\infty} I_{inc}(\overrightarrow{Q},t)e^{-i\omega t}dt \tag{2.21}$$

Then, inserting those correlation functions in Equations 2.14 and 2.15 we obtain :

$$\left(\frac{d^2\sigma}{d\Omega dE_f}\right)_{coh} = \frac{\sigma_{coh}}{4\pi}\frac{k_f}{k_i}NS_{coh}(\overrightarrow{Q},\omega) \tag{2.22}$$

$$\left(\frac{d^2\sigma}{d\Omega dE_f}\right)_{inc} = \frac{\sigma_{inc}}{4\pi}\frac{k_f}{k_i}NS_{inc}(\overrightarrow{Q},\omega) \tag{2.23}$$

Alike the cross-section, we can define a function $S(\overrightarrow{Q},\omega)$ composed of the coherent and incoherent scattering functions, known as the *total dynamical structure factor*, such as:

$$S_{tot}(\overrightarrow{Q},\omega) = S_{coh}(\overrightarrow{Q},\omega) + S_{inc}(\overrightarrow{Q},\omega) \tag{2.24}$$

We see from equations 2.22 and 2.23 that the cross-section measured in neutron experiments is essentially the product of two factors. The first factor, σ, depends on the interaction between the neutron and the individual particles of the scattering system. The second factor, $S(\overrightarrow{Q},\omega)$, does not depend on the properties of the neutrons (mass, energy, etc.) but depends on the properties of the scattering system, and more specifically on the relative positions and motions of the particles in the system. These depend on the forces between the particle, and on the temperature of the system. Therefore, these equations allow to bridge the measurements and the properties of the studied samples, and illustrate quite well why neutrons are widely used for probing matter.

2.2.3 Specificities of IN1-LAGRANGE spectrometer

The IN1-LAGRANGE (LArge GRaphite ANalyser for Genuine Excitations) instrument [171] was chosen to investigate the vibrations of our sample on a wide energy range (26-500 meV), where the internal modes of the hydrogen atoms are expected.

IN1-LAGRANGE is an indirect geometry spectrometer (Figure 2.13) based on the space focusing of neutrons scattered by the sample (that can be cooled down to 5 K) in a very large solid angle, which are all recorded with a relatively small single counter (^{3}He detector). It is installed on the hot beam H8, having a direct view of the ILL hot source and it shares the primary spectrometer (constituted of a set of monochromators) with the D4 diffractometer. The primary spectrometer contains large double-focussing multi-face crystal

monochomators (Cu220, Cu331, Si111 and Si311) that supply the secondary spectrometer (IN1-LAGRANGE or D4) with a monochromatic neutron beam.

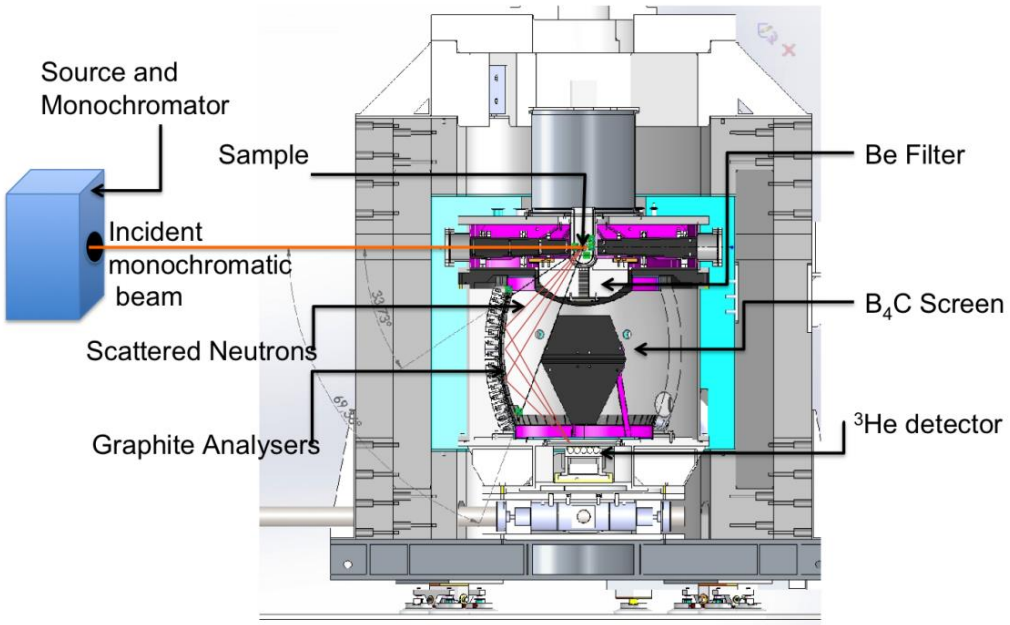

FIGURE 2.13: *Vertical cut of the IN1-LAGRANGE insert (secondary spectrometer)*

IN1-LAGRANGE uses a cooled Beryllium filter combined with a large area pyrolitic graphite (PG) space-focusing crystal analyzer, to collect the scattered neutrons over a large solid angle of 2.5 steradian. The combination of the filter and the crystal analyzer defines the final energy of the scattered neutron to 4.5 meV, making the final energy reaching the $^{3}\mathrm{He}$ detector fixed. The incident energy $\mathrm{E_i}$ is given by the Bragg angle between the monochomator face and the sample. It is a scanning instrument that changes its configuration at each energy step (at each $\mathrm{E_i}$). Indeed by moving both the monochromator and the secondary spectrometer on θ-2θ scans, IN1-LAGRANGE is allowed to take advantage of the whole energy range provided by the hot source and to scan from 1 meV to 1 eV (with different monochromators).

Due to its peculiar geometry, the spectrometer probes a relatively thick region in $(\overrightarrow{Q}, \omega)$ (see fig. 2.14) owing to the relative large scattered angles collected. However the $\overrightarrow{Q}$ domain available at each energy transfer is integrated at the detector, so that no $\overrightarrow{Q}$ dependence on the scattering can be analyzed, but the integration results in a very intense signal. Moreover, its geometry is such that the spectrometer works at relatively high values of $\overrightarrow{Q}$ (large $\overrightarrow{k_i}$ and low $\overrightarrow{k_f}$), meaning that all scattering involves the exchanging energy of the scattering atoms. In such conditions, as the neutron energy rises, the elastic cross section falls, the inelastic cross section rises and the incoherent approximation is valid. The dynamic response of the scattering system can then be calculated simply by treating the scattering as **inelastic** and **incoherent**.

Finally, the measured intensity is directly proportional to the generalized phonon density of states ($\mathrm{GDOS_{exp}}$), which allows a direct comparison with the calculated neutron spectra[172, 173]. The experiments were performed using the Cu220 and Cu331 monochromators. With such a configurations the incident energy ($\mathrm{E_i}$) was scanned from 26 meV up to 500 meV and the energy resolution was around 1.5 - 2% of $\mathrm{E_i}$.

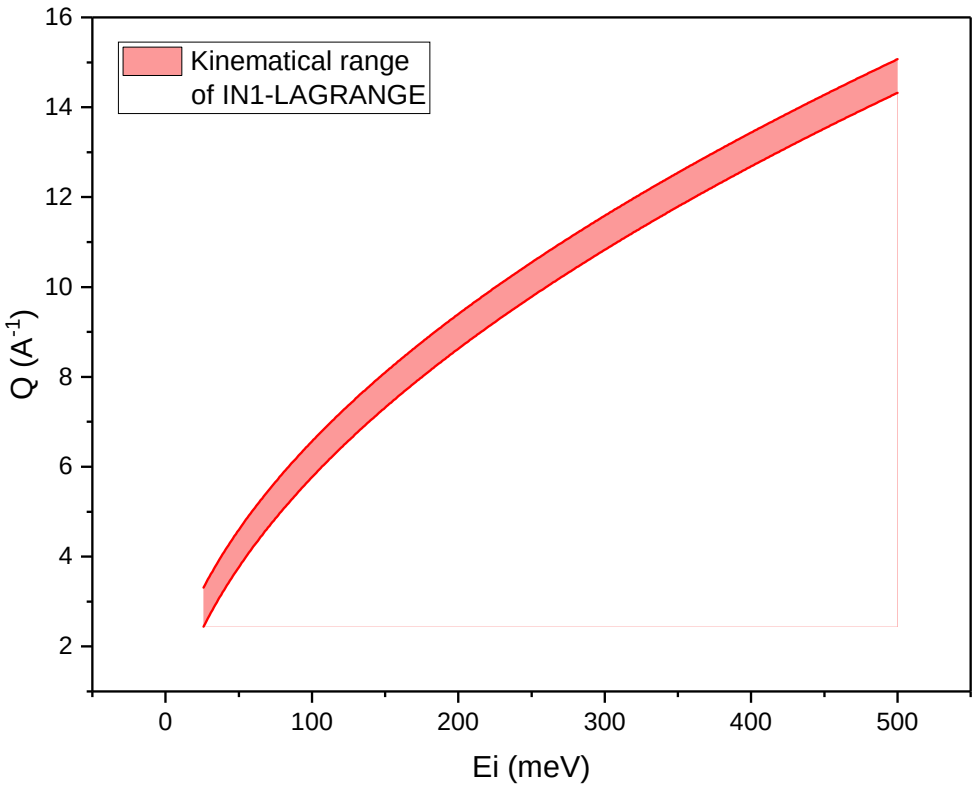

FIGURE 2.14: *Kinematical range of IN1-LAGRANGE over its wide scanning energy range (26-500 meV). It represents the (Q, ω) region accessible with the spectrometer.*

2.3 Density Functional Theory calculations

We introduced in section 2.2.1 that one of the many advantages of neutron techniques is that they can be relatively easily modeled by computer simulations. Indeed, nowadays, with the growth of computer capacities and performance, the simulations of complex molecular systems have been rendered possible. Therefore the experimental data are quasi-systematically analyzed and discussed jointly with the results of numerical modeling and simulations.

In the context of this thesis, the main goal of the numerical simulations is to calculate the vibration frequencies of the atoms in our samples, based on hypothetical models that represent at best the materials under study. With

the calculated vibration frequencies, we can confront the simulated and experimental results in order to have a better understanding of the interactions between atoms in our samples, and therefore, increase our chances of answering to the fundamental questions raised here. In order to obtain these vibration frequencies we used a very common numerical approach based on the *Density Functional Theory* (DFT), and that aims at calculating the vibrations of a given arrangement of atoms, called *Lattice Dynamics* (LD). In this section we develop the basic concepts of the DFT and the Lattice dynamics, and we advise any interested reader who would like to have the full details about those numerical tools to refer to the following very good books and papers: [174–176] (DFT) and [177–179] (Lattice Dynamics).

2.3.1 The principle of DFT

Density Functional Theory (DFT) is one of the most popular and successful quantum mechanical approach for materials modeling problems in physics, chemistry, materials science and some branches of engineering. The good balance between its high efficiency and its relatively high accuracy is the main reason of its still growing success. In many-body quantum theory (such as Hartree-Fock (HF) methods [180–182]) the wavefunction (Ψ) is the fundamental variable that contains all the information on the state of a system and from which the resolution of the time-independent Schrödinger equation, $\hat{H}\Psi = E\Psi$, allows to derive values of the observable of interest. The major drawbacks of the HF methods comes from the fact that they ignore the correlated motion of each electron with every others, which has an impact on their accuracy, and that they have a lack of computational efficiency, which troubles the calculations performed on large systems.

The main idea behind the DFT is that the one-electron density ρ is used as the basic variable to describe the systems. The strength of the DFT is that ρ is

a function of the three space coordinates only, *i.e.* :

$$\rho = \rho(r), \tag{2.25}$$

and that the complex mathematical object Ψ (wavefunction) is replaced by the much simpler quantity ρ. If the Ψ in many-body theory methods is a function of $3\mathrm{N}$ coordinates ($4\mathrm{N}$ if the spin is taken into account), N being the number of electrons in the system, ρ is a function of three spacial variables which renders the electronics problem solvable for systems containing more than few atoms. So, for example, for a nanocluster of 100 Pb atoms the DFT reduces the problem from something with more than 23000 dimensions to a problem with just 3 dimensions.

2.3.2 The Hohenberg-Kohn-Sham formulation of DFT

Even if the basis of DFT were set already by L. Thomas and E. Fermi in 1928 [183, 184], the real formulation was provided by P. Hohenberg and W. Kohn (HK) in 1964 with their two fundamental theorems [185]. And in 1965, Hohenberg, Kohn and Sham (HKS) introduced a proof of these theorems by showing that the DFT was an exact theory in the same sense as the multi-body theories [186].

In HKS formulation, instead of using the full electronic wavefunction Ψ_0, the electronic ground state of a system can be entirely described by its electron density $\rho(r)$. Based on the second HK theorem, that relates the non-degenerated ground-states density ρ_0 to the ground-state energy E_0 by stating that the energy functional $E[\rho]$ is universal for $\rho = \rho_0$, the exact ground-state density is obtained by minimizing $E[\rho]$ with respect to ρ in order to find $E[\rho] = E_0$.

In the Kohn-Sham (KS) approach, the fully interacting many-body system

is replaced by an ensemble of virtual particles in a modified potential $V(r)$ characterized by the same density ρ as the real electronic system, and the total energy functional $E[\rho]$ can be written as:

$$E[\rho] = T_s[\rho] + V_{ext}[\rho] + E_H[\rho] + E_{xc}[\rho], \tag{2.26}$$

where $T_s[\rho]$ is the non-interacting kinetic energy, $V_{ext}[\rho]$ is the external potential, $E_H[\rho]$ is the Hartree energy (representing the classical Coulomb interaction of an interacting charge density $\rho(r)$), and $E_{xc}[\rho]$ is the exchange-correlation functional and takes into account the correlation part that is missing in the HF methods. The advantage of this decomposition, given by the KS approach, is that $T_s[\rho]$ and $E_H[\rho]$ are given by exact expressions. In practice, KS equation is solved using an iterative self-consistant procedure that aims at calculating the exact ground-state and energy by finding $\rho(r)$ such that :

$$\frac{\delta E[\rho]}{\delta \rho} = 0, \tag{2.27}$$

with the condition :

$$\int \rho(r) dr = N \tag{2.28}$$

where N is the number of electron in the system.
Note that the $E_{xc}[\rho]$ is often divided into two contributions, an exchange term and a correlation term :

$$E_{xc}[\rho] = E_x[\rho] + E_c[\rho], \tag{2.29}$$

where the exchange energy $E_x[\rho]$ of a system of electrons is associated with the Pauli exclusion principle (because two electrons with the same spin must have a spatial separation, the electron-electron repulsion energy is reduced). And the correlation energy $E_c[\rho]$ is taking into account the correlated motion of each electron with every other.

However, the exact expression of E_{xc} is not known and thus approximate formulas are needed. Several approximations approaches have been developed to improve the exchange-correlation functional, each approach presents its own advantages and disadvantages and this is the reason why we find nowadays a wide variety of developed functionals. Nevertheless they can be classified in different classes depending on the type of approximation they are based on: the local density approximations (LDA), the generalized gradient approximations (GGA), the meta-GGA and the hybrid ones.

The Local Density Approximation (LDA)

The simplest approach used to approximate the exchange-correlation functional is the LDA. In this approximation, the value of $E_{xc}[\rho]$ is approximated by the exchange-correlation energy per electron ε_{xc} in an uniform electron gas of the same density $\rho(r)$:

$$E_{xc}^{LDA}[\rho(r)] = \int \varepsilon_{xc}[\rho(r)]\rho(r)dr, \tag{2.30}$$

and where $\varepsilon_{xc}[\rho] = \varepsilon_x[\rho] + \varepsilon_c[\rho]$.

The $\varepsilon_x[\rho]$ and $\varepsilon_c[\rho]$ are usually interpolated analytically by Quantum Monte Carlo (QMC) methods. Despite the success of the LDA methods, that made the popularity of the DFT calculations, they present some limitations for inhomogeneous systems such as molecular materials. For instance, in strongly correlated systems LDA is very inaccurate. Moreover it does not account for the van der Waals interactions at all and gives very poor description of hydrogen bonding systems. Functionals with other forms were then needed.

The Generalized Gradient Approximation (GGA)

In order to improve the LDA, it has been developed a gradient correction to the E_{xc} expression which gave raise to the GGAs methods. Practically, it is done by rendering the E_{xc} a functional of both the density $\rho(r)$ and its gradient $\bigtriangledown\rho(r)$. Therefore the exchange-correlation energy of the GGAs methods takes the general form of:

$$E_{xc}^{GGA}[\rho(r)] = \int f_{GGA}\left\{\rho(r), \bigtriangledown\rho(r)\right\} dr. \tag{2.31}$$

For many properties, for example optimized geometries, ground state energies of molecules and solids, covalent bonds and weakly bonded systems, the GGAs methods often gives better results than the LDAs. Several GGA functionals have been developed so far and, depending on the studied system, can provide a relatively good accuracy. We can cite few of the most popular gradiant corrected correlation functionals wich are widely adopted, such as: the PBE (Perdew, Burke and Ernzerhof) functional[187], which have been widely used for the calculations of this thesis, the PW91 (Perdew and Wang) functional[188, 189] and the LYP (Lee-Yang-Parr) functional[190].

Other types of functionals

A number of new f_{GGA} functionals include a third generation which uses the second derivative of the density $\triangle\rho(r)$ and/or kinetic energy densities $\tau(r)$ as additional degrees of freedom. They belong to the class called meta-GGAs functionals.

And a forth generation which adds "exact exchange" calculated from the Hartree-Fock exchange, that are called hybrid functionals, and for instance that are mixing a portion of the exact Hartree-Fock exchange to a LDA- or GGA-type functionals. A good example of this type of functional that could

be mentioned is the very popular B3LYP[191].

Figure 2.15 below summarizes the characteristics and the successive improvements made building an accurate universal density-based approach.

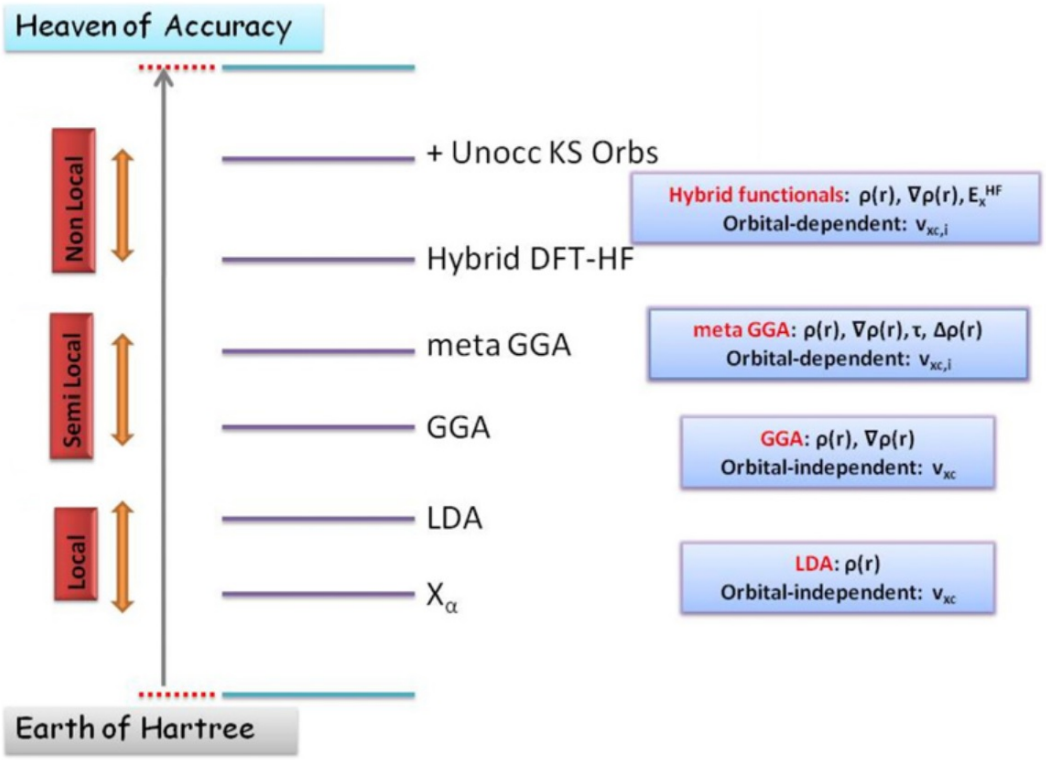

FIGURE 2.15: *Schematic illustration of Perdew's view of the hierarchy of DFT approximations. Taken from [176].*

2.3.3 The Lattice Dynamics

The subject of the *lattice dynamics* (LD) is the study of the vibrations of the atoms in crystals, but finds applications for various types of materials. For instance, in our case we made advantage of the periodicity in order to simulate infinite carbon nanotubes along one dimension, allowing us to model long CNTs, using a reasonable number of carbon atoms.

In this section, we will give the important notions about the lattice dynamics for a crystalline system, in order to understand how does the LD method allow to obtain vibrational information from a virtual atomic model. These

concepts are actually applicable to any virtual collection of atoms within a unit cell.

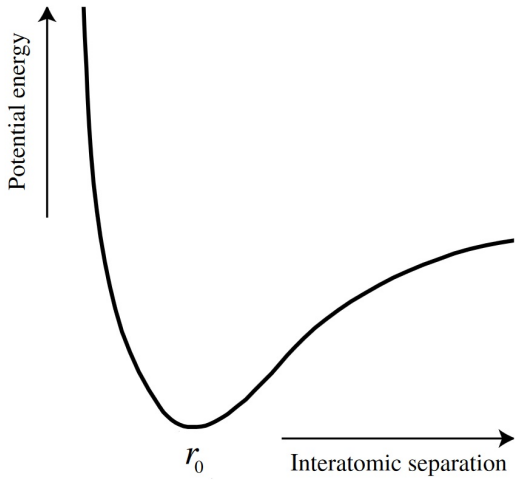

FIGURE 2.16: *Classical potential energy curve for two atoms, showing a minimum at separation at r_0 that might correspond to the bond length. This plot is a simplification of the situation within a crystal. Taken from [179].*

The harmonic approximation

The key approximation in the theory of lattice dynamics is the *harmonic approximation*. This is illustrated by considering the potential energy between two atoms, as shown in Figure 2.16. The energy can be written as a Taylor expansion around the minimum point r_0:

$$E(r) = E_0 + \frac{1}{2}\left.\frac{\delta^2 E}{\delta r^2}\right|_{r_0}(r-r_0)^2 + \frac{1}{3!}\left.\frac{\delta^3 E}{\delta r^3}\right|_{r_0}(r-r_0)^3 + \frac{1}{4!}\left.\frac{\delta^4 E}{\delta r^4}\right|_{r_0}(r-r_0)^4 + \ldots \tag{2.32}$$

where the derivatives are performed at $r = r_0$. The harmonic approximation consists in neglecting all the terms of power higher than 2.

The total energy E of a crystalline collection of atoms in a lattice can be defined by :

$$E = \frac{1}{4}\sum_{n,n'}\sum_{j,j'}\phi^{j,j'}_{n,n'}(u_{j,n} - u_{j'n'})^2 = \frac{1}{2}\sum_{n,n'}\sum_{j,j'}u_{j,n}\Phi^{j,j'}_{n,n'}u_{j'n'} \tag{2.33}$$

where $\phi^{j,j'}_{n,n'}$ is the differential of an individual bond energy with respect to the displacements of the atoms within the bond, $\Phi^{j,j'}_{n,n'}$ is the differential of the overall energy with respect to the atomic displacement. The labels n and n' denote unit cells, and the labels j and j' denote the atoms in the unit cell. And where the displacement of any atoms in the unit cell can be described by the following equation of motion :

$$u_{j,n}(t) = \tilde{u}_j \exp(i(kna - \omega t)) \tag{2.34}$$

where $\tilde{u}_j$ is the relative amplitude of motion of the atoms and a is the length unit cell labelled n.
From simple Newton's equations, $force = mass \times acceleration$, we can write a general equation of motion for our system:

$$\omega^2 e_j = \sum_{j',n'} \frac{1}{\sqrt{m_j m_{j'}}} \Phi^{j,j'}_{n,n'} e^{ik(n'-n)a} e_j \tag{2.35}$$

That can be expanded in the form of a matrix equation :

$$\omega^2 \overrightarrow{e} = D(\overrightarrow{k}) \cdot \overrightarrow{e} \implies \omega^2 = \overrightarrow{e}^T \cdot D(\overrightarrow{k}) \cdot \overrightarrow{e} \tag{2.36}$$

where

$$\overrightarrow{e} = \begin{pmatrix} \vdots \\ e_j \\ \vdots \end{pmatrix} \tag{2.37}$$

and

$$D_{j,j'}(\overrightarrow{k}) = \frac{1}{\sqrt{m_j m_{j'}}} \sum_{n'} \Phi^{j,j'}_{0,n'} e^{i\overrightarrow{k}.(\overrightarrow{r}_{j,0} - \overrightarrow{r}_{j',n'})} \tag{2.38}$$

$D(\overrightarrow{k})$ is the *dynamical matrix* of the system and m is the mass of the atom.

Equations 2.36 is a simple eigenvalue/eigenvector equation, with the matrix of solutions ω^2 representing the eigenvalues of $D(k)$ and the matrix of e representing the eigenvectors. This step is commonly referred as the *diagonalisation of the dynamical matrix* of the system. Then, from the eigenvectors and the eigenvalues, the atomic displacements and their amplitudes in real space can be expressed in terms of normal modes coordinates in the reciprocal space. Therefore, the frequencies of the normal modes can be calculated, and by performing a summation over all modes *via* the generation of a list of frequency values for a grid of wave vector. If the grid is sufficiently fine, it is possible then to generate a histogram of frequency values, and such an histogram is called the **density of states** $\mathrm{g}(\omega)$.

This $\mathrm{g}(\omega)$ is actually the sum of the individual atomic contribution to the vibrational density of states and is defined by $\mathrm{g}(\omega) = \sum_i \mathrm{g_i}(\omega)$. Where the label i denote the atomic element.

Before being able to compare it with the experimental generalized density of states $\mathrm{GDOS_{exp}}$ (result of the INS experiments) it is necessary to calculate a theoretical generalized density of states ($\mathrm{GDOS_{th}}$) taking into account the individual atomic contributions **weighted by their respective neutron cross section and mass**, and defined by $\mathrm{GDOS_{th}} \propto \sum_i \frac{\sigma_\mathrm{i}}{\mathrm{m_i}} \mathrm{g_i}(\omega) \mathrm{e}^{-2\mathrm{W_i(Q)}}$, where σ_i indicate the experimental individual cross section, m_i is the mass and $W_i(Q)$ is the Debye-Waller factor for the atom i. Since the hydrogen scattering cross section is very large compared to the other atoms of our models, the individual contributions of any atoms are often considered negligible compared to those of hydrogen in the case of INS measurements, and the $\mathrm{GDOS_{th}}$ can be then approximated such as $\mathrm{GDOS_{th}} \approx \mathrm{g_H}(\omega)\mathrm{e}^{-2\mathrm{W_H(Q)}}$, where $\mathrm{g_H}(\omega)$ is known as the **hydrogen partial density of states**.

2.4 X-ray Photoelectron Spectroscopy

2.4.1 Principle

The X-ray Photoelectron Spectroscopy (XPS) technique is commonly used for surface analysis. Because it uses photons (soft X-rays) as a probe, the penetration depth in the materials does not exceed usually a few nanometers. Nevertheless it is a powerful technique that presents many advantages. The surface analysis by XPS is accomplished by irradiating a sample with mono-energetic soft X-rays and analyzing the energy of the core electrons emitted from the sample (see Figure 2.17). Indeed, these photons interact with atoms in the surface region, causing core electrons to be emitted by photoelectric effect.

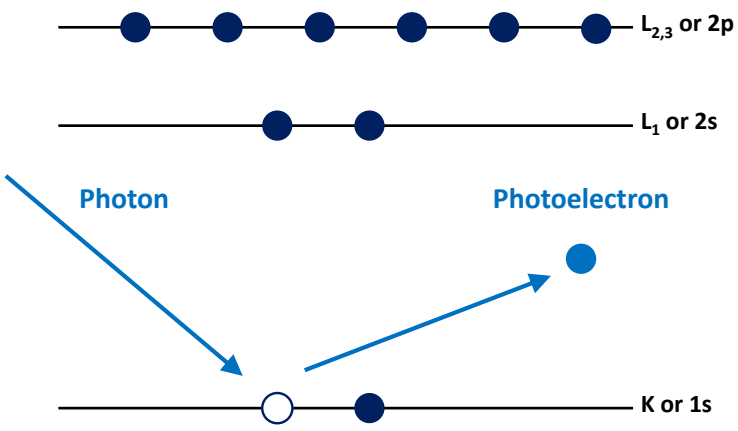

FIGURE 2.17: *Illustration of the photoelectric effect on one core electron.*

The emitted electrons have then a kinetic energy given by :

$$KE = h\nu - BE$$

Where $h\nu$ is the energy of the photon and BE is the binding energy of the atomic orbital from which the electron originates.

It is then easy to have access to the original binding energy of the electron knowing the incident photon energy and measuring the kinetic energy of the emitted photoelectron. And, because each element has a unique set of binding energies, XPS can be used to **identify and determine the concentration of elements** at the surface of a given sample. In addition, small variations of the elemental binding energy can be found and exploited. Indeed those variations in the elemental binding energies arise from differences in the chemical bonding of the element. This change in core electron binding energies, so-called "chemical shift" can be explained by the effective charge potential change on an atom when bonded to another one. It is therefore possible to have access to the bonding state of the studied element, meaning that the chemical shifts can be used to **identify the neighboring or the chemical state of the atoms of interest**.

2.4.2 Instrumentation

The basic components of a typical XPS instrument are schematically shown in Figure 2.18. Commonly it is composed of an ultrahigh vacuum (UHV)-based stainless steel chamber containing the sample stage, an electron energy analyzer and an X-ray source (with or without monochromator). Frequently there are additional devices like, for example, a sample preparation chamber or an ion source for sample cleaning or depth profiling.

X-ray Sources

The most common X-ray sources used in XPS are equipped with Mg or Al anodes. The characteristic Mg K_α radiation at 1253.6 eV and the Al K_α radiation at 1486.6 eV possess sufficiently high energy for core level electron emission as well as a sufficiently low spectral line width (less than 1 eV) to provide XPS spectra with a good resolution. A thin foil of Aluminium is placed at the

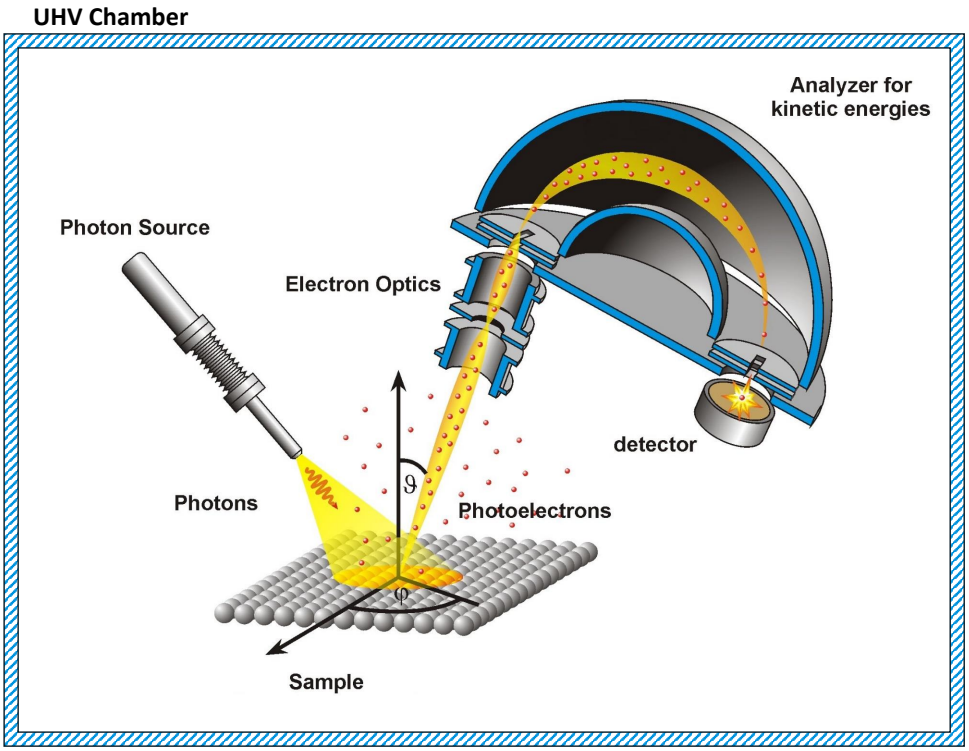

FIGURE 2.18: *Main components of a typical XPS instrument*

exit of the X-rays source to shield the sample from parasitic electrons emitted by the source, from contamination and from the radiative heat from the anode. This type of X-ray source produce a main emission line together with minor lines at higher binding energy. Indeed, the K_α line of the usual Mg and Al sources consists in a main doublet peak $K_{\alpha 1,2}$, further satellite peaks and a K_β line. If the $K_{\alpha 5,6}$ and the K_β lines owns negligible intensity, the $K_{\alpha 3,4}$ possesses together about 10% intensity of the main line and are about 10 eV shifted to lower binding energy (see Table 2.2). These satellites contribute to distort the spectra and have to be taken into account when it comes to data analysis.

K lines		$\alpha_{1,2}$	α_3	α_4	α_5	α_6	β
Mg	Rel. intensity (%)	100	8.0	4.1	0.55	0.45	0.5
	Energy displacement (eV)	0	8.4	10.2	17.5	20.0	48.5
Al	Rel. intensity (%)	100	6.4	3.2	0.4	0.3	0.55
	Energy displacement (eV)	0	9.8	11.8	20.1	23.4	69.7

TABLE 2.2: X-ray Satellites energies and intensities for Mg and Al sources [192].

Electron Energy Analyzer

The Electron Energy Analyzer (EEA) is maybe the most important part of an electron spectrometer. From its quality depends the quality and the precision of the measurement. Three different types of electrostatic analyzers are most common in commercial electron spectroscopic instruments: the Retarding Field Analyzers (RFA), the Concentric Hemispherical Analyzers (CHA) and Cylindrical Mirror Analyzers (CMA). The RFA acts as a high-pass filter that cut off all the electrons below a certain energy, while the CHA and CMA are deflection analyzers and operate like band-pass filters that select electron having energies comprised in a certain choosen small energy window. Therefore, CHA and CMA have intrinsically a better signal-to-noise feature and an higher sensitivity than the RFA type. That leaves the RFA used for special applications (AES, PECVD ...).

2.4.3 Measurements

Sampling depth

The sampling depth is defined as the depth from which 95% of all photoelectrons are scattered by the time they reach the surface of the sample, and therefore as the depth from which 95% of all the photoelectrons do not reach the analyzer. This depth is directly linked to the inelastic mean free path (IMFP) of an electron in a solid, and is approximately three times this IMFP. As the IMFP depends mostly on the kinetic energy of the photoelectron it is

possible to establish the relation between the IMFP and the corresponding kinetic energy. Figure 2.19 represents the "universal curve" that relate the kinetic energies of the electrons to their IMFP in a solid (taken from[193]).

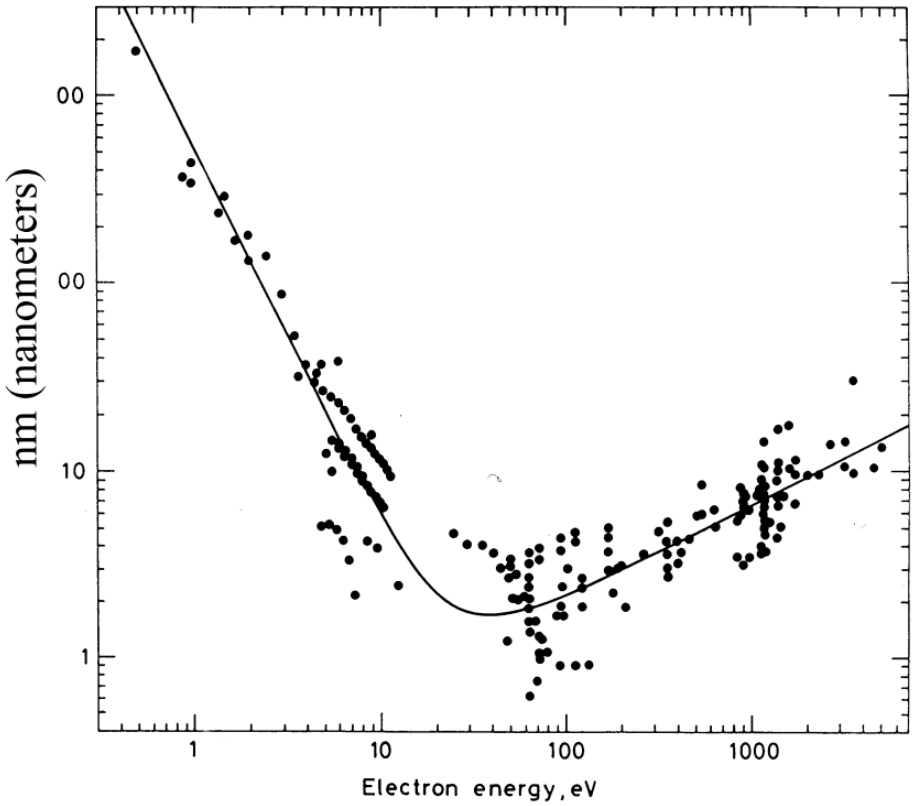

FIGURE 2.19: *Universal curve for the inelastic mean free path of electrons in a solid [193].*

For example, the core level photoelectrons owns a kinetic energy of approximately 100-500 eV. According to figure 2.19 we see that to this energy corresponds an IMFP of approximately 1-3 nm. We can then easily find the sampling depth to be: Sampling depth $= 3 \times$ IMFP $=$ 3-9 nm. This sampling depth is typically what we can expect to probe in our samples using the Mg K_α radiation at 1253.6 eV or the Al K_α radiation at 1486.6 eV.

Typical XPS spectrum

Figure 2.20 below, shows the typical XPS spectrum obtained for the fluorescein isothiocyanate (FITC) by means of the Mg K_α radiation at 1253.6 eV. It illustrates quite well the information we can obtain with such a technique.

The FITC is a molecule composed of hydrogen, carbon, oxygen, nitrogen and sulfur atoms only and, as we clearly see on figure 2.20, these different atoms can be discriminated on the spectrum since their core electrons own very different bonding energies. Indeed, the peaks labeled "C1s" "N1s" "O1s" and "S2p" corresponds respectively to the detection of the core photoelectron from the 1s orbital of the carbon, nitrogen and oxygen atoms, and from the 2p orbital of the sulfur atoms. The hydrogen is obviously not present on the spectrum since it does not have a core electron and so will not produce a core photoelectron in this range of binding energy. Nevertheless, from this type of spectrum we are able to identify the different elements composing our samples via the characteristic binding energies of their core orbitals. Afterwards, by measuring specifically the range of an element of interest with a better resolution we can obtain information about its surrounding by looking at the so-called "chemical shift".

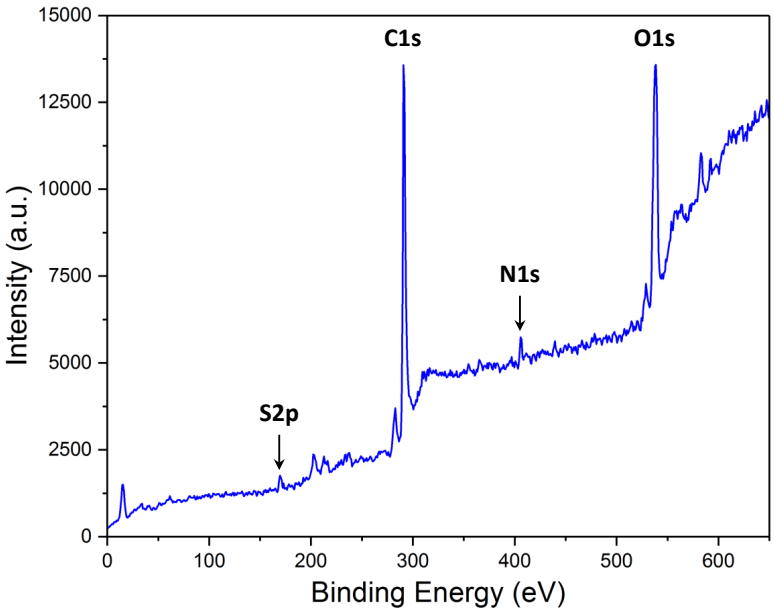

FIGURE 2.20: *Typical XPS spectrum of the fluorescein isothiocyanate in the binding energy range of 0-650 eV and measured with an Mg K_α radiation at 1253.6 eV.*

Chemical Shift

As it has been mentioned before, XPS technique allows to identify the neighboring of a given element by measuring its chemical state, and measuring the so-called "chemical shift" of the peaks. Indeed, from a well known peak position attributed to a specific element with a specific surrounding, it is possible to observe shift in peak position when the surrounding of the element is different.

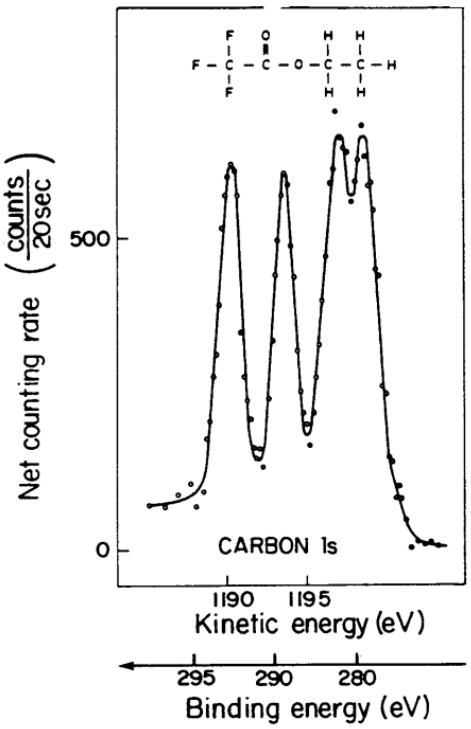

FIGURE 2.21: *XPS spectrum in the C1s region of the Ethyl Trifluoroacetate[194].*

For instance, when an atom is bonded to another one with higher electronegativity a charge transfer to the latter occurs and the effective charge of the former becomes positive, and thus increasing the binding energy. On the contrary, the binding energy of the atom with higher electronegativity is decreased. With the help of data bases, it is then possible to attribute these chemical shifts to a specific surrounding, and obtain qualitative information on the composition of the sample. Figure 2.21 gives an example for the use of the chemical shift. On this plot of the carbon 1s orbital (C1s) analysis of the Ethyl Trifluoroacetate [194], we see that the different carbon atoms of the molecule are responsible for different specific peak depending on their direct surrounding and can thus be discriminated.

Quantification

Beside the discrimination of the elements and their surrounding, one of the strength of the XPS techniques is to allow quantitative measurements. Indeed, the measured intensities of the photoelectrons is define by:

$$I_i = N_i \sigma_i \lambda_i K, \tag{2.39}$$

where I_i is the intensity of a photoelectron peak "p" for the element "i", N_i is the average atomic concentration of the element "i" in the surface analyzed, σ_i is the photoelectron cross section for the element "i", λ_i is the inelastic mean free path of a photoelectron from the element "i", and K represents all the other factors related to quantitative detection of a signal and is assumed to remain constant during a given experiment. We see that the parameters σ_i and λ_i depend on the element but also depend on the materials analyzed. Therefore, for a unique experiment on a sample surface, we can consider them only depending on the element and can be gathered with K in a unique factor S_i defined as the atomic sensitivity factor. We thus find the atomic concentration N_i to be:

$$N_i = \frac{I_i}{S_i}, \tag{2.40}$$

If S_i vary from a material to an other, the S_i ratio between two element ($\frac{S_1}{S_2}$) is nearly constant. Thus, for any spectrometer, it is possible to develop a set of relative values of S for all the element. From equation 2.41 we see then that we can easily find the relative proportions of two elements in a materials by simply knowing the $\frac{S_1}{S_2}$ ratio and their relative intensity using the following equation:

$$\frac{N_1}{N_2} = \frac{I_1/S_1}{I_2/S_2}, \tag{2.41}$$

It becomes even easier when it comes to know the relative proportions of the different contributions to the chemical shifts of a single element. Indeed, in this case the sensitivity factors of equation 2.41 are equal and the equation become, for two contributions peak "p1" and "p2" to the same element orbital:

$$\frac{N_{p1}}{N_{p2}} = \frac{I_{p1}}{I_{p2}}, \tag{2.42}$$

Finally, in practice we prefer to use the area of the peaks instead of the intensity, in order to increase the precision of the quantification with XPS techniques. Indeed using the peak's areas allow to better take into account the effects of the background and the experimental resolution on the measured spectra. If, at this point, the reader is interested in more details about the XPS Instrumentation or XPS measurement, we recommend the very good book of S. Hofmann, "Auger- and X-Ray Photoelectron Spectroscopy in Materials Science" [195] where all the concepts above are developed extensively.

Chapter 3

Experiments

In this chapter we focus on the analysis of the grafting of the two fluorophores selected for this Ph.D. project, the FITC and the Cyanine. Indeed, we aim here at investigating the differences in between this two fluorophores in terms of covalent grafting efficiency when they are grafted onto DWNTs. First, the FITC is commonly used for tracking the CNTs *via* fluorescence techniques and, therefore, knowing the proportions of covalently and non-covalently grafted molecules present a direct interest to determine the reliability of such techniques. Then, the Cyanine which is rarely used because of its higher cost, present nevertheless a huge interest in our study. Indeed, the Cyanine exhibits a very different geometry from the FITC and offers us the possibility to investigate the influence of the fluorophore's geometry on the grafting process.

This chapter is divided in three parts. The first part presents the experimental results obtained for the study of the grafting of FITC onto DWNTs using two differents spectroscopic techniques, the X-ray photoelectron spectroscopy (XPS) and the inelastic neutron scattering (INS) spectroscopy that allow to probe respectively the surface and the bulk of our samples. The second part presents the experimental results obtained for the study of the grafting of the Cyanine onto DWNTs using the same techniques. The reader must not be surprised by the similarities between the two first parts of this chapter since the experiments were performed with the same techniques and

under the same conditions in order to allow us to compare the grafting process of the two fluorophores. Finally, the third part focuses on the computational investigation of the energies involved in the non-covalent grafting of the fluorophores onto DWNTs, and attempt to pave the way for the potential furthers computational investigations.

3.1 Study of the grafting of the Fluorescein Isothiocyanate

3.1.1 X-ray Photoelectron Spectroscopy

The XPS measurements were performed using a standard ultrahigh vacuum (UHV) chamber with a base pressure of $1x10^{-10}$ mbar equipped with an hemispherical analyzer and a non-monochromatic dual Mg/Al x-ray source. For the present measurements the Mg anode was used providing X-ray photons with energy of 1253.6 eV. As the sample are powders, we used copper adhesive tape to stick them to the sample holder which is made of molybdenum. Both the adhesive and the sample holder are conductive materials allowing the charges to be evacuated. Samples were pumped down overnight within the XPS load lock chamber ($1x10^{-8}$ mbar) prior to introduction into the analysis chamber. The experimental XPS spectra have been fitted with Voigt functions using a fixed Gaussian width of 0.8 eV corresponding to the overall experimental resolution. For each spectrum the same procedure was followed using the software "UNIFIT". First the satellites and the Background were removed. The XPS spectra obtained for each sample were then shifted in energy to compensate charge effects. The C1s orbital main C-C peak was centered at 284.6 eV accordingly to the literature. Then, the appropriate number of components used for fitting the different contributions

to each spectrum were chosen according to the number of Nitrogen containing chemical groups in the sample. Finally, one sample of pure FITC and the sample "DWNT-diamine" were measured as references and the results so obtained were used to fit the results obtained for the sample "DWNT-diamine-FITC".

For all the spectra, the fit was considered converged when the χ^2 tolerance was reached and was equal to 1.10^{-9}.

FITC

A FITC molecule contains only one type of Nitrogen involved in a $-\mathrm{NCS}$ chemical group (see inset of Fig. 3.1-a). The peak position, the area and the Lorentzian full width at half maximum (wL) were let unconstrained during the fitting procedure.

Figure 3.1-a shows the result of the XPS measurement of the FITC in the N1s orbital binding energy region (blue marked line) and displays the result of the peak fitting following the procedure mentioned above (green line).

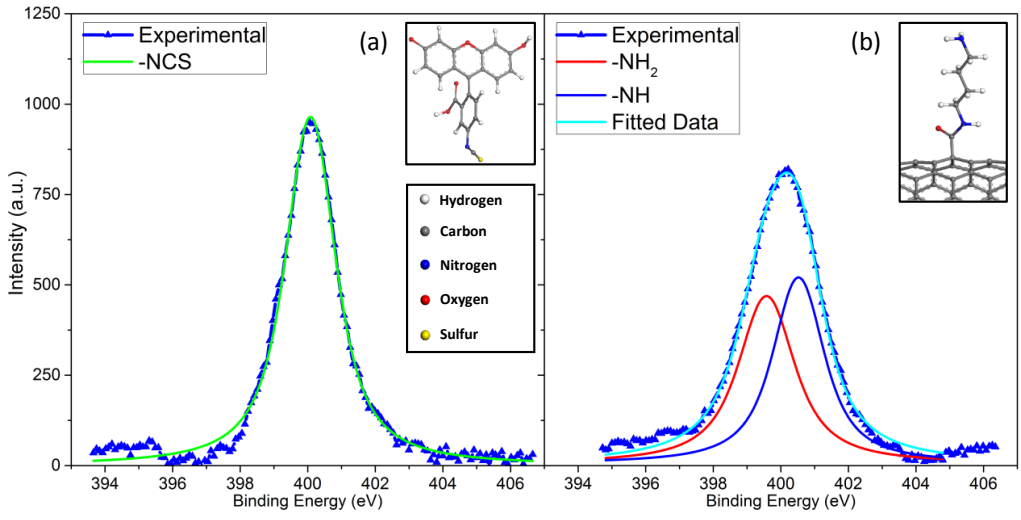

FIGURE 3.1: *Experimental results of XPS measurements in the N1s orbital of (a) the FITC and (b) the DWNT-diamine, and respective results of the fitting.*

The $-NCS$ group contribution to the N1s peak can be defined by its characteristic position and wL, while its area is characteristic of the number of Nitrogen atoms involved in such groups. The fitting parameters are listed in table 3.1.

Chemical group	$-NCS$
Peak Position (eV)	400.1 ± 0.0
wL	1.4 ± 0.0
Area	2493.69 ± 0.07

TABLE 3.1: Fitting parameters of the $-NCS$ groups XPS peak from the FITC sample.

DWNT-Diamine

The DWNT-diamine sample has in principle two types of Nitrogen atoms: the first type is involved in a $-NH$ group and participates to the chemical bond that links the linker to the nanotube. The second type, located at the other extremity of the linker, is involved in a $-NH_2$ group (see inset of Fig. 3.1-b). For the fitting procedure, the peaks positions and the wL were let unconstrained, and the area of the two peaks were constrained to be equal.
Figure 3.1-b shows the result of the XPS measurement of the DWNT-diamine in the N1s orbital binding energy region (blue marked line) and displays the results of the peak fit of the two chemical groups contributions to the spectrum: $-NH_2$ groups (red line) and $-NH$ groups (blue line)[196].

Now that the $-NH_2$ and the $-NH$ contributions to the N1s peak have been fitted, we can define the position and the wL that are characteristic of the latter groups signal. The fitting parameters are listed in table 3.2.

Chemical group	$-NH_2$	$-NH$
Peak Position (eV)	399.6 ± 0.0	400.6 ± 0.0
wL	1.68 ± 0.06	1.45 ± 0.04
Area	1370.67 ± 25.05	1370.67 ± 25.05

TABLE 3.2: Fitting parameters of the $-NH_2$ and $-NH$ contribution to the N1s peak from the DWNT-Diamine sample.

DWNT-diamine-FITC

This sample is more complex than the previous ones in terms of species and chemical groups. It is necessary to define the different species that are present in the sample and which contribute to the XPS N1s peak in order to be able to fit correctly the data. For this sample we developed three models (see figure 3.2) corresponding to the three different configurations which could occur at the surface of the DWNTs:

1. The diamine did not react with the FITC and remained unchanged. (Model I)

2. The diamine and the FITC did react together and are covalently bonded. (Model II)

3. The FITC did not react with a linker, remained unchanged and has been adsorbed at the surface of the DWNTs. (Model III)

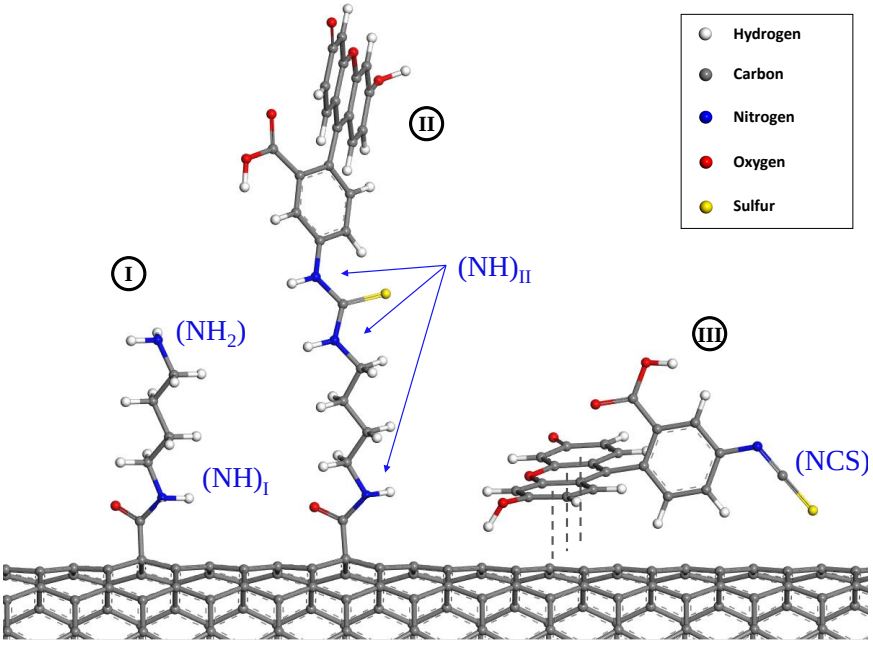

FIGURE 3.2: *Illustration of the three models chosen for representing the surface of the DWNT-diamine-FITC sample : (I) SWNT-linker, (II) SWNT-linker-FITC and (III) SWNT@Fluo.*

The DWNT-Diamine-FITC sample contains three different types of Nitrogen atoms. The first type is involved in $-\mathbf{NH_2}$ groups and is provided by the diamine that stands in the Model I (diamine-I). The second type of Nitrogen is involved in $-\mathbf{NCS}$ chemical groups, they are provided by the FITC-III belonging to the Model III presented above. The FITC-III is stacked at the surface of the CNTs and was not able to react with a diamine. Therefore, its $-\mathbf{NCS}$ group remained unchanged. Finally, the last type of Nitrogen atom is involved in $-\mathbf{NH}$ groups. They are shared between the diamine-I that did not react with any FITC (Model I) and the diamine-II that did react (Model II). Concerning the diamine-II, that reacted with the FITC-II, it still owns one of this chemical group involved in the covalent bond with the Nanotube, but exhibits two additional $-\mathbf{NH}$ groups as the result of the chemical reaction between the original $-\mathbf{NH_2}$ and $-\mathbf{NCS}$ groups respectively.

Figure 3.3 shows the result of the XPS measurement of the DWNT-Diamine-FITC in the N1s orbital binding energy region (blue marked line). The peak

positions and the wL obtained with the FITC sample ($-\mathbf{NCS}$) and the DWNT-diamine sample ($-\mathbf{NH_2}$ and $-\mathbf{NH}$) were used directly as fitting parameters, while the areas were let unconstrained. The results of the fit are displayed on Figure 3.3 for each group contributing to the N1s XPS peak : $-\mathbf{NH_2}$ (red line), $-\mathbf{NCS}$ (green line) and $-\mathbf{NH}$ (blue line).

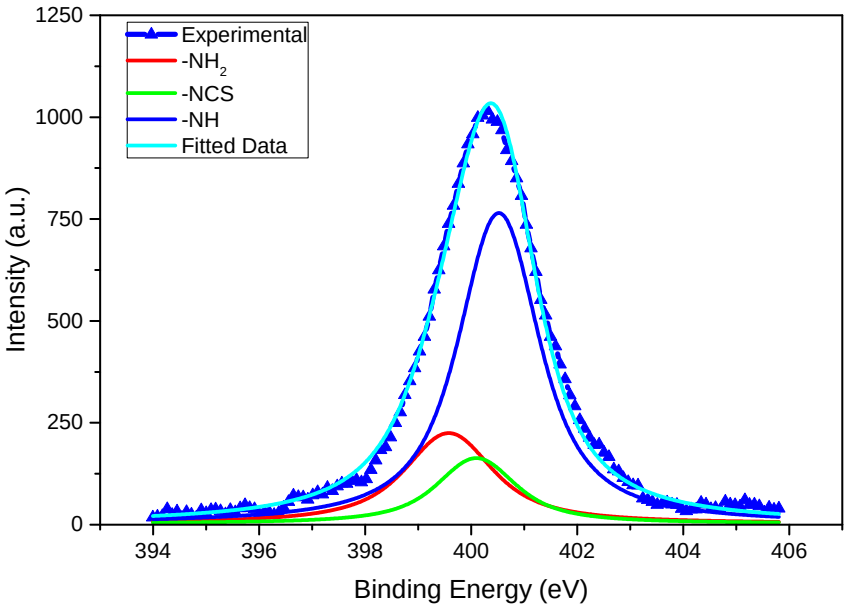

FIGURE 3.3: *Experimental results of XPS measurement of the DWNT-diamine-FITC in the N1s orbital binding energy region, and results of the fitting using the reference samples.*

From the fitted curves of the different group contributions to the N1s peak, we can obtain their respective positions, areas and wL. The fitting parameters are listed in table 3.3.

Chemical group	$-NH_2$	$-NCS$	$-NH$
Peak Position (eV)	399.6 ± 0.0	400.1 ± 0.0	400.6 ± 0.0
wL	1.68 ± 0.00	1.40 ± 0.00	1.45 ± 0.00
Area	655.18 ± 44.96	415.92 ± 77.67	2023.32 ± 49.25

TABLE 3.3: Characteristics of the different contributions to the N1s peak from the DWNT-diamine-FITC sample.

DWNT@FITC

The only molecule containing nitrogen atoms is the DWNT@FITC sample is the FITC itself. Its unique nitrogen atom involved in a $-\mathrm{NCS}$ chemical group. As for the FITC sample, the peak position, the area and the wL were let unconstrained during the fitting procedure.

Figure 3.4 shows the result of the XPS measurement of the DWNT@FITC in the N1s orbital binding energy region (blue marked line) and displays the result of the peak fitting (green line).

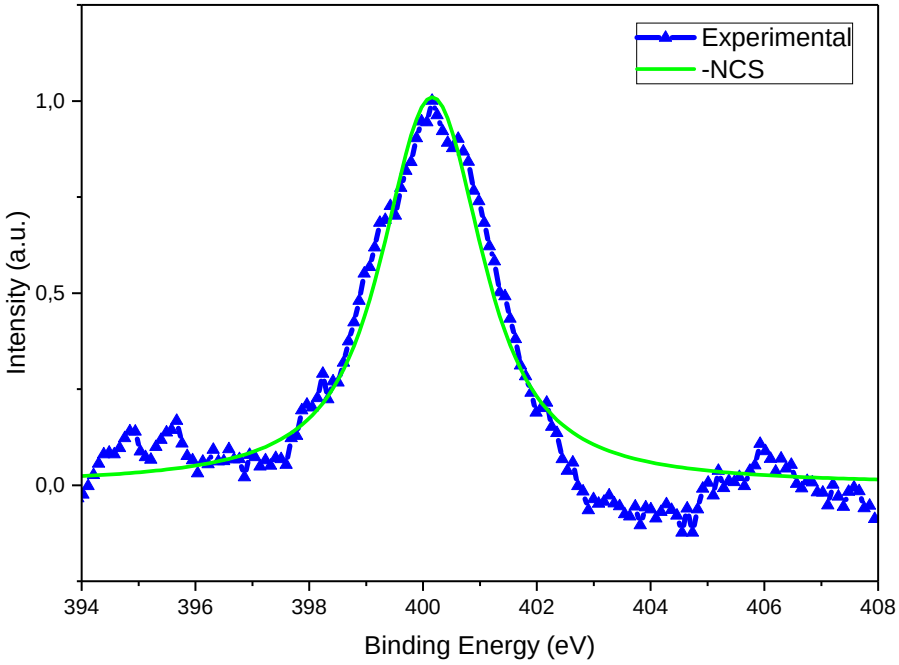

FIGURE 3.4: *Experimental results of XPS measurement of the DWNT@FITC in the N1s orbital binding energy region, and results of the fitting. The spectrum is normalized to unity.*

The fitting parameters are listed in table 3.4.

Chemical group	$-NCS$
Peak Position (eV)	400.1 ± 0.0
wL	1.79 ± 0.0
Area	3.18 ± 0.08

TABLE 3.4: Fitting parameters of the $-NCS$ groups XPS peak from the SWNT@FITC sample.

We see on figure 3.4 that the spectrum obtain in this N1s orbital region is rather noisy. The background noise is rather large and influence the shape of the measure spectra. This comes from the fact we have a very poor statistic on this sample measurement, despite an overnight accumulation where the others were measured in few hours. It indicates us that the sample contains a very low amount of nitrogen, and consequently, that the quantity of FITC remaining adsorbed at the surface of the tubes after the washing procedure is very low. (Note that more evidences of the presence of FITC in this sample is presented in the Appendix A).

Process efficiency quantification from the DWNT-diamine-FITC sample

We need to define the relations between the XPS peaks area (that corresponds to chemical groups) and the number of molecules in a given Model out of the 3 mentioned above, knowing that the relative proportion of each group in terms of quantities is proportional to its relative proportion of the XPS peak area. Since only the diamine-I contains $-NH_2$ groups, and there is only one $-NH_2$ group and only one $-NH$ group per diamine-I when grafted on a DWNT (see Figure 3.2), we can then define n(diamine-I) $= n(NH)_I = n(NH_2)_{Tot} \propto A(NH)_I = A(NH_2)_{Tot}$. The amount of diamine-I is now accessible knowing the amount of $-NH_2$ groups. It is then necessary to define the amount of diamine-II in the sample. Concerning the Model II we find that for 1 mole of diamine-II there are 3 moles of $-NH$ groups (Fig. 3.2). We can

thus define n(diamine-II) $\propto \frac{A(\mathrm{NH})_{Tot} - A(\mathrm{NH_2})_{Tot}}{3}$. Finally, we need to define the amount of FITC which did not react with the diamine and, therefore, which is π-stacked onto the DWNTs. As this FITC remained unchanged during the functionalization process, all the nitrogen atoms have the same signature as the FITC sample, corresponding to $-\mathrm{NCS}$ groups. As FITC owns one group per molecule it is then easy to define n(FITC-III) $= n(\mathrm{NCS})_{Tot} \propto A(\mathrm{NCS})_{Tot}$. Finally, using the different areas obtained with the fitting of the DWNT-diamine-FITC sample spectra (see Table 3.3) the relative proportions of the three models present in the sample were determined and are presented in table 3.5 hereafter.

	Model I	Model II	Model III
Relative proportions	0.43 ± 0.03	0.30 ± 0.02	0.27 ± 0.04

TABLE 3.5: Relative proportions of the three models constituting the DWNT-diamine-FITC sample given by the XPS measurements.

In order to determine the process efficiency we need to define relevant quantities to compare. Here we introduce three different ratios in order to have the clearest vision of what our sample looks like in terms of covalent and non-covalent grafting :

The covalent coverage ratio It represents the amount of diamine which reacted with the FITC comparatively to the total amount of Diamine on the sample before the grafting of the FITC. In that sense it can be interpreted as a measure of the efficiency of the covalent grafting of the fluorophore. It is defined as the ratio between the number of moles of the diamine that reacted

with the FITC and the total number of moles of diamine in the sample :

$$R_{cc} = \frac{n(\text{diamine-II})}{n(\text{diamine-I}) + n(\text{diamine-II})} \propto \frac{A(\text{NH})_{\text{Tot}} - \text{A}(\text{NH}_2)_{\text{Tot}}}{A(\text{NH})_{\text{Tot}} + 2 \times \text{A}(\text{NH}_2)_{\text{Tot}}} \tag{3.1}$$

The non-covalent grafting ratio It represents the amount of FITC which is adsorbed onto the carbon nanotubes comparatively to the total amount of FITC in the sample. It gives a measure of the proportion of fluorophore which did not react during the process but which is still present in the sample. It is defined as the ratio between the number of moles of FITC that did not react and the total number of moles of FITC in the sample :

$$R_{ncg} = \frac{n(\text{FITC-III})}{n(\text{FITC-II}) + n(\text{FITC-III})} \propto \frac{3 \times A(\text{NCS})_{\text{Tot}}}{3 \times A(\text{NCS})_{\text{Tot}} + \text{A}(\text{NH})_{\text{Tot}} - \text{A}(\text{NH}_2)_{\text{Tot}}} \tag{3.2}$$

The covalent grafting ratio It represents the amount of FITC which is covalently grafted onto the carbon nanotubes comparatively to the total amount of FITC in the sample. It gives a measure of the proportion of fluorophore which did react with the diamine during the process. It is defined as the ratio between the number of moles of FITC that did react and the total number of moles of FITC in the sample, meaning it is simply the inverse ratio of the non-covalent grafting ratio :

$$R_{cg} = 1 - R_{ncg} = \frac{A(\text{NH})_{\text{Tot}} - A(\text{NH}_2)_{\text{Tot}}}{3 \times A(\text{NCS})_{\text{Tot}} + \text{A}(\text{NH})_{\text{Tot}} - \text{A}(\text{NH}_2)_{\text{Tot}}} \tag{3.3}$$

Now the relation between the amount of the different organic molecules in the sample and the chemical groups contributing to the XPS N1s orbital peaks area have been defined, and relevant ratios to understand our sample have been established, we can calculate them in order to get an estimation of the functionalization process efficiency. Using Eq. 3.1, 3.2 and 3.3, and using the XPS peaks area summed up in table 3.3 we find that $R_{cc} = 0.41 \pm 0.02$,

$R_{ncg} = 0.47 \pm 0.05$ and $R_{cg} = 0.53 \pm 0.05$.

The R_{cc} indicates that 41% only of the diamine available reacted with the FITC to form a covalent bond (see figure 3.5) , which question the efficiency of the grafting process and leaves a lot of room for improvement. Then, the comparison of the R_{ncg} and the R_{cg} seems to show that about 50% of the total amount of FITC is involved in covalent interaction with the DWNTs while the other half of is simply adsorbed at the surface (see figure 3.6). These latter results are very concerning since they indicates that potentially half of the fluorescence could be attributed to relatively weakly bonded fluorophores molecules. Finally, it is important to notice that the results obtained with the DWNT@FITC sample (figure 3.4) indicates that the quantity of FITC adsorbed at the surface of the DWNTs is very low in the absence of the linker, and that the washing procedure was quite efficient in this case. This led us to believe that the presence of the 1,4-diaminobutane could have a strong influence on the final proportion of FITC simply adsorbed on the nanotubes.

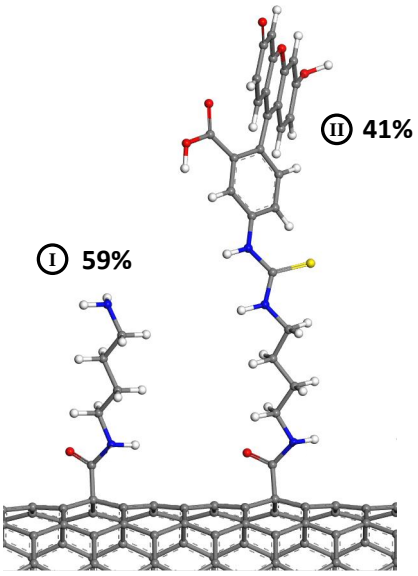

FIGURE 3.5: *Representation of the results given by the R_{cc} for the DWNT-diamine-FITC surface.*

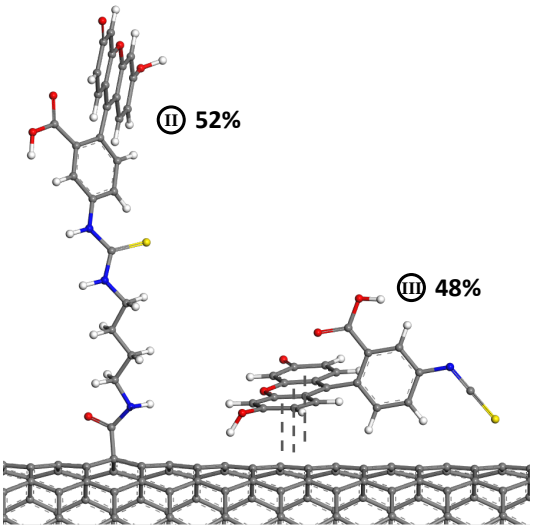

FIGURE 3.6: *Representation of the results given by the R_{ncg} and the R_{cg} for the DWNT-diamine-FITC surface.*

3.1.2 Inelastic Neutron Scattering and DFT

All the samples were heated up to 380K under vacuum (10^{-6} bar) in order to remove the water trapped within the DWNTs samples and sealed inside standard aluminium cylindrical containers with an indium O-ring. The INS measurement were then performed on the samples cooled down to 5K.

The simulations were performed using the software Materials Studio[197]. The calculations of the normal modes associated to our samples were performed considering three model systems. For each models the DWNT have been replaced by a periodic single-walled carbon nanotube (SWNT) (6,6) of 8.14 Å diameter placed in a triclinic lattice, in order to decrease the number of atoms and optimize the computational time. The SWNT was oriented parallel to the $\vec{c}$ vector of the lattice and the lattices parameters were chosen as following : a = 15.000-20.000 Å, b = 20.000 Å, c = 14.595 Å ; α = 90°, β = 90°, γ = 120°. Three models have been chosen to represent the three extreme cases that can be found at the end of the grafting process. The first model is a SWNT with one molecule of linker covalently bonded to it, representing the case of 0% of FITC grafted, in the following will be referred as "SWNT-linker" (see figure 3.7-a). The second model is a SWNT that corresponds to the "SWNT-linker" model but where, in addition, one molecule of FITC is covalently bonded to the linker, and represents the case of 100% of fluorophore covalently grafted. It will be referred as "SWNT-linker-Fluo" (see figure 3.7-b). For each of these two models, a search of the lowest energy space conformation was performed using the module "Conformers" in Materials Studio. The rotatable torsion angles of the nitrogen bonds in our models were let free and a systematic search was performed by rotating step by step each of them. The other degrees of freedom (carbon bonds of the organic molecules) were kept constrained since the more stable space conformations of polyamines were found for linear carbon chains [198–200]. At each step a coarse geometry optimization was performed and the total energy of the system was calculated. Then, the lowest energy space conformation was kept for the density functional theory (DFT) calculations. Finally, the third model is constituted of one SWNT and one FITC weakly bonded through adsorption interactions, representing the case were 100% of the FITC is non-covalently

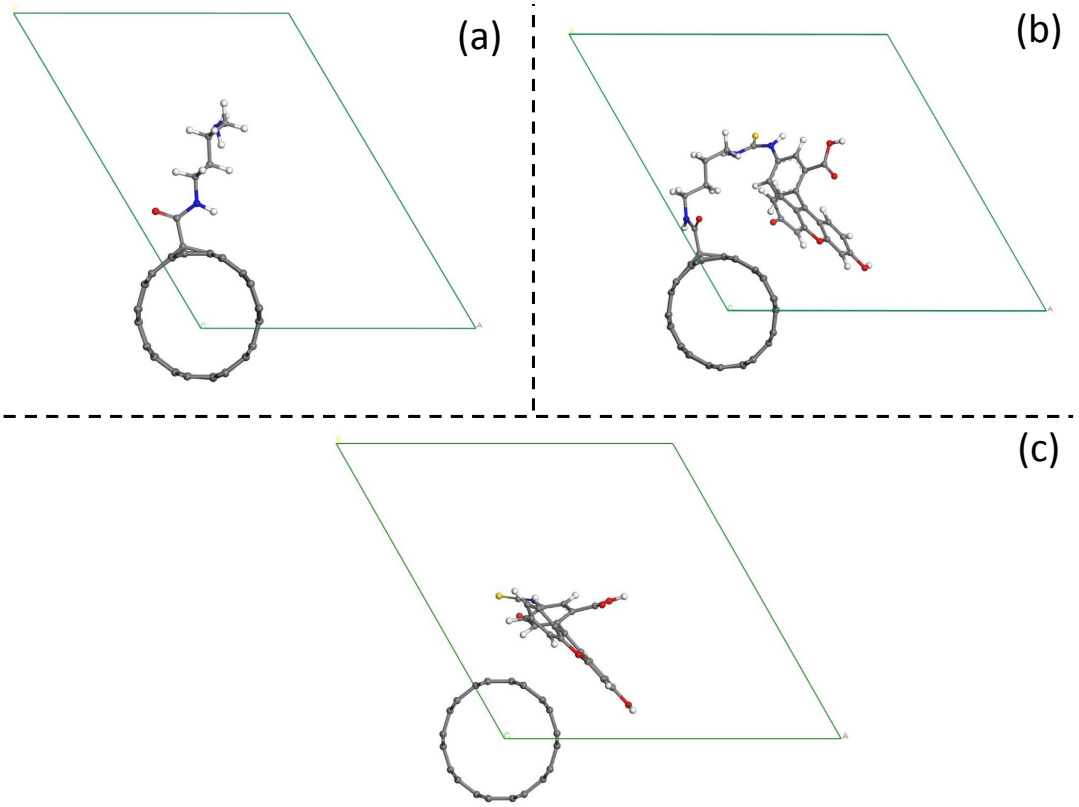

FIGURE 3.7: *Representation of the three model systems and their respective lattices, chosen for the DFT calculations. With (a) the SWNT-linker, (b) the SWNT-linker-Fluo and (c) the SWNT@Fluo.*

grafted. It will be referred as "SWNT@Fluo" from now on (see figure 3.7-c). The DFT calculations were performed using the DMol3 module of Materials Studio with the GGA-PBE functional[187] in order to achieve the fine geometry optimization of the systems after which the residual forces were converged close to zero ($\sim 10^{-3}$). To do so, we used an all electron core treatment and a double numerical plus polarization basis set, with a 10^{-5} energy cutoff, a 10^{-6} SCF tolerance and a gamma k-point sampling. Finally, once an equilibrium structures was reached, lattice dynamics calculations were subsequently performed to obtain the phonon frequencies by diagonalization of the dynamical matrix.

The $\mathrm{g}(\omega)$ is the sum of the individual atomic contribution to the vibrational density of states and is defined by $\mathrm{g}(\omega) = \sum_i \mathrm{g_i}(\omega)$. In order to compare with the $\mathrm{GDOS_{exp}}$ it was necessary to calculate a theoretical generalized

density of states ($\mathrm{GDOS_{th}}$) taking into account the individual atomic contributions weighted by their respective neutron cross section and mass, and defined by $\mathrm{GDOS_{th}} \propto \sum_i \frac{\sigma_i}{m_i} g_i(\omega) e^{-2W_i(Q)}$, where σ_i indicate the experimental individual cross section, m_i is the mass and $W_i(Q)$ is the Debye-Waller factor for the atom i. Since the hydrogen cross section is very large compared to the other atoms of our models, the individual contributions of any atoms are negligible compared to those of hydrogen in the case of INS measurements, and the $\mathrm{GDOS_{th}}$ can be then approximated such as $\mathrm{GDOS_{th}} \approx g_H(\omega) e^{-2W_H(Q)}$, where $g_H(\omega)$ is the hydrogen partial density of states. Finally, in order to reproduce at best the $\mathrm{GDOS_{exp}}$ measured in INS experiment the multiphonon events ($M(\omega)$) were taken into account (please refer to Appendix B for more details on multiphonon events). Indeed, as IN1-LAGRANGE is an indirect geometry spectrometer the momentum transfer (Q) increases with the energy transfer [171], and as the $M(\omega)$ are Q-dependent [201, 202], they play an important role in the shape of the measured spectra. The $\mathrm{GDOS_{th}}$ is thus defined by $\mathrm{GDOS_{th}} \approx g_H(\omega) e^{-2W_H(Q)} + M(\omega)$.

DFT calculations results

The DFT calculations performed on the three model systems SWNT-linker, SWNT-linker-Fluo and SWNT@Fluo, which represent three limit cases of the grafting process, allow us to understand the changes expected in our experimental data in terms of active vibrational modes. Indeed, figure 3.8 compares the hydrogen partial density of states ($g_H(\omega)$) obtained via DFT calculations for (a) the SWNT-linker, (b) the SWNT-linker-Fluo and (c) the SWNT@Fluo. We were then able to identify characteristic vibrational bands of our model molecules (see table 3.6). For instance, in the bending region, the SWNT-linker and the SWNT-linker-Fluo $g_H(\omega)$ present obvious similarities notably the two broad set of modes at 1270-1380 and 1440-1480 $\mathrm{cm^{-1}}$ corresponding

to the bending vibrational modes of the -CH groups with no particular distinction between the -CH sp^3 (Linker) and the -CH sp^2 (FITC). Similar modes were found at 1140-1220 cm^{-1} for the three models, corresponding to -CH bending modes, and, once again, without distinction between the models despite the apparent change in intensity and position. Nevertheless, a major difference is clearly visible between the systems, at 1620 cm^{-1} on figure 3.8-a and disappears completely on figure 3.8-b. This characteristic vibration corresponds to the bending mode of the -NH_2 groups and present the advantage to be isolated from the other modes and to be clearly identifiable. It was naturally chosen as the signature of the disappearance of the -NH_2 groups characteristic of the covalent grafting of the FITC. On the other hand, in the stretching region, signatures of the -CH sp^3 were found on the SWNT-linker and the SWNT-linker-Fluo models between 2890 and 3090 cm^{-1}, and are characteristic vibrational modes of -CH belonging to the linker. On figures 3.8-b and 3.8-c, the presence of the FITC brought new vibrational modes arising at 3100-3160 cm^{-1} which are characteristic of the -CH sp^2 constituting the fluorescent molecule. Finally, the vibrational modes of the -NH and -NH_2 and some -OH groups are located within 3420-3510 cm^{-1}. Unfortunately the vibrational bands are very close to each other, so that we do not expect to see any difference on the $GDOS_{exp}$ in the stretching region if the amount of -NH_2 groups decreases after the grafting process.

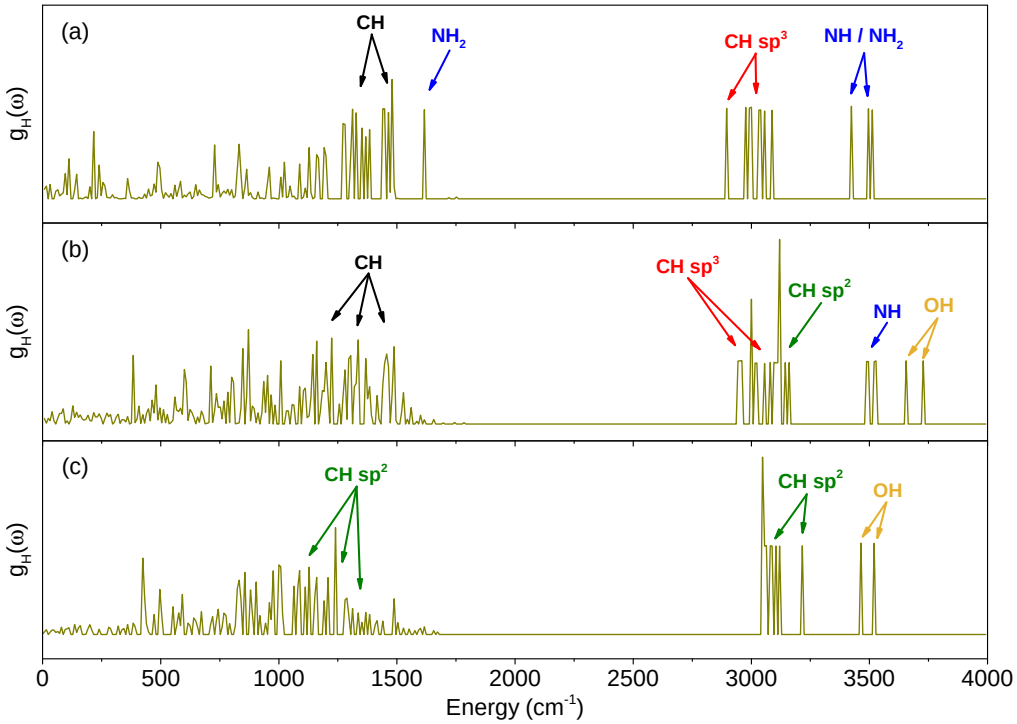

FIGURE 3.8: *Comparison of the* $g_H(\omega)$ *obtained via DFT calculations for the three models : (a) the SWNT-linker, (b) the SWNT-linker-Fluo and (c) the SWNT@Fluo.*

Modes (cm^{-1})	SWNT-linker	SWNT-linker-Fluo	SWNT@Fluo
740-1080	Bending -CH (out of plane)	Bending -CH (out of plane)	Bending -CH (out of plane)
1230-1480	Bending -CH (in plane)	Bending -CH (in plane)	Bending -CH (in plane)
1600-1640	Bending $-NH_2$ (in plane)	-	-
2850-3250	Stretching -CH	Stretching -CH	Stretching -CH
3400-3550	Stretching -NH/$-NH_2$	Stretching -NH	Stretching -OH
3600-3750	-	Stretching -OH	-

TABLE 3.6: Vibrational modes of interest for the three model systems: SWNT-linker, SWNT-linker-Fluo and SWNT@Fluo.

INS evidences of the covalent grafting of the FITC

Aiming at finding the characteristic INS vibrational bands modified by the covalent grafting of the fluorophore onto the linker, three reference samples have been prepared and analyzed in INS spectroscopy (refer to chapter 2.1.4 and figure 2.10 for details about the samples):

1. The Diamine (commercial 1,4-diaminobutane).
2. The FITC (commercial fluorescein isothiocyanate).
3. The Diamine-FITC (product of the chemical reaction of the Diamine and the FITC, witnessing the covalent grafting).

Figure 3.9 shows the experimental results of the INS spectroscopy performed on the reference samples in the energy range comprised between 500 and 4000 cm^{-1}. First of all, by comparing the results for the Diamine-FITC sample (cyan line) and the FITC sample (green line), the presence of FITC after the grafting process was naturally associated to two sets of characteristic vibrational bands between 830-960 cm^{-1} and between 1100-1250 cm^{-1}. Nevertheless it could not be used to differentiate the FITC covalently bonded from the one simply adsorbed. Then, comparing the results obtained for the Diamine sample (pink line) and the Diamine-FITC sample, it was clearly visible that four isolated characteristic vibrational bands centered at 760, 910, 1050 and 1620 cm^{-1} completely disappeared once the Diamine reacted with the FITC and formed a covalent bond. These bands, strongly modified during reaction, were perfect candidates to evidence the covalent grafting of the fluorophore on the linker.

Finally, these results have been compared with the INS spectroscopy experimental results obtained for the DWNT-diamine and the DWNT-diamine-FITC samples displayed on figure 3.10. These two samples represent respectively the step before (blue line) and the step after the grafting process of the

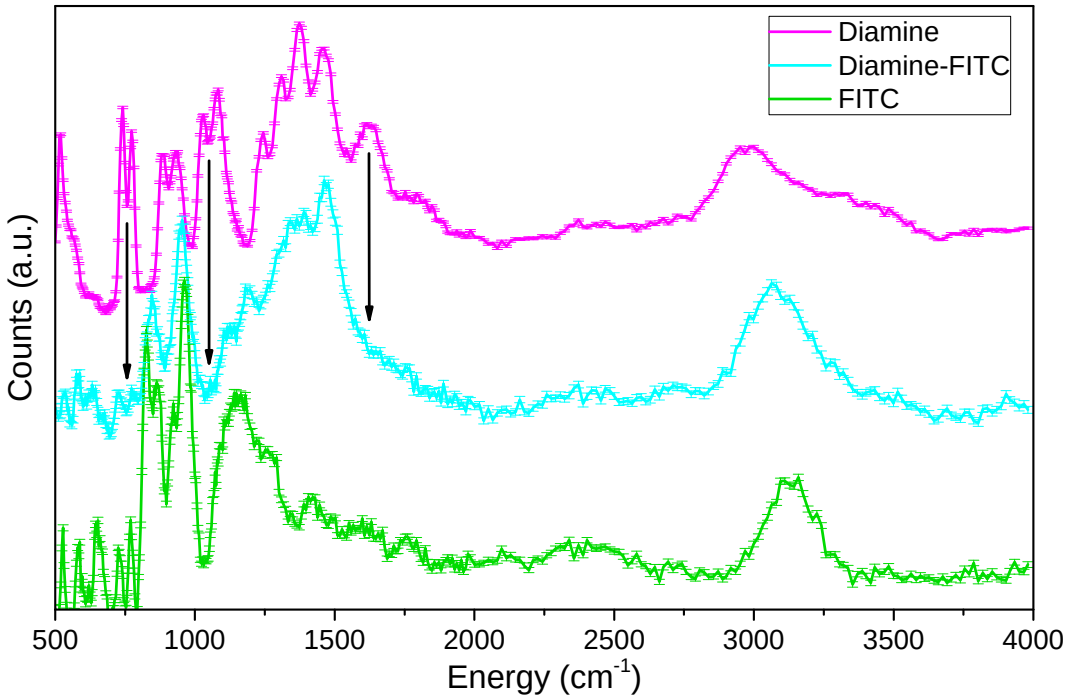

FIGURE 3.9: *Comparison of the experimental INS spectra obtained for the reference samples : Diamine (pink line), FITC (green line) and Diamine-FITC (cyan line).*

fluorophore (red line). By looking at the characteristic vibration bands identified above, it appeared that the slight growth of the bands located at 930 and 1200 cm^{-1} (green arrows) suggests the presence of FITC in the sample after the process, while the decrease of the bands at 740 and 1060 cm^{-1} (pink arrows) gave the confirmation that a significant amount of diamine reacted with the FITC to form covalent bonds.

Concerning the vibrational band at 1620 cm^{-1}, we see that there is no sign of any decrease before and after the grafting process. This can be attributed to the fact that the spectra are clearly distorted by multiphonon events and especially in the range from 1500-2000 cm^{-1} where we can easily identify the presence of phonon wings that could somehow hide the vibrational band of interest. In order to go further we thus need to take into account the effect of multiphonon events on our measured spectra.

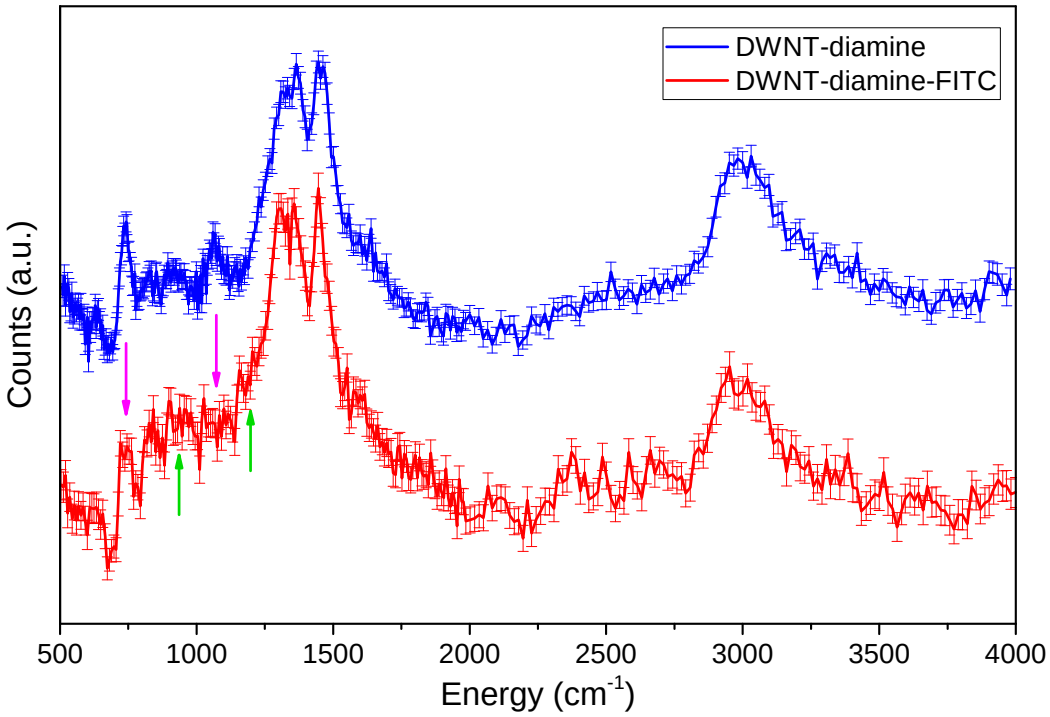

FIGURE 3.10: *Comparison of the experimental INS spectra obtained for the DWNT-diamine (blue line) and the DWNT-diamine-FITC (red line) samples.*

Quantification of the grafting efficiency

The measurements performed on IN1-LAGRANGE allowed us to obtain well defined spectra of the DWNT-diamine and the DWNT-diamine-FITC samples, and to have access to several vibrational modes. Figure B.6 shows the experimental generalized density of states ($\mathrm{GDOS_{exp}}$) measured in the energy range 500-4000 $\mathrm{cm^{-1}}$ for the DWNT-diamine (fig.B.6-a) and the DWNT-diamine-FITC (fig.B.6-b) samples (Red lines). Figure B.6 also shows the calculated $\mathrm{g_H}(\omega)$ of the SWNT-linker model (fig.B.6-a) and the mixing of the $\mathrm{g_H}(\omega)$ obtained for the SWNT-linker, the SWNT-linker-Fluo and the SWNT@Fluo models in the proportion of respectively 60%/20%/20% (fig.B.6-b), corresponding to the best fit to the $\mathrm{GDOS_{exp}}$ obtained. Both the $\mathrm{g_H}(\omega)$ and the mixed $\mathrm{g_H}(\omega)$ were convoluted with the experimental resolution (3% of the energy)(Cyan lines). It shows as well the corresponding calculated multiphonon contributions for these models (green line) and the

resulting theoretical generalized density of states ($\mathrm{GDOS_{th}}$) which corresponds to the sum of the $\mathrm{g_H}(\omega)$ and Multiphonon contributions, convoluted with the experimental resolution (blue line).

The simulations were based on perfect model systems where the SWNTs were well individualized and all oriented in the same direction. Therefore, the simulation results could not be expected to perfectly fit our data, as can be seen on figure B.6 in the 500-1200 $\mathrm{cm^{-1}}$ and 2750-4000 $\mathrm{cm^{-1}}$ regions. Indeed, as real samples are much more complex than models, it is not surprising that several vibrational modes could practically be strongly affected by the changes of environment, and appeared to be shifted, broadened or even less intense than the DFT-based predictions. Nevertheless, the simulations performed appeared to fit properly the region of interest comprised between 1200 and 2250 $\mathrm{cm^{-1}}$ allowing their use for a better understanding of the samples composition.

Despite the clear evidences of the covalent grafting of FITC found previously, the INS experimental spectra of our two samples are very similar and particularly around 1600 $\mathrm{cm^{-1}}$ where we expected to see the largest differences after the grafting process, accordingly to the results provided by the DFT calculations (fig. 3.8). Indeed, this vibrational band was supposed to be strongly affected by the number of -$\mathrm{NH_2}$ groups in our samples and should decrease significantly when the FITC reacts with the linker. But, taking into account the multiphonon contributions to the spectra in our simulations we were able to explain this lack of differences in the experimental spectra. Indeed, it is clearly visible on figure B.6-b that for a mixing ratio of 60%/20%/20% of our three models $\mathrm{g_H}(\omega)$, the decrease in intensity undergone by the 1600 $\mathrm{cm^{-1}}$ vibration was compensated by the resulting multiphonon intensity associated to the bending region (500-2000 $\mathrm{cm^{-1}}$) fundamental vibrations. By looking at

the resulting $\mathrm{GDOS_{th}}$, this vibrational band intensity then appears to be almost unchanged despite the fact that 25% of the linker reacted with the FITC. Various ratios for mixing our three models have been tried and the best fit with the experimental data corresponds to this 60%/20%/20% ratio. These results could indicate that the bulk of the DWNT-diamine-FITC sample is slightly different from its surface (see XPS measurements) which would not be surprising since the DWNTs have a strong tendency to form bundles and that the grafting efficiency could change between the outside and the inside of those bundles. However, some other ratios could still fit reasonably our INS spectrum. Nevertheless, we were able to define that if less than 40% of the SWNT-linker model was taken into account in the mixing ratio, the intensity loss of the 1600 $\mathrm{cm^{-1}}$ vibrational mode could not be compensated by the multiphonons and would have been clearly visible on the DWNT-linker-FITC spectra. Therefore, accordingly to the INS results, we were able to find that in the best covalent grafting case scenario the sample is constituted of 40% of Model I, 30% of Model II and 30% of Model III, which is comparable to the results obtained with the XPS measurements.

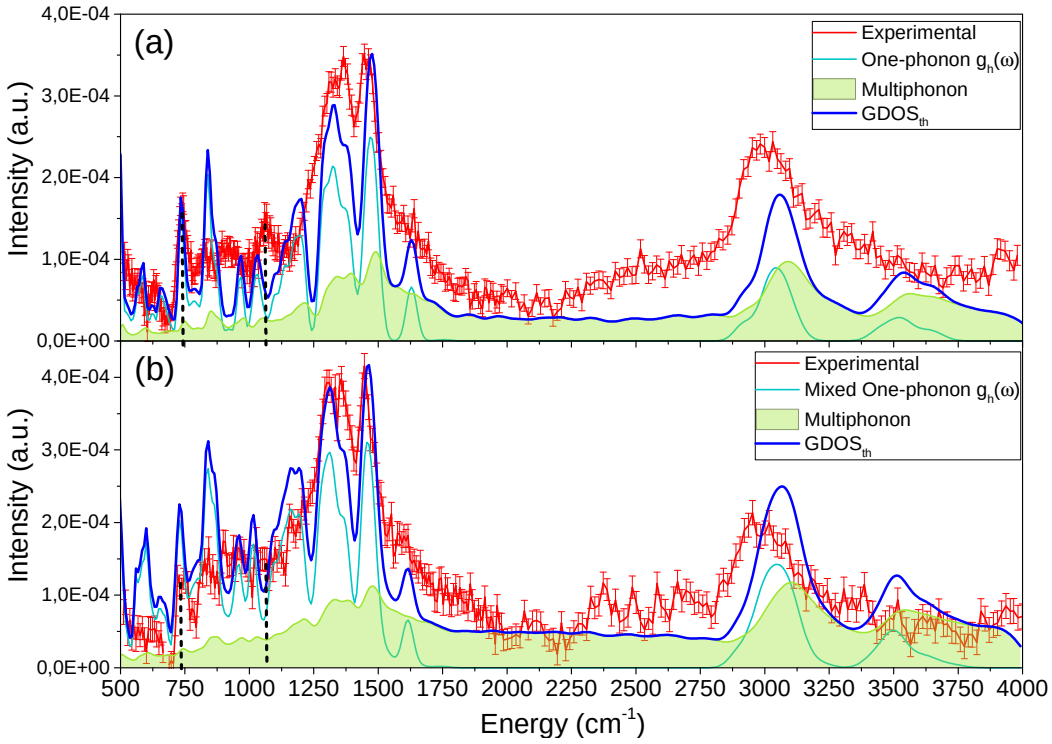

FIGURE 3.11: *Comparison of the* $\mathrm{GDOS_{th}}$ *(taking into account the multiphonon contribution) with the INS experimental spectra for (a) the DWNT-diamine and (b) the DWNT-diamine-FITC samples.*

The quantification of the covalent grafting efficiency of the FITC on DWNTs remains a central question for several toxicity studies. Based on spectroscopy techniques and calculations, it has been shown that not only the efficiency of the chemical reaction between the linker and the fluorophore stayed below 41%, although we used a grafting protocol very common in the literature, but also that there is a significant amount of fluorophore which remained adsorbed at the surface of the DWNTs after the grafting process. Indeed, the XPS measurements brought information on the surface of the sample and indicated that both covalent and non covalent grafting occurred during the grafting process. It also allowed to make an estimation of the relative proportions of each species at the surface of the sample, and provided concerning results with regards to the amount of FITC simply adsorbed onto the

DWNTs. Then, concerning the bulk of the sample, the INS measurement performed on IN1-LAGRANGE coupled with DFT Calculations showed strong evidences that the FITC reacted with the diamine. However, the results indicated that the proportions of FITC that reacted with the diamine could be even lower than for the surface but are not contradictory with the estimations provided by the XPS measurements. Finally, these results highlight that, although the amount of FITC markers grafted on carbon nanotubes when using a covalent strategy is always considered to be strongly bonded, a non-negligible part may indeed be only adsorbed even after thorough washing of the nanoparticles. This is likely to lead to a release of the fluorescent marker at some point along the journey of the nanoparticle throughout the cells or the whole organism, and thus to partially wrong conclusions in terms of their fate in terms of biodistribution, accumulation or excretion.

3.2 Study of the grafting of the Cyanine

In this part, the study of the streptocyanine grafting process efficiency will often be compared to the study of the FITC. The samples related to the cyanine were analyzed in the same conditions as the ones containing FITC for both the XPS and INS techniques. At this point, the reader is advised to refer to the chapters 2.1.3 and 2.1.4 in order to remind himself or herself of the differences between the Hemicarboxonium and the Cyanine as well as the composition of the different samples.

3.2.1 X-ray Photoelectron Spectroscopy

As it was performed with the FITC, the characterization of the surface of our samples and the determination of the different types of interaction between the Cyanine and the DWNTs were first needed. To do so two reference samples were used in order to identify the chemical groups involved.

The Cyanine sample was first analyzed, and then used, coupled with the XPS results obtained previously on the DWNT-diamine, to characterize our DWNT-diamine-Cyanine sample of interest.

Cyanine

A Cyanine molecule contains only one type of nitrogen involved in a $-\mathrm{N(Et)_2}$ chemical group (see inset of Fig. 3.12). Figure 3.12 shows the result of the XPS measurement of the Cyanine in the N1s orbital binding energy region (blue marked line) and displays the result of the peak fitting following the procedure mentioned above (Cyan line). Nevertheless, by looking at the experimental results shown on figure 3.12 it is clear that we needed two different contributions to fit properly our data. Again, the peak positions, the areas and the wL were let unconstrained during the fitting procedure.

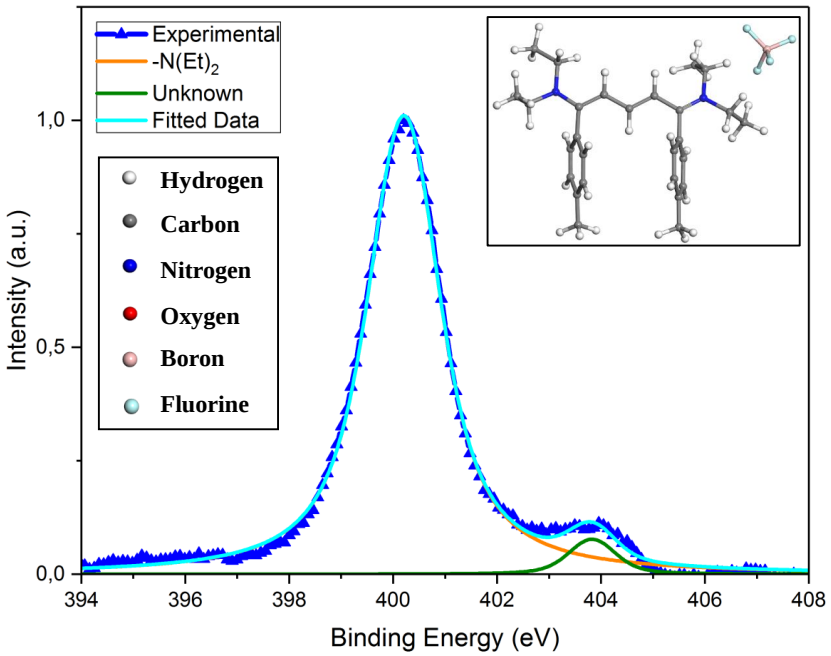

FIGURE 3.12: *Experimental results of XPS measurements in the N1s orbital of the Cyanine and results of the fitting. The spectrum is normalized to unity.*

The groups contribution to the N1s peak can be defined by their characteristic position and wL, and again, like for the FITC, their area is characteristic of the number of nitrogen atoms involved in such groups. The fitting parameters are listed in table 3.7.

Chemical group	$-\mathrm{N(Et)_2}$	unknown
Peak Position (eV)	400.2 ± 0.0	403.8 ± 0.0
wL	1.29 ± 0.02	0.46 ± 0.16
Area	2.45 ± 0.02	0.10 ± 0.01

TABLE 3.7: Fitting parameters of the $-\mathrm{N(Et)_2}$ groups XPS peak from the Cyanine sample.

The contribution located at 400.2 eV was then naturally attributed to the $-\mathrm{N(Et)_2}$ groups, since the cyanine is supposed to contain only one type of nitrogen atoms. Concerning the unknown contribution to the N1s orbital peak, the only example in literature that could satisfy both the binding energy at 403.8 eV and the species present in our sample is found for a nitrogen complex containing also a $\mathrm{BF_4^-}$ ion, the $[\mathrm{C_6H_5(N_2)}]\mathrm{BF_4}]$, studied by P. Finn and W.L. Jolly in 1972[203]. It has been attributed to the presence of a +1 charge of the diazonium ion. Nevertheless, even if the Cyanine presents certain similarities with this compound (6-carbon ring, nitrogen atoms, etc.), it is also very different (no diazonium, no direct attachement to a phenyl group, presence of a conjugated carbon chain, etc...). We must then be very careful with the conclusion related to the nature of this contribution. Moreover, comparatively to the main peak attributed to the $-\mathrm{N(Et)_2}$ groups, its peak area is 24 times smaller and does not appear on the following XPS results perfomed on the Cyanine containing samples. We thus chose to consider it negligible and to let it labelled "unknown".

DWNT-diamine-Cyanine

As for the DWNT-diamine-FITC sample, the analysis of the results concerning this sample, that underwent the functionalization process, is more complex than the references in terms of species and chemical groups. It is again necessary to define the different species that are present in the sample and which contribute to the XPS N1s peak in order to be able to fit correctly the data. Three models have been chosen to represent the surface of the sample (see figure 3.13) corresponding to the three different configurations which could occur at the surface of the DWNTs (see chapter 2.1.3 for details on the sample):

1. The diamine did not react with the Hemicarboxonium and remained unchanged. (Model I)

2. The diamine and the Hemicarboxonium did react together, are covalently bonded and turned the Hemicarboxonium into a fluorescent Cyanine. (Model II)

3. The Hemicarboxonium did not react with a linker, remained unchanged and has been adsorbed at the surface of the DWNTs. (Model III)

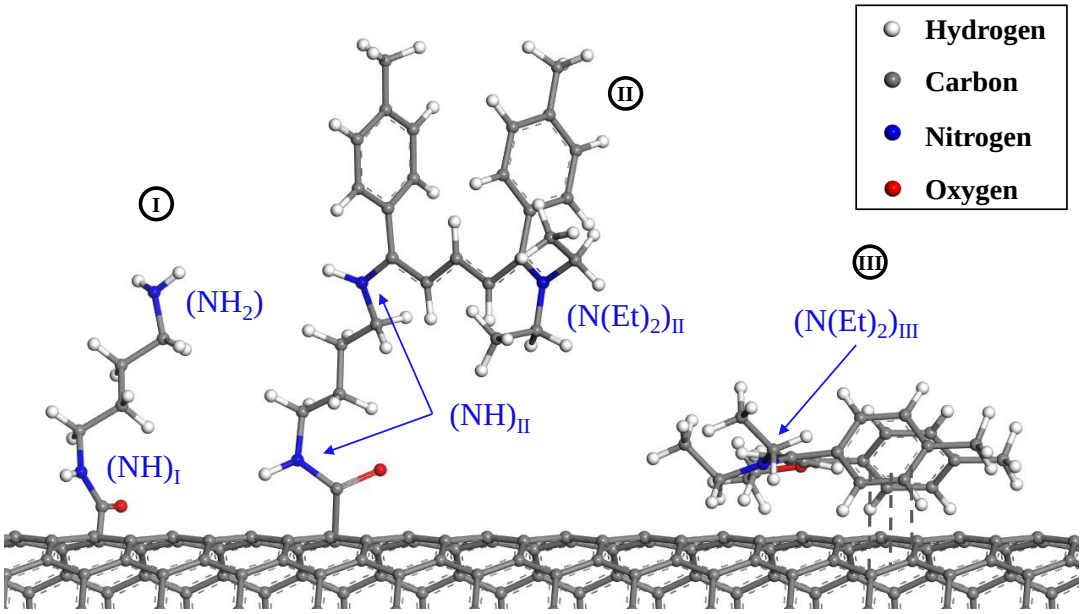

FIGURE 3.13: *Illustration of the three models chosen for representing the surface of the DWNT-diamine-Cyanine sample : (I) SWNT-linker, (II) SWNT-linker-Cyanine and (III) SWNT@Fluo.*

The DWNT-diamine-Cyanine sample contains three different types of nitrogen atoms. As for the DWNT-diamine-FITC the first type is involved in $-\mathbf{NH_2}$ groups and is provided by the diamine that stands in the Model I (diamine-I). The second type of nitrogen atom is involved in $-\mathbf{NH}$ chemical groups, are shared between the diamine-I that did not react with any Hemicarboxonium (Model I) and the diamine-II that did react (Model II). The main difference with the DWNT-diamine-FITC sample comes from the third type of nitrogen atoms. Indeed, this third type is involved in $-\mathbf{N(Et)_2}$ groups and is shared between the Hemicarboxonium that did react with a diamine (Model II) and turned into a fluorescent Cyanine (referred as "Cyanine-II" from now on), and the Hemicarboxonium which is adsorbed at the surface of the DWNTs and that did not react with a diamine (Model III) (see fig. 3.13). This latter Hemicarboxonium will be referred as "Hemi-III" from now on.

Figure 3.14 shows the result of the XPS measurement of the DWNT-diamine-Cyanine in the N1s orbital binding energy region (blue marked line). The peak positions and the wL obtained with the Cyanine sample

($-\mathbf{N(Et)_2}$ in table 3.7) and the DWNT-diamine sample ($-\mathbf{NH_2}$ and $-\mathbf{NH}$ from table 3.2) were used directly as fixed fitting parameters, while the areas were let unconstrained. The results of the fit are displayed on Figure 3.14 for each group contributing to the N1s XPS peak : $-\mathbf{NH_2}$ (red line), $-\mathbf{N(Et)_2}$ (orange line) and $-\mathbf{NH}$ (blue line).

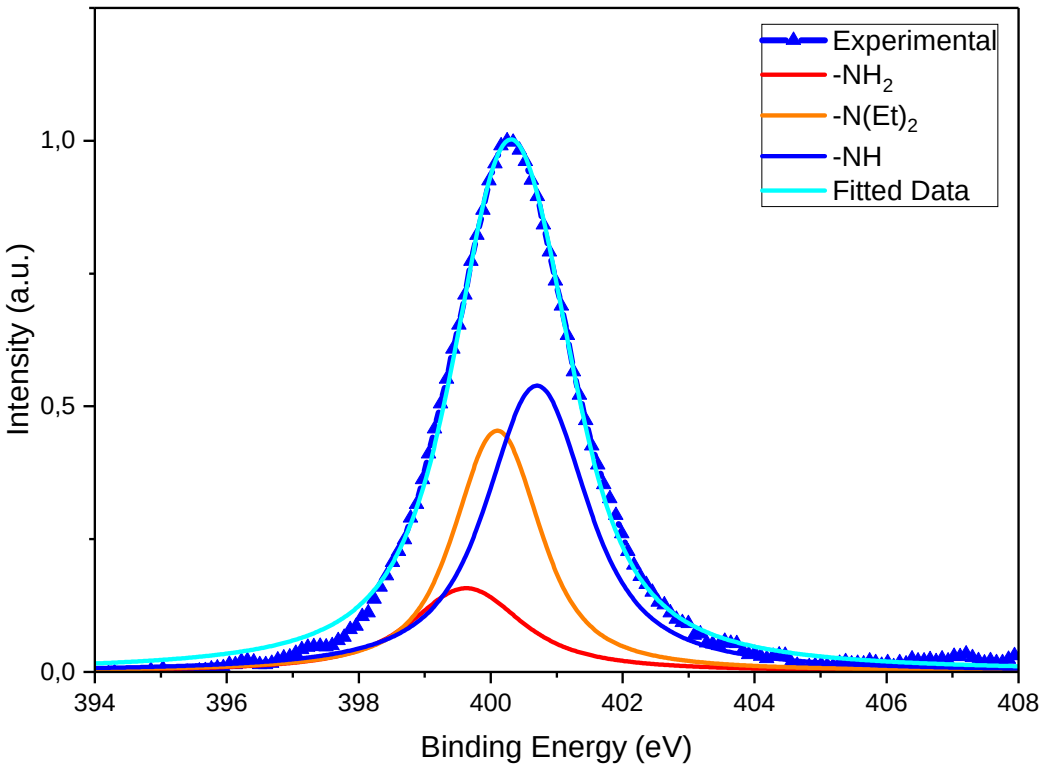

FIGURE 3.14: *Experimental results of XPS measurement of the DWNT-diamine-FITC in the N1s orbital binding energy region, and results of the fitting using the reference samples. The spectrum is normalized to unity.*

From the fitted curves of the different group contributions to the N1s peak, we can obtain their respective positions, areas and wL. The fitting parameters are listed in table 3.8.

Chemical group	$-NH_2$	$-N(Et)_2$	$-NH$
Peak Position (eV)	399.6 ± 0.0	400.2 ± 0.0	400.6 ± 0.0
wL	1.68 ± 0.00	1.29 ± 0.00	1.45 ± 0.00
Area	0.47 ± 0.03	0.99 ± 0.04	1.43 ± 0.02

TABLE 3.8: Characteristics of the different contributions to the N1s peak from the DWNT-diamine-Cyanine sample.

DWNT@Cyanine

The DWNT@Cyanine sample is supposed to contain Cyanine molecules adsorbed at the surface of the DWNTs. Therefore it would contains only one type of Nitrogen involved in a $-N(Et)_2$ chemical group. Again, the peak positions, the areas and the wL were let unconstrained during the fitting procedure.

Figure 3.15 shows the result of the XPS measurement of the DWNT@Cyanine in the N1s orbital binding energy region (blue marked line) and displays the result of the peak fitting (orange line).

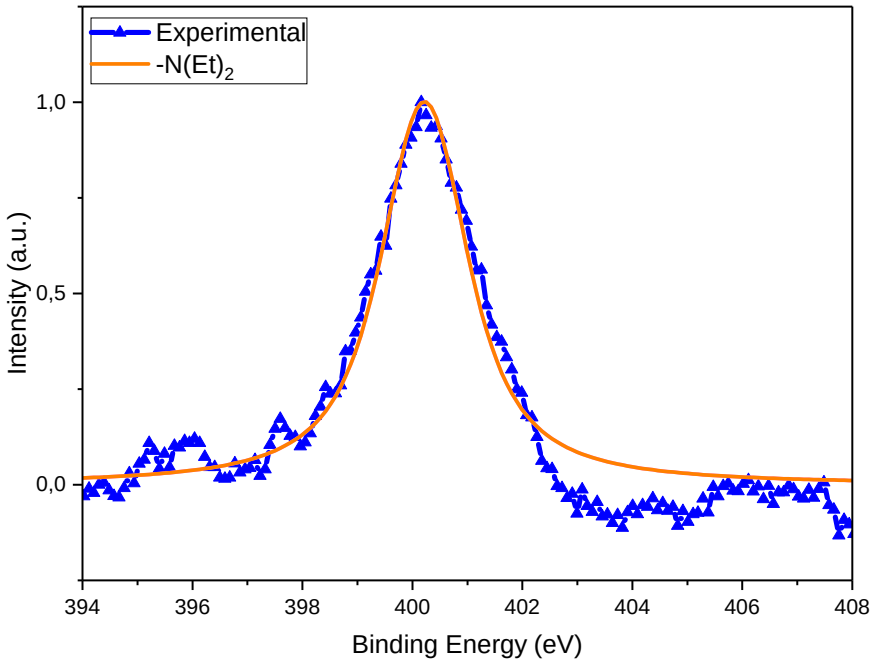

FIGURE 3.15: *Experimental results of XPS measurement of the DWNT@Cyanine in the N1s orbital binding energy region, and results of the fitting. The spectrum is normalized to unity.*

The fitting parameters are listed in table 3.9.

Chemical group	$-\mathrm{N(Et)_2}$
Peak Position (eV)	400.2 ± 0.0
wL	1.54 ± 0.06
Area	2.79 ± 0.07

TABLE 3.9: Fitting parameters of the $-$NCS groups XPS peak from the FITC sample.

Again, the figure 3.15 shows that the spectrum obtained is rather noisy. Indeed, as for the DWNT@FITC sample (fig. 3.4), we obtained a poor statistic on the measurement, despite an overnight accumulation which as to be compared with the few hours measurement of the other samples. As well as the DWNT@FITC sample, this one appeared to contain a very low amount of

nitrogen, and consequently, a very low quantity of adsorbed Cyanine remaining after the washing procedure. (Note that more evidences of the presence of Cyanine in this sample is presented in the Appendix A).

Process efficiency quantification from the DWNT-diamine-Cyanine sample

We need to redefine the relations between the XPS peaks area (chemical groups) and the number of molecules that belong to a given Model.

In the case of the DWNT-diamine-Cyanine sample, only the diamine-I contains $-NH_2$ groups, and there is still only one $-NH_2$ group and only one $-NH$ group per diamine-I when grafted on a DWNT (see figure 3.13). Thus, the relation $n(\text{diamine-I}) = n(NH)_I = n(NH_2)_{Tot} \propto A(NH)_I = A(NH_2)_{Tot}$ defined in chapter 3.1.1 is still valid. The amount of diamine-I is again accessible knowing the amount of $-NH_2$ groups. Concerning the Model II we find that for 1 mole of diamine-II there are 2 moles of $-NH$ groups (fig. 3.13). In the same way we did previously, we define $n(\text{diamine-II}) \propto \frac{A(NH)_{Tot} - A(NH_2)_{Tot}}{2}$. Finally, we need to define the amount of Hemicarboxonium which did not react with the diamine (Hemi-III) and, therefore, which is adsorbed onto the DWNTs. The quantity of diamine-II is equal to the quantity of Cyanine-II (since they are covalently bonded) therefore we can define that for 1 mole of diamine-II there is 1 mole of $-(N(Et)_2)_{II}$ that belongs to the Cyanine-II. And, $n(\text{Cyanine-II}) = n(\text{diamine-II}) \propto \frac{A(NH)_{Tot} - A(NH_2)_{Tot}}{2} = A(N(Et)_2)_{II}$. Thus, in order to know the amount of Hemi-III we simply remove the amount of $-(N(Et)_2)_{II}$ belonging to the Cyanine-II from the total $-N(Et)_2$ area. We thus define $n(\text{Hemi-III}) = n(N(Et)_2)_{III} \propto A(N(Et)_2)_{Tot} - \frac{A(NH)_{Tot} - A(NH_2)_{Tot}}{2}$.
Finally, using the different areas obtained with the fitting of the DWNT-diamine-Cyanine sample spectra (see table 3.8) the relative proportions of the three models present in the sample were determined and are presented

in table 3.10 hereafter.

	Model I	Model II	Model III
Relative proportions	0.32 ± 0.03	0.33 ± 0.02	0.35 ± 0.04

TABLE 3.10: Relative proportions of the three models constituting the DWNT-diamine-Cyanine sample given by the XPS measurements.

In order to determine the process efficiency we use the different ratio defined in the chapter 3.1.1. Here we redefine the expressions of the three ratios:

The covalent coverage ratio It represents the amount of diamine which reacted with the Hemicarboxonium comparatively to the total amount of diamine on the sample before the grafting. It is defined as the ratio between the number of moles of the diamine that reacted with the Hemicarboxonium and the total number of moles of diamine in the sample :

$$R_{cc} = \frac{n(\text{diamine-II})}{n(\text{diamine-I}) + n(\text{diamine-II})} \propto \frac{A(\text{NH})_{\text{Tot}} - \text{A}(\text{NH}_2)_{\text{Tot}}}{A(\text{NH})_{\text{Tot}} + \text{A}(\text{NH}_2)_{\text{Tot}}} \tag{3.4}$$

The non-covalent grafting ratio It represents the amount of Hemicarboxonium which is adsorbed onto the carbon nanotubes comparatively to the total amount of Hemicarboxonium and Cyanine in the sample. It is defined as the ratio between the number of moles of Hemicarboxonium that did not react (Hemi-III) and the total number of moles of Hemicarboxonium and Cyanine in the sample (Cyanine-II + Hemi-III) :

$$R_{ncg} = \frac{n(\text{Hemi-III})}{n(\text{Cyanine-II}) + n(\text{Hemi-III})} \propto \frac{2 \times A(\text{N}(\text{Et})_2)_{\text{Tot}} + A(\text{NH}_2)_{\text{Tot}} - A(\text{NH})_{\text{Tot}}}{2 \times A(\text{N}(\text{Et})_2)_{\text{Tot}}} \tag{3.5}$$

The covalent grafting ratio It represents the amount of Cyanine which is covalently grafted onto the carbon nanotubes comparatively to the total amount of Hemicarboxonium and Cyanine in the sample. It is defined as the ratio between the number of moles of Hemicarboxonium that did react (and became a Cyanine-II) and the total number of moles of Hemicarboxonium and Cyanine in the sample (Cyanine-II + Hemi-III). It is also by definition, simply the inverse ratio of the non-covalent grafting ratio:

$$R_{cg} = 1 - R_{ncg} = \frac{A(\mathrm{NH})_{\mathrm{Tot}} - A(\mathrm{NH_2})_{\mathrm{Tot}}}{2 \times A(\mathrm{N(Et)_2})_{\mathrm{Tot}}} \tag{3.6}$$

Using Eq. 3.4, 3.5 and 3.6, and using the XPS peaks area summed up in table 3.8 we find that $R_{cc} = 0.51 \pm 0.02$, $R_{ncg} = 0.52 \pm 0.05$ and $R_{cg} = 0.48 \pm 0.05$. The R_{cc} indicates that 51% only of the diamine available reacted with the Hemicarboxonium to form a covalent bond (see figure 3.16), which is slightly better than the FITC grafting process efficiency (R_{cc}=0.41), but still remain relatively low accordingly to our expectations. Then, comparing the R_{ncg} and the R_{cg}, indicates that the fluorophore stands in a situation very similar to the FITC and shows that about 50% of the total amount of Hemicarboxonium is covalently grafted onto the DWNTs while the other half of is simply adsorbed at the surface (see figure 3.17).

Therefore, beside the fact that the grafting process efficiency seems to be slightly improved with the Cyanine, we do not find major differences in between the FITC and the Cyanine accordingly to this XPS results. This lead us to conclude that, at least for the surface of the samples, the geometry of the two molecules does not seem to play an important role during the grafting process. Above all concerning the ratio between covalent and non-covalent grafting since the results of $\mathrm{R_{ncg}}$ and $\mathrm{R_{cg}}$ are almost the same for the two fluorophores.

In addition, since the Hemicarboxonium is not commonly used as a fluorophore for toxicity studies and since it becomes fluorescent only when covalently grafted to a diamine, these results could be less critical than the results obtain for the FITC in the chapter 3.1.1. Nevertheless, it is important to have in mind that biological media are often very complex. Indeed, we can easily imagine that, depending on the environment of the DWNT-diamine-Cyanine, the simply adsorbed fraction of Hemicarboxonium could anyway react with biological compounds and turn into a fluorescent Cyanine. This, of course, would also mislead the conclusions of such a toxicity experiment. Eventually, the results obtained with the DWNT@Cyanine sample (figure 3.15) indicates that, in the absence of diamine, the quantity of Cyanine adsorbed at the surface of the DWNTs is very low after the washing procedure while it is not the case for the DWNT-diamine-Cyanine. As the same trend was observed for the FITC-containing samples, it brings more evidence to our previous supposition that stated that the 1,4-diaminobutane could have a strong influence on the ability of the fluorophore to remain adsorbed on the nanotubes despite thorough washing.

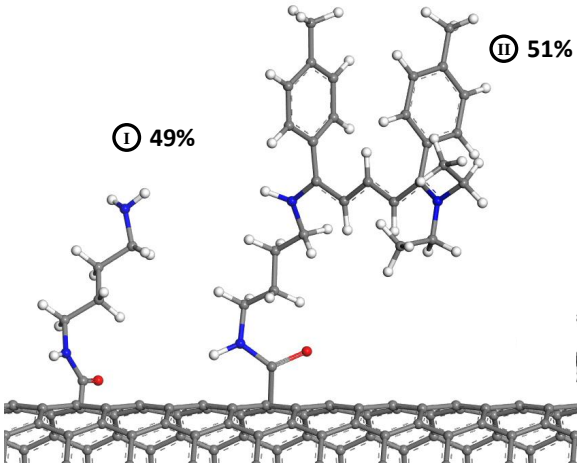

FIGURE 3.16: *Representation of the results given by the R_{cc} for the DWNT-diamine-Cyanine surface.*

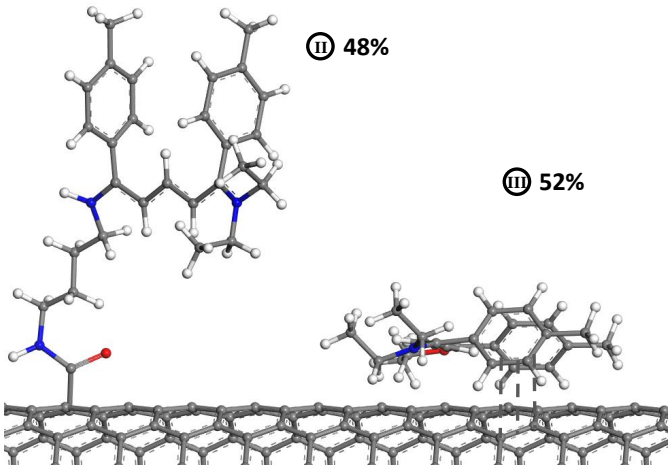

FIGURE 3.17: *Representation of the results given by the R_{ncg} and the R_{cg} for the DWNT-diamine-Cyanine surface.*

3.2.2 Inelastic Neutron Scattering

In this part of the manuscript, please note that for Cyanine-containing samples, the conditions of INS measurement and simulations were the same as for the FITC-containing sample mentioned in the chapter 3.1.2. The reader should refer to this specific chapter for the detailed procedures used in the following analysis.

Concerning the simulations, we kept our three previous model system

with the periodic single-walled carbon nanotube (SWNT) (6,6) of 8.14 $\mathrm{\AA}$ diameter placed in a triclinic lattice, and we simply replace the FITC by an Hemicarboxonium molecule. The three new models obtained still represent the three extreme cases that can be found at the end of the grafting process. The first model is not changed and correspond to a SWNT with one molecule of linker covalently bonded to it, representing the case of 0% of Cyanine grafted (SWNT-linker). The second model represents the case where 100% of the Hemicarboxonium turned into a Cyanine by creating a covalent bond with the linker. It will be referred as "SWNT-linker-Cya". Again, for the SWNT-linker-Cya model, a search of the lowest energy space conformation was performed using the module "Conformers" in Materials Studio, and the lowest energy space conformation was kept for the density functional theory (DFT) calculations. Finally, the third model is constituted of one SWNT and one Hemicarboxonium adsorbed on the nanotube. It represents the case were 100% of the Hemicarboxonium did not react with the linker. It will be referred as "SWNT@Hemi" from now on.

DFT calculations results

The results of the DFT calculations performed on the three model systems SWNT-linker, SWNT-linker-Cya and SWNT@Hemi, are presented in figure 3.18. As for the FITC, this figure compares the hydrogen partial density of states ($\mathrm{g_H}(\omega)$) for the three models and allows to identify characteristic vibrational bands (see table 3.11).

By comparing the figure 3.18-a and the figure figure 3.18-b, we first notice that vibrational band at 1620 $\mathrm{cm^{-1}}$, previously associated to the bending modes of the -$\mathrm{NH_2}$ groups of the linker, disappeared once the Hemicarboxonium is covalently bonded to the linker. This characteristic vibration is still isolated from the other modes and is still clearly identifiable. It is thus kept

as the signature of the disappearance of the -NH_2 groups which is characteristic of the covalent grafting of the Hemicarboxonium onto the DWNTs. In the bending region, the three models present the set of modes at 1270-1380 and 1440-1480 cm^{-1} corresponding to the bending vibrational modes of the -CH groups. Contrarily to the FITC, the Hemicarboxonium is composed of both -CH sp^2 and sp^3 so that no distinction can be made in this region of the spectrum. Nevertheless, in the stretching region the signatures of the two types of -CH can be distinguished. Indeed the signatures of the -CH sp^3 were found for the three models between 2890 and 3090 cm^{-1}. Similarly, on figures 3.18-b and 3.18-c, the presence of the Hemicarboxonium brought new vibrational modes arising at 3100-3160 cm^{-1} which are characteristic of the -CH sp^2 constituting the 6-carbon rings of the Hemicarboxonium. Eventually, the vibrational modes of the -NH and -NH_2 were found within 3420-3510 cm^{-1}. But again in this case, the vibrational bands being so close to each other, leaved us with low expectations concerning their use in differentiating the different $GDOS_{exp}$ obtained before and after the grafting process.

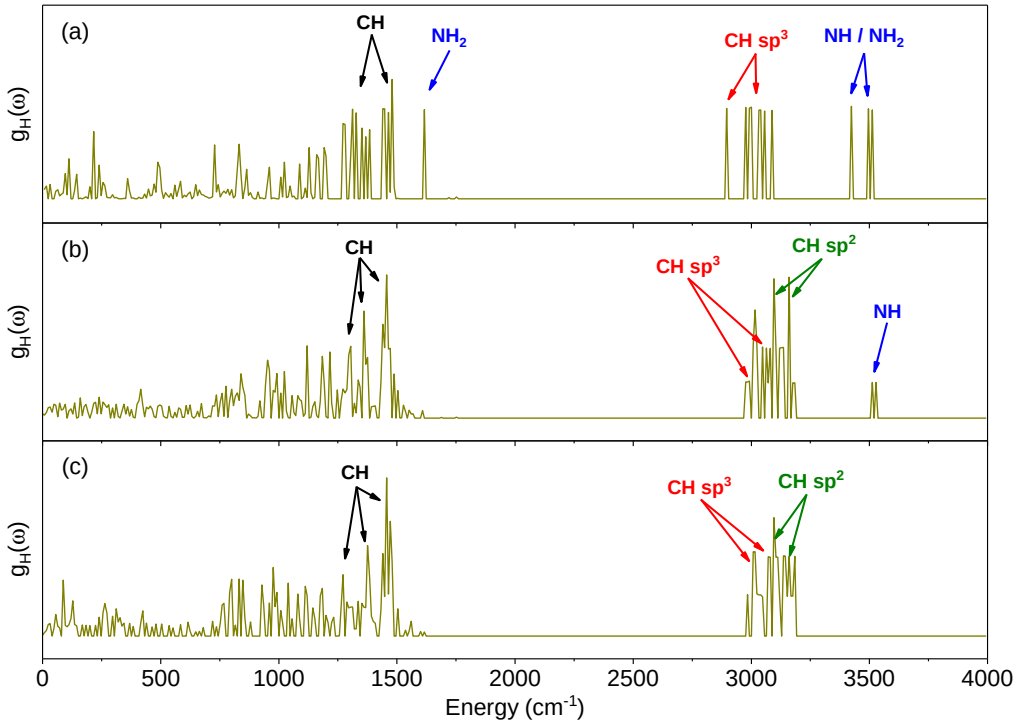

FIGURE 3.18: *Comparison of the $g_H(\omega)$ obtained via DFT calculations for the three models : (a) the SWNT-linker, (b) the SWNT-linker-Cya and (c) the SWNT@Hemi.*

Modes (cm^{-1})	SWNT-linker	SWNT-linker-Cya	SWNT@Hemi
740-1080	Bending -CH (out of plane)	Bending -CH (out of plane)	Bending -CH (out of plane)
1230-1480	Bending -CH (in plane)	Bending -CH (in plane)	Bending -CH (in plane)
1600-1640	Bending $-NH_2$ (in plane)	-	-
2850-3250	Stretching -CH	Stretching -CH	Stretching -CH
3400-3550	Stretching -NH/$-NH_2$	Stretching -NH	-

TABLE 3.11: Vibrational modes of interest for the three model systems: SWNT-linker, SWNT-linker-Cya and SWNT@Hemi.

INS evidences of the covalent grafting of the Cyanine

As for the FITC, the first step before the quantification of the grafting efficiency is to give the proof that the covalent grafting of the Cyanine did occur. In order to do so, we used the same method developed in the chapter 3.1.2, and which consists identifying the characteristic signatures of the covalent grafting on reference samples (without any DWNT) prior to analyze the real ones. We thus chose to compare the three following reference samples (refer to chapter 2.1.4 and figure 2.10 for details) :

1. The Diamine sample (commercial 1,4-diaminobutane).
2. The Cyanine sample (synthesized $5\mathrm{Me}(\mathrm{NEt}_2)_2$)).
3. The Diamine-Cyanine sample (product of the chemical reaction of the Diamine and the Hemicarboxonium, witnessing the covalent grafting).

Figure 3.19 shows the experimental results of the INS spectroscopy performed on the reference samples in the energy range comprised between 500 and 4000 cm^{-1}. First, comparing the spectra of the Diamine sample (pink line) and the Diamine-Cyanine sample (pale blue line), we were able to find that the four isolated characteristic vibrational bands centered at 760, 910, 1050 and 1620 cm^{-1} also disappeared in the case of the grafting of the Hemicarboxonium (notice that these bands are the same that the ones which disappeared on the Diamine-FITC reference sample spectrum). Again these bands, strongly modified during reaction, were chosen to evidence the covalent grafting of the Hemicarboxonium on the linker. Eventually, by comparing the results for the Diamine-Cyanine sample (pale blue line) and the Cyanine sample (orange line), we were able to associate the presence of Cyanine after the grafting process to two sets of characteristic vibrational bands between 800-875 cm^{-1} and between 900-1250 cm^{-1}.

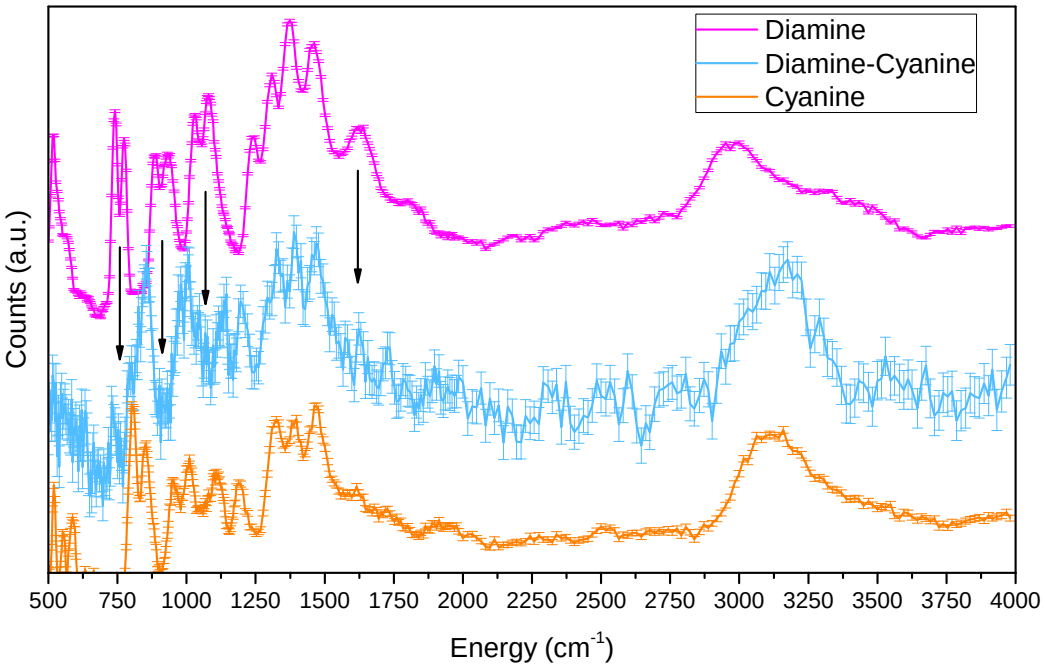

FIGURE 3.19: *Comparison of the experimental INS spectra obtained for the reference samples : Diamine (pink line), Diamine-cyanine (light blue line) and Cyanine (orange line)*

Once we obtained this characteristic vibrational bands on the reference samples, witnessing the covalent grafting of an Hemicarboxonium turning into a Cyanine, we could compare the DWNT-containing samples and tried to find evidence that the covalent grafting did occur after the functionalization process. Figure 3.20 compares the INS spectroscopy experimental results obtained for the DWNT-diamine and the DWNT-diamine-Cyanine samples. These two samples represent respectively the step before (blue line) and the step after the grafting process of the Cyanine (red line). By looking for the characteristic vibrational bands identified above, we were able to associate the growth of the bands located at 845, 985 and 1195 cm^{-1} (green arrows) to the presence of either the Cyanine or the Hemicarboxonium in the sample after the process. Indeed, as we were not able to measure by means of INS spectroscopy a reference sample of pure Hemicarboxonium we could not be sure that these vibrational bands strictly belongs to the Cyanine. It is even

very likely that these vibrational bands are the same for the Cyanine and the Hemicarboxonium since the two molecules are very similar. Nevertheless, we could identify a decrease of the bands at 740, 920 and 1060 cm^{-1} (pink arrows) associated to the covalent grafting of the Cyanine onto the diamine that gave the confirmation that a significant amount of diamine reacted with the Hemicarboxonium forming covalent bonds.

Unfortunately, as for the FITC-containing samples (fig. 3.10), the vibrational band at 1620 cm^{-1} did not present any sign of decreasing after the grafting process, while it was expected to be the most affected by the formation of a covalent bond between the diamine and the Hemicarboxonium. It was again attributed to the distortions carried by multiphonon events in the range of 1500-2000 cm^{-1} where the presence of phonon wings is clearly visible (refer to Appendix B for more details on multiphonon events). Thus, the multiphonon contributions to spectra needed to be taken into account.

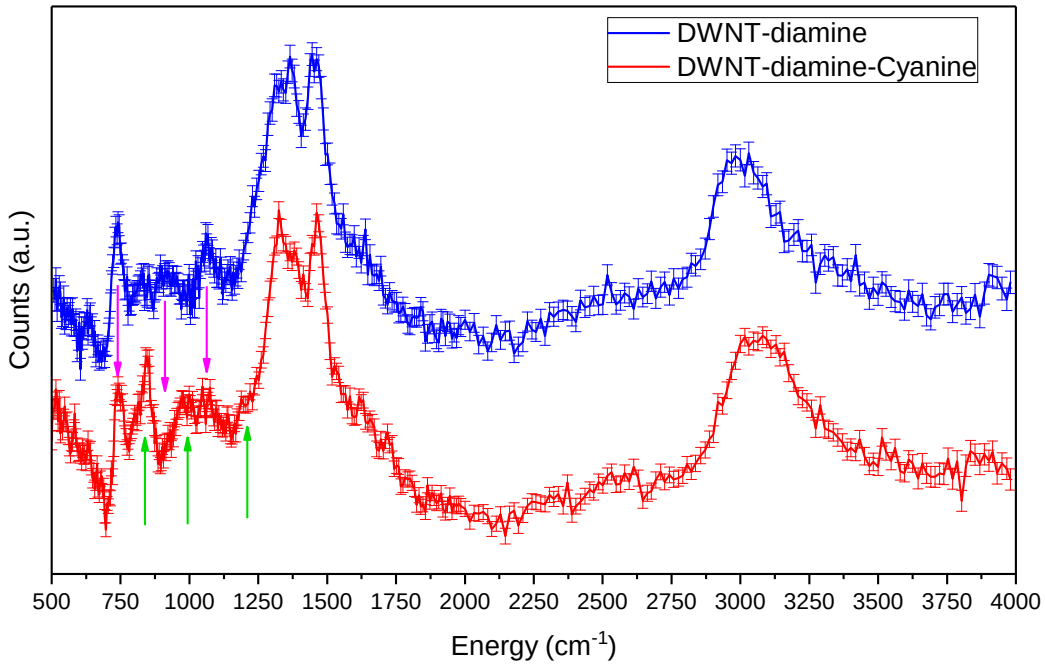

FIGURE 3.20: *Comparison of the experimental INS spectra obtained for the DWNT-diamine (blue line) and the DWNT-diamine-Cyanine (red line) samples.*

Quantification of the grafting efficiency

In order to be able to quantify the different proportions of species present in the bulk of our DWNT-diamine-Cyanine sample, we reproduced the method used in the chapter 3.1.2. Indeed, we used the $g_H(\omega)$ obtained for our three models representing the different extreme cases that could be found after the grafting process (fig. 3.18) and mixed them using various ratio to best fit our experimental data. Figure 3.21 shows the experimental generalized density of states ($GDOS_{exp}$) measured in the energy range 500-4000 cm^{-1} for the DWNT-diamine-Cyanine sample (Red lines). Figure 3.21 also shows the result of mixing of the $g_H(\omega)$ obtained for the SWNT-linker, the SWNT-linker-Cya and the SWNT@Hemi models in the proportion of respectively 60%/20%/20%, corresponding to the best fit obtains for the $GDOS_{exp}$. These mixed $g_H(\omega)$ were convoluted with the experimental resolution (3% of the energy)(Cyan lines). It shows as well the corresponding calculated multi-phonon contributions for these models (green line) and the resulting theoretical generalized density of states ($GDOS_{th}$) which corresponds to the sum of the mixed $g_H(\omega)$ and multiphonon contributions (Appendix B), convoluted with the experimental resolution (blue line).

Looking at the $GDOS_{th}$ on figure 3.21, we see that the mixing proportion of 60%/20%/20% are in good agreement with the experimental data. Indeed, it reproduces well the $GDOS_{exp}$ of the vibrational bands defined previously for the increased ones at 845, 985 and 1195 cm^{-1}. It also shows at 740, 920 and 1060 cm^{-1} that the vibrational bands decreased during the grafting process. Concerning the vibrational band around 1600 cm^{-1}, characteristic of the presence of -NH_2 groups and where the largest differences were expected after the grafting, we see once again that the multiphonons are responsible of the apparent lack of change in its intensity. Indeed, as for the DWNT-diamine-FITC, the decrease in intensity undergone by the 1600 cm^{-1} vibration was

compensated by the resulting multiphonon intensity associated to the bending region (500-2000 cm^{-1}) fundamental vibrations. Then by looking at the resulting $\mathrm{GDOS}_{\mathrm{th}}$, this vibrational band intensity then appears to be almost unchanged despite the fact that 25% of the linker reacted with the Hemicarboxonium. However, unlike the DWNT-diamine-FITC sample, the attempt to fit the $\mathrm{GDOS}_{\mathrm{exp}}$ with the ratio given by the XPS measurements were unsuccessful. Indeed, using the ratio 32%/33%/35% corresponding to the respective proportions of Model I, Model II and Model III used for the XPS data analysis, we found that not only the changes in the vibrational bands in the 740-1200 cm^{-1} region were badly reproduced, but also that the decrease of intensity of the 1620 cm^{-1} vibrational band was not sufficiently compensated by the multiphonon contribution. This latter loss of intensity would thus be clearly visible on the DWNT-diamine-Cyanine INS spectrum if the bulk (INS technique) and the surface (XPS technique) would be similar.

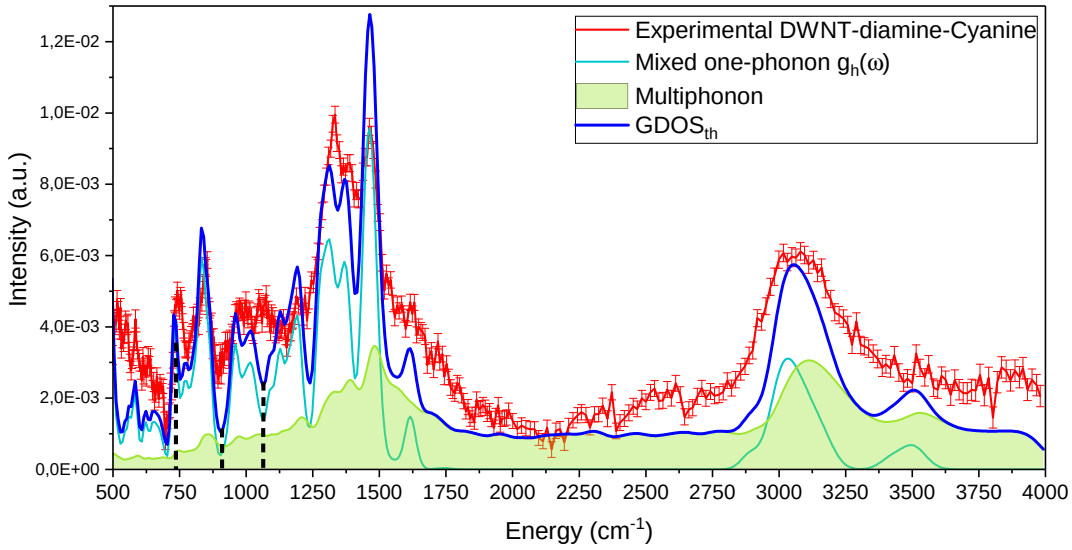

FIGURE 3.21: *Comparison of the* $\mathrm{GDOS}_{\mathrm{th}}$ *(taking into account the multiphonon contribution) calculated for a mixing ratio of 60%/20%/20% with the INS experimental spectra for the DWNT-diamine-Cyanine sample.*

These latter results bring new evidences that the surface and the bulk of

the sample behave differently during the grafting process. By comparing the results obtained by means of the XPS and INS techniques for both fluorophores, it seems that the bulk of the samples is always more difficult to functionalize than their very surface. Moreover, we demonstrated, analysing the surface of the DWNT@FITC (chapter 3.1.1) and the DWNT@Cyanine (chapter 3.2.1) samples, that the presence of the diamine could play an important role in the non-covalent functionalization of the samples.
One potential explanation that satisfies the results obtained for both fluorophores could be that, once the diamine is grafted on the DWNTs it furthers the agglomeration of the nanotubes, forming bundles hardly accessible to any chemicals (fluorophores or solvents). Therefore it would be more difficult both to functionalize the diamine and to remove the adsorbed fluorophores within those bundles.

Nevertheless, beside this possible explanation, we notice that these results are again similar to the results obtained for the FITC by means of the INS spectroscopy. Indeed, for both fluorophores the mixing ratio of 60%/20%/20% appeared to best fit our data. These results combined with those of the XPS measurements lead us to strongly believe that the different geometries of our fluorophores do not make any significant changes during the grafting process in terms of covalent and non-covalent grafting ratio. Finally, in order to go further with the analysis of the impact of the geometry on the non-covalent grafting mechanisms and hoping to confirm our experimental conclusions, we decided to study and compare the adsorption energy of our two fluorophores with the help of computational calculations.

3.3 Study of the adsorption energy for both fluorophores

In this chapter the main differences between the FITC and the Hemicarboxonium in terms of adsorption interaction with the carbon nanotubes were studied. In order to compare them in such a way we chose to use DFT calculations to calculate the respective energies of both adsorbed systems (Hemicarboxonium and FITC adsorbed onto CNTs), and thus have an idea of the energies involved in their interactions with the nanotubes. The aim of this part is obviously not to give a complete description of the different types of interactions involved in the adsorption of the molecules on the CNTs, this would probably necessitate a project entirely dedicated to this goal since the interactions can be very complex when it comes to aromatic molecules. Rather, the aim of this part is to quantify the energies involved in such weak interactions and to attempt to determine whether or not the geometries of the molecules could play a role in the non-covalent grafting outcome of the functionalization process. We then selected the two non-covalent models, SWNT@Fluo and SWNT@Hemi, for this study. In practice, from the two models geometrically optimized, we performed DFT calculations using the DMol3 module of Materials Studio with the GGA-PBE functional and calculated the total energy of our model systems for different configuration. This allowed us to determine the energy profile of our systems related to this different chosen configuration. Then from the lower energetic configuration, we subtracted the total energy of the individual SWNTs and fluorophores. Therefore, this difference between the total energy of the systems and the sum of the individual energies gave us the energy of interaction between the SWNTs and the fluorophores, i.e. the adsorption energy E_{ads}, and such as :

$$E_{ads} = E(\text{SWNT+Fluorophore}) - E(\text{SWNT}) - E(\text{Fluorophore}). \quad (3.7)$$

This calculation allowed us to obtain the adsorption energies for different model systems, and obtain a clearest vision of the energies involved when the fluorophores interact with the CNTs. Finally, as it was mentioned earlier, the limited numbers of atoms in our models forced us to use small diameter SWNTs. In order to understand what could be the effect of the curvature of the CNTs on the adsorption of the molecules, we also performed single point energy calculations on two models were the SWNTs were replaced by a graphene mono-layer. These results are presented hereafter.

3.3.1 Adsorption energy study of the FITC

In order to verify that the adsorption interaction was likely to happen during the functionalization process we needed to prove that the configuration where the FITC is adsorbed at the surface of a nanotube was less energetic than the configuration where the nanotubes and the fluorophores are sufficiently distant to be considered not interacting. From our geometrically optimized SWNT@Fluo model, the parameter used for the single point energy calculations were the distance between the SWNT and the FITC (see figure 3.22). Therefore for each step (distance), the energy of the system was calculated.

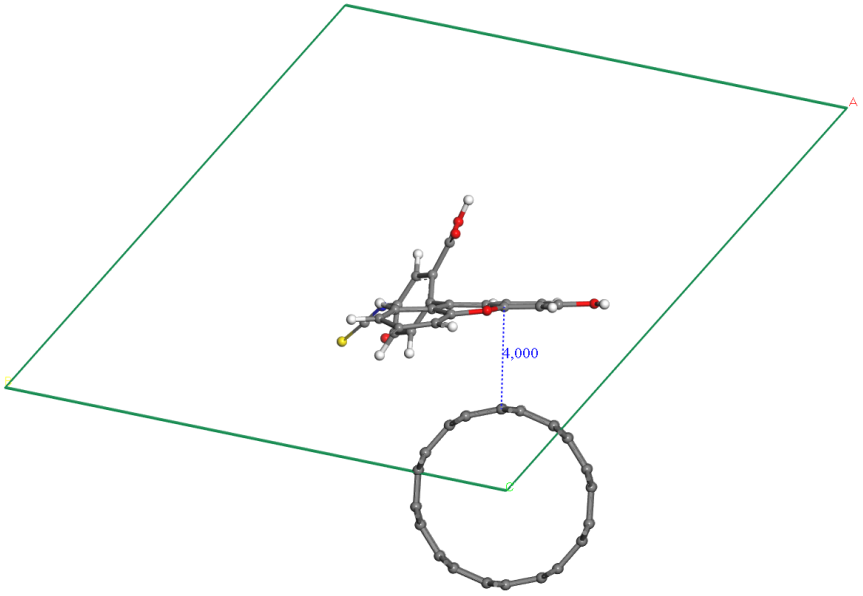

FIGURE 3.22: *Representation of the model SWNT@Fluo, chose for the calculation of single point energy of a FITC molecule interacting with a single-walled carbon nanotube.*

Figure 3.23 shows the energy profile of the FITC interacting with a SWNT as a function of the SWNT - FITC distance. Figure 3.23 shows that the interaction between the SWNT and the FITC exhibits a minimum of energy of -6204.13515 Ha at a distance of 3.75 Å. When the fluorophore gets closer to the tube we see that the single point energy of the system increase rapidly due to repulsive forces between electronic orbitals of the SWNT and the FITC. When the FITC is taken away from the CNT the energy increases more softly until the FITC undergoes the influence of a neighboring SWNT and then start to decrease again. The minimum found in the energy profile suggests that the FITC would have a strong tendency to adsorb onto the SWNT, stacked at 3.75 Årather than remaining individualized.

From this minimum energy value of -6204.13515 Ha, that correspond to the energetically more favorable position, the corresponding adsorption energy E_{ads} was calculated using equation 3.7:

$$E_{ads}(\text{SWNT@Fluo}) = -0.06854 \text{ Ha} = -1.86506 \text{ eV} = -43.00884 \text{ kcal.mol}^{-1}$$

Notice that a system owning negatives values of E_{ads} indicates that the studied configuration of the system is less energetic than the individualized molecules and that the system would rather naturally evolve toward this configuration.

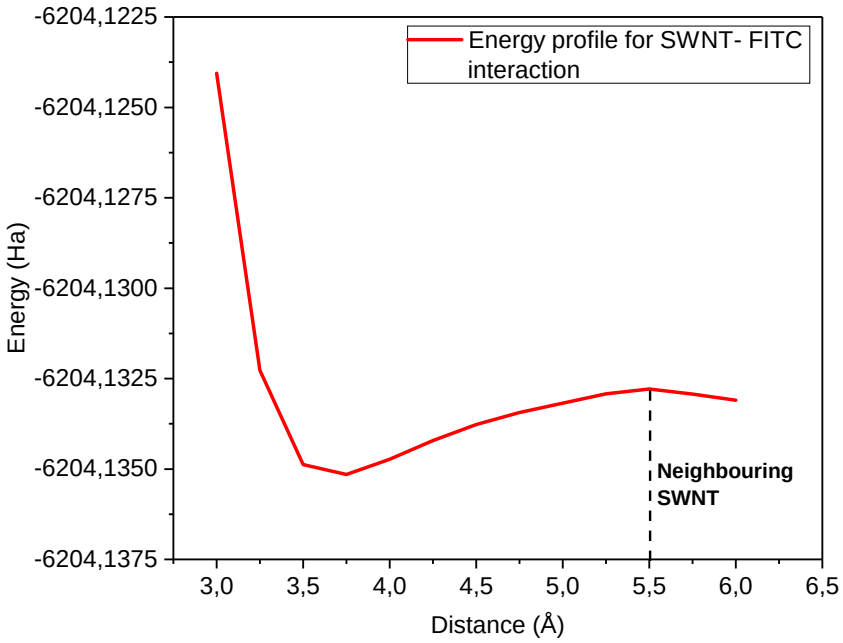

FIGURE 3.23: *Energy profile of the interaction of the FITC and a single-walled carbon nanotube.*

Nevertheless, as it has been mentioned already, in order to optimize our computational calculation speed we had to use small SWNT (6,6) of 8.14 Å diameter, while the outer-wall diameter of the DWNTs in our samples is typically around 2.0 nm. The single point energy results we obtained on SWNT (6,6) could then be biased by the high curvature of the wall in our models and could thus be different from the actual energy in the real samples.
To overcome this issue, we decided to study another model of infinite diameter representing the extreme case where the SWNT would be very large and where it would appear to own a zero-curvature from the point of view of the stacked fluorophore. Indeed, simulating a mono-layer of carbon atoms (graphene) necessitates relatively few atoms per lattice and fits our requirements in terms of calculation speed. Figure 3.24 shows a representation of

the model chose for the calculation of single point energy of a FITC molecule interacting with a mono-layer of graphene, this model will be referred as "Graphene@Fluo". The graphene and the FITC were placed in a cubic lattice. The graphene layer was oriented parallel to the plane define by the $\overrightarrow{a}$ and $\overrightarrow{b}$ b vectors of the lattice and the lattices parameters were chosen as following : a = 23.100 Å, b = 18.671 Å, c = 20.000 Å ; $\alpha = 90°$, $\beta = 90°$, $\gamma = 90°$.

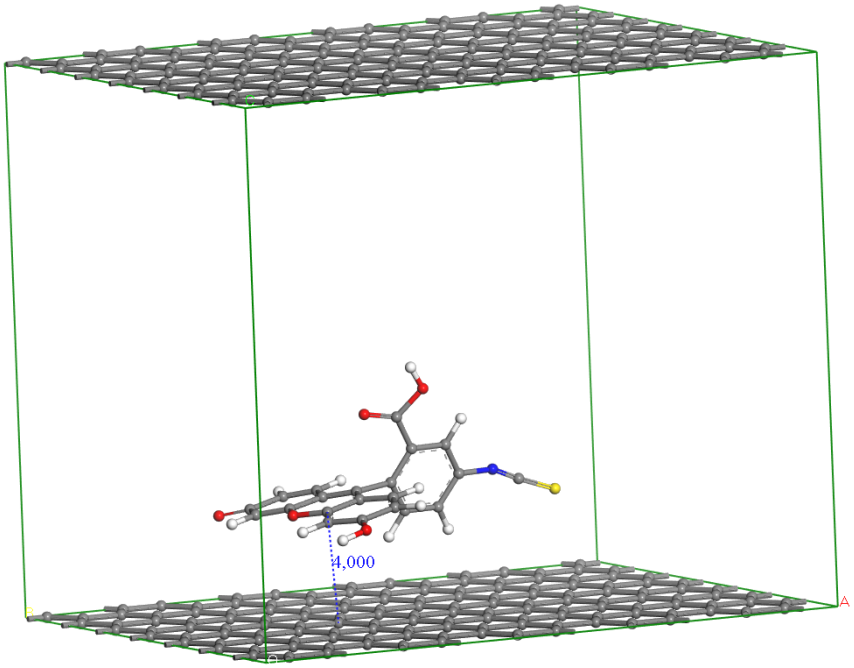

FIGURE 3.24: *Representation of the model Graphene@Fluo chose for the calculation of single point energy of a FITC molecule interacting with a mono-layer of graphene.*

On the Graphene@Fluo model, we performed the same simulations as for the SWNT@Fluo and were able to find the corresponding energy profile. This profile is displayed on figure 3.25. We see that, for this new model, the minimum of energy was found at -6964,755242 Ha for a Graphene - FITC distance of 4 Å. We then calculated the E_{ads} from this minimum in energy with the help of equation 3.7, and found :

$$E_{ads}\text{(Graphene@Fluo)} = -0.07073 \text{ Ha} = -1.92454 \text{ eV} = -44.38057 \text{ kcal.mol}^{-1}$$

By comparing the profiles of the SWNT@Fluo and the Graphene@Fluo, we see that both samples own adsorption energies that are very close but that the Graphene - FITC distance at the equilibrium is slightly higher. This could be explain by the steric hindrance of the isolated perpendicular 6-carbon ring of the FITC that can be overcome by the curvature of the SWNT, allowing the molecule to get slightly closer to the surface.

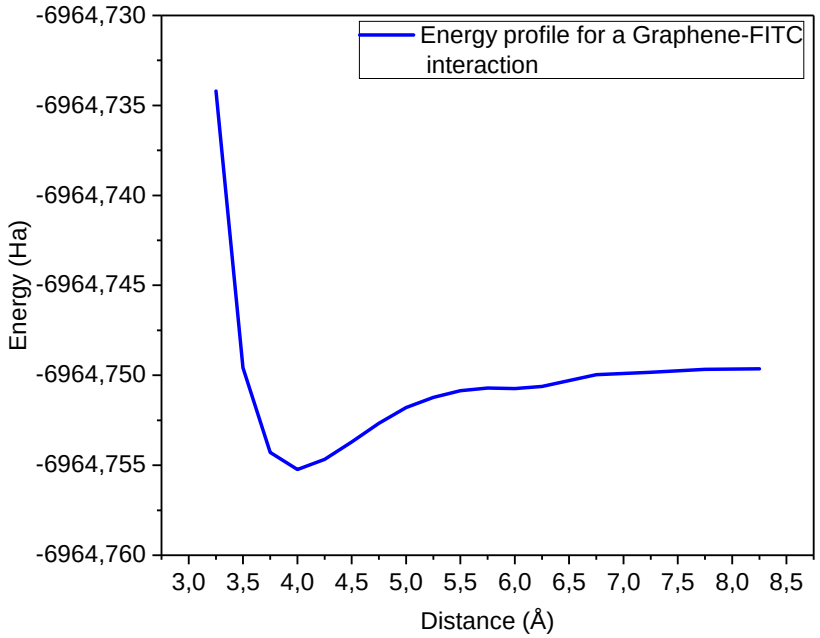

FIGURE 3.25: *Energy profile of the interaction of the FITC and a graphene monolayer.*

Finally, from the two previous models we see that the configuration where the fluorophore is adsorbed at the surface is still the more favorable configuration. These results lead us to believe that the FITC is very likely to adsorb onto the DWNTs during the functionalization process since the simulations showed that the energy of the systems find a minimum when the fluorophores and the SWNTs are involved in adsorption interactions and this, regardless of the diameter of the nanotubes.

3.3.2 Adsorption energy study of the Hemicarboxonium

The study of the adsorption energy of the FITC on the CNTs gave us a good starting point to be compared with the Hemicarboxonium which owns a different geometry. As this latter molecules is constituted of two 6-carbon rings almost parallel to one another and perpendicular to the main carbon chain, we could expect some difference in the way it interacts with the CNTs (see figure 3.26).

Nevertheless, this new geometry requires a slightly different approach. Indeed, the two 6-carbon rings are theoretically free to rotate, due to their single C-C bond that connect them to the main carbon chain. For this reason two parameters were chosen for the single point energy profile calculation: the distance between the SWNT and the fluorophore (as for the FITC), and in addition the orientation of the rings. More specifically, the torsion angles of the two rings with the main chain were changed, so that for 90° the rings form two distinct parallel planes (see inset of figure 3.26), and for 0° the rings are parallel and contained in the same plane.

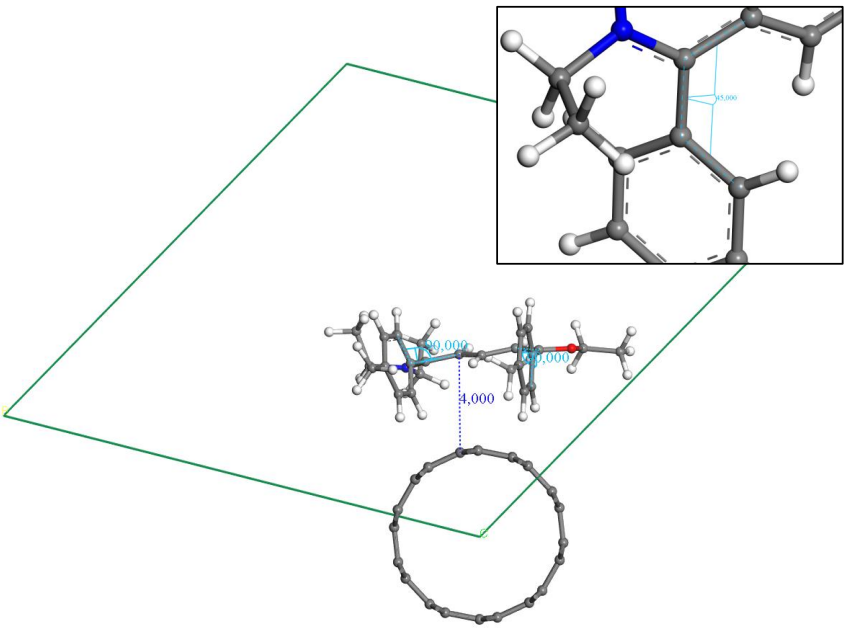

FIGURE 3.26: *Representation of the model SWNT@Hemi, chose for the calculation of single point energy of a Hemicarboxonium molecule interacting with a single-walled carbon nanotube.*

Taking into account this new parameter allowed us to plot 2D colormaps representing, here again, the energy profile of the interaction of the Hemicarboxonium with a SWNT. Figure 3.27 shows this single point energy profile for the Hemicarboxonium interacting with a SWNT as a function both of the SWNT - Hemicarboxonium distance and the torsion angle the rings make with the main carbon chain. We see on figure 3.27 that the interaction between the SWNT and the Hemicarboxonium shows a minimum of energy at -5670,10662 Ha for a distance of 4.3 $\mathring{\text{A}}$ and for a torsion angle of 52.5°. First, these results confirm, as for the FITC, that there is a minimum of energy in the proximity of the SWNT that suggests the Hemicarboxonium tendency to adsorb on the surface of the tube rather than remaining individualized. Then by looking at the angles of the rings at this energetic minimum we clearly see that they found an equilibrium position around 52.5° where, when the molecule is individualized, the value of this angle is between 80 and 90°. This illustrates the competition between the natural position of the rings (facing each other) and the less energetic position for the interaction with the SWNT (probably facing the surface of the tube). We noticed that the energy of the system increase rapidly for the angles comprised between 40 and 0° which showed us that the configurations below 40° were very unlikely to happen. Finally, we also calculated the E_{ads} at this minimum in energy still using equation 3.7, and found :

$$E_{ads}(\text{SWNT@Hemi}) = -0.04272 \text{ Ha} = -1.16248 \text{ eV} = -26.80954 \text{ kcal.mol}^{-1}$$

This result must be compared with the one obtained with the FITC. Indeed, if the distance between the SWNT and the two fluorophores can not be compared from one molecule to another (because of the two distinct geometries), we can compare the adsorption energies of the two SWNT systems. We see that, in terms of adsorption energy it seems that the interactions of the

Hemicarboxonium with the SWNT are weaker (-26.80954 kcal.mol^{-1}) than the interactions of the FITC with the same SWNT (-43.00884 kcal.mol^{-1}).

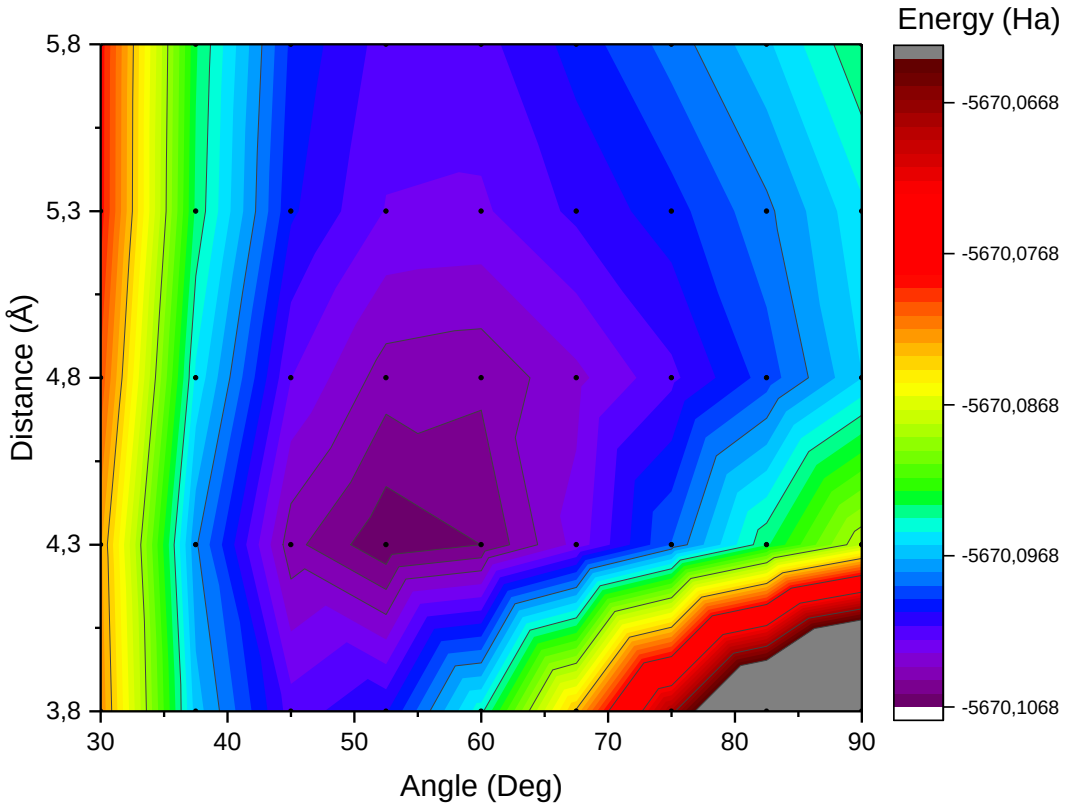

FIGURE 3.27: *2D colormap energy profile of the SWNT@Hemi model, representing the variation of the energy of the system as a function of both the SWNT - Hemicarboxonium distance and the torsion angle of the rings.*

In order to go further, and as we did for the FITC, we investigated the influence of the curvature of the CNTs on the adsorption energy. To do so, we again used a graphene mono-layer in the same way we did for the Graphene@Fluo, and made our simulation including variations in the 6-carbon rings torsion angles, this model will be referred as "Graphene@Hemi" (see figure 3.28).

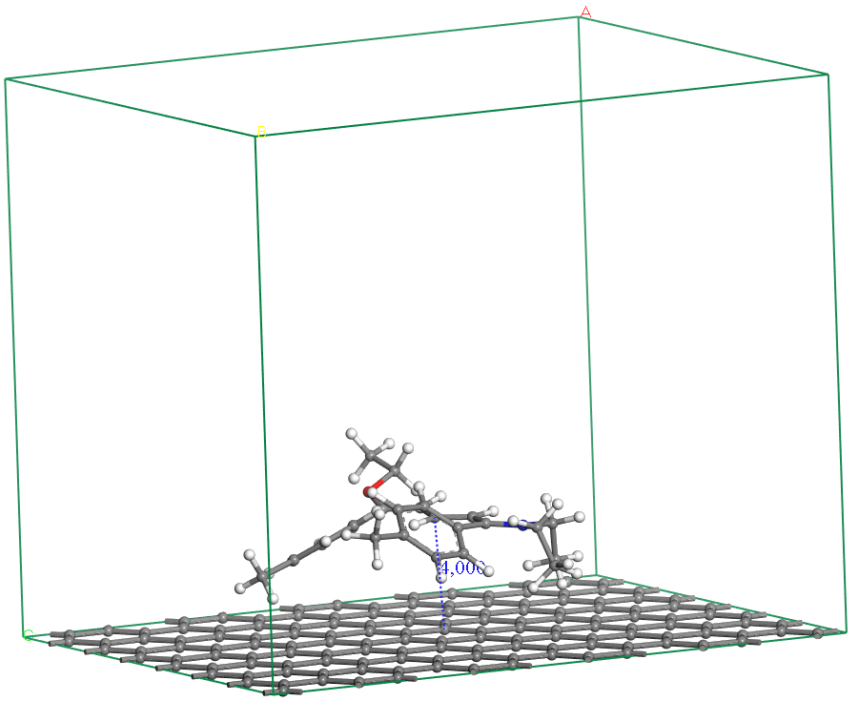

FIGURE 3.28: *Representation of the model Graphene@Hemi chose for the calculation of single point energy of a Hemicarboxonium molecule interacting with a mono-layer of graphene.*

The results of the single point energy calculations on this model allowed us to plot again the 2D colormap energy profile of the system, and are presented in figure 3.29 which represents the energy profile for the Hemicarboxonium interacting with a graphene mono-layer as a function of both the Graphene - Hemicarboxonium distance and the torsion angle the rings make with the main carbon chain. We see for this plot that the minimum of energy has moved compared to the SWNT@Hemi, and stands now at an energy of -6430,7118 Ha for a distance of 5.3 Å and for a torsion angle of 67.5°. First this results indicate that, when the diameter of the CNTs increases, the Hemicarboxonium is not able to get as close at the tube as for the small diameter CNTs, but also that the rotation of the rings is less important and is much closer to its original position (individualized Hemicarboxonium). We then calculated the E_{ads} at this minimum in energy with the help of equation 3.7,

and found:

$$E_{ads}(\text{Graphene@Hemi}) = -0.0416 \text{ Ha} = -1.13192 \text{ eV} = -26.10249 \text{ kcal.mol}^{-1}$$

Comparing the SWNT@Hemi and the Graphene@Hemi, we see that the adsorption energy slightly decreases when the diameter of the CNTs increases, probably because the rotation of the rings find an equilibrium position further from facing the 6-carbon rings of the graphene layer.

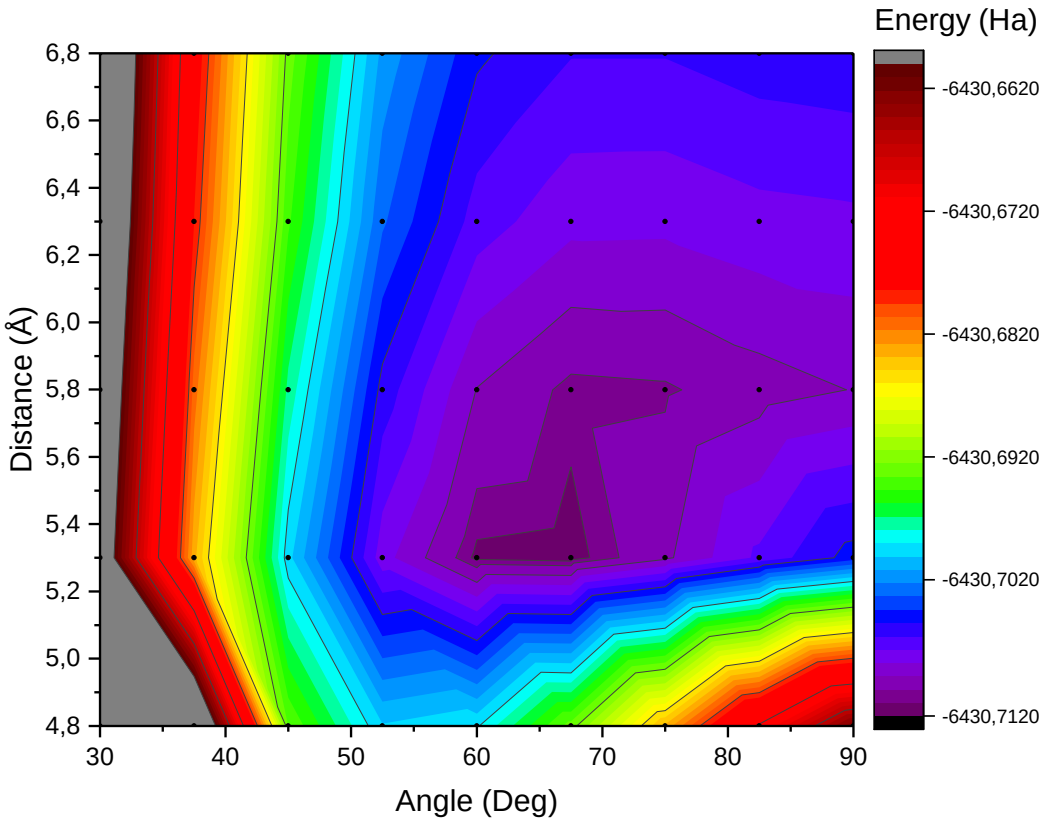

FIGURE 3.29: *2D colormap energy profile of the Graphene@Hemi model, representing the variation of the energy of the system as a function of both the Graphene - Hemicarboxonium distance and the torsion angle of the rings.*

By comparing now the results obtained for the two molecules, both molecules present a minimum of energy in the vicinity of the SWNTs that make us believe they would both preferably adsorb on the CNTs instead of remaining individualized, regardless the diameter of CNTs. In addition, we

found that the two molecules exhibits different adsorption energies on the SWNTs, with an adsorption energy in the order of -44 kcal.mol^{-1} for the FITC and in the order of -26 kcal.mol^{-1} for the Hemicarboxonium. This difference in E_{ads} indicates us that the geometry of the molecules might eventually play a role in the way they interact with the CNTs. Although, we have to be very careful with this assumption since not only the geometry is different between the two molecules but also the number of their 6-carbon rings as well as the chemical groups they contains. It is then better not to conclude on the influence of the geometry itself, but rather notice that the two molecules interact indeed with different adsorption energies on the SWNTs of our model and that this difference is not visible in our experimental results so far.

Chapter 4

Conclusions and Perspectives

The aim of this Ph.D. project was to study the grafting of the FITC on double-walled carbon nanotubes. Indeed, as the FITC is a fluorophore commonly used as fluorescent marker for toxicity studies on carbon nanotubes, the understanding of the efficiency of its grafting process onto CNTs was fundamental to be able to answer the concerning questions raised by the intrinsic drawbacks of the fluorescence techniques.
The strategy carried out in this thesis was to analyze both the surface and the bulk of our samples using two complementary spectroscopic techniques, X-ray photoelectron spectroscopy and inelastic neutron scattering spectroscopy. This approach allowed us to quantify, for the first time, the competition between covalent and non-covalent functionalization of DWNTs with FITC molecules, and led to concerning results about the grafting process efficiency.

First of all, the analysis of the surface of our FITC-containing samples by means of XPS allowed us to determine that only 41% of the diamine available, at the surface of the DWNT-diamine-FITC sample of interest, reacted with the FITC to form covalent bonds, which indicated that the efficiency of the covalent grafting could certainly be further improved. In addition, this study also allowed us to evidence that a significant fraction of the FITC at the surface of the sample stands in a non-covalent interaction with the

DWNTs despite thorough washings with appropriate solvents, since our results showed that 47% of the total amount of FITC was simply adsorbed onto the carbon nanotubes. This means, by extension, that potentially half of the fluorescence visible at the surface of our sample can be attributed to weakly-bonded molecules, which could undergo desorption at some point along their journey in biological media. Then, the bulk of our sample of interest was analyzed using inelastic neutron scattering spectroscopy coupled to DFT calculations and a similar trend was evidenced. The experimental results obtained and the vibrational density of states calculated from our models provided us evidences that both covalent and non-covalent grafting were present in the bulk of our sample. Indeed, our results showed that, in the best grafting case scenario, we could expect the bulk of the sample to be similar to its surface, but that the situation could be even worse with only 25% of the total diamine available that reacted with FITC molecules, and still 50% of the total FITC standing in weak interaction with the DWNTs. These results, provided by both spectroscopic techniques (XPS, INS), confirmed that, although the covalent functionalization strategy commonly used in toxicity studies for the marking of DWNTs assumes strong covalent interactions with the fluorophores, a non-negligible part of the FITC may indeed be only adsorbed even after thorough washings of the samples.

The influence of the geometry of fluophores was also investigated in order to consider potential alternative fluorescent molecules. The Cyanine $5\mathrm{Me(NEt_2)_2)}$ synthesized at the laboratory of *Synthèse et Physico-Chimie de Molécules d'Intérêt Biologique* (SPCMIB), was selected for its very different geometry from the one of FITC, and the same approach as in the case of FITC samples was proposed (XPS, INS, DFT calculations). The experimental results obtained indicated that the geometry of the Cyanine do not show any significant influence on the grafting process efficiency since the relative

proportions of covalent and non-covalent grafted molecules were very similar to those of the FITC. Indeed, the XPS results showed that the surface of the DWNT-diamine-Cyanine sample presented only 51% of the total diamine that reacted with the Hemicarboxonium (precursor of the Cyanine), and again almost 50% of the grafted molecules that were weakly-bonded to the DWNTs. Similarly, the INS results brought evidences that the bulk of the sample was containing 25% of the total diamine available that reacted with Hemicarboxonium molecules to form the Cyanine ones, and around 50% of the total Hemicarboxonium simply adsorbed at the surface of the DWNTs. These latter results led us to conclude that the geometry of the compared fluorophores was unlikely to influence the efficiency of the covalent grafting process, at least in our experimental conditions.

In addition to the experimental results, and in order to go further in the understanding of this potential geometry influence, the FITC and the Cyanine were studied in terms of adsorption energy in presence of SWNTs, using DFT calculations. The performed calculations seemed to show that the adsorption energy of the two fluorophores were significantly different from one to another. Indeed, the performed calculations gave the E_{ads} of the FITC around -43 kcal.mol^{-1} while the E_{ads} of the Hemicarboxonium was given around -26 kcal.mol^{-1}, a difference that may be contradictory with the experimental results presented above.

In order to increase the general knowledge around the question of the competition between the covalent and non-covalent grafting of fluorophores onto DWNTs, further investigations would be required. First of all, as the comparison between the surface and the bulk of the samples suggests, the dispersion of the DWNTs during the grafting process may play a critical role

on the number of amine functions accessible to the fluorophore, and consequently on the quality of the covalent grafting. Mastering the dispersion of the DWNTs throughout the functionalization process could not only be an important parameter to ensure both the homogenization of the samples and the amount of covalently grafted fluorophores, but also could be an efficient way to improve the washing procedure aiming at removing the adsorbed molecules. Then it would be interesting to investigate the influence of the choice of the linker on the grafting process since some of our results suggests that in the absence of diamine, the removal of the adsorbed molecules is facilitated.

Finally, further simulations would be necessary to unveil the question of the apparent contradiction between the theoretical adsorption energies and the experimental results. Moreover, deeply investigating the different interactions of the fluorophores and the CNTs with the use of the DFT calculations could greatly assist the possible choice of an alternative fluorescent molecule, with a much lower adsorption energy, that would better suits the requirements of the fluorescence techniques related to toxicity studies.

Appendix A

Other Spectroscopic Techniques

In addition to the XPS and the INS techniques that were used in this project, some other spectroscopic techniques were explored as well. Indeed, with the help of Rozenn Le Parc and Jean-Louis Bantignies from the *Laboratoire Charles Coulomb (L2C)* in Montpellier, we could perform Raman and Infra-Red spectroscopy. Although these two techniques could not bring quantitative information about our samples, they allowed to obtain some qualitative information that strengthen our vision of the topic.

A.1 Raman spectroscopy

In order to obtain as much information as we could, we performed Raman spectroscopy using various excitation wavelengths. We were thus able to study our samples with 457, 488, 532, 633, 785 and 1064 nm excitation wavelengths, but only two of them could bring us exploitable results. Indeed, if the characteristic signature of the DWNTs were observed for every wavelength, only the 488 ant 1064 nm excitation wavelengths could give us information on the fluorophores. These results are presented hereafter.

Figure A.1, displays the Raman spectra obtained for the FITC and the Cyanine samples with a 1064 nm excitation wavelength rescaled in the range of 90-1250 cm^{-1} of interest (no signature beyond these limits).

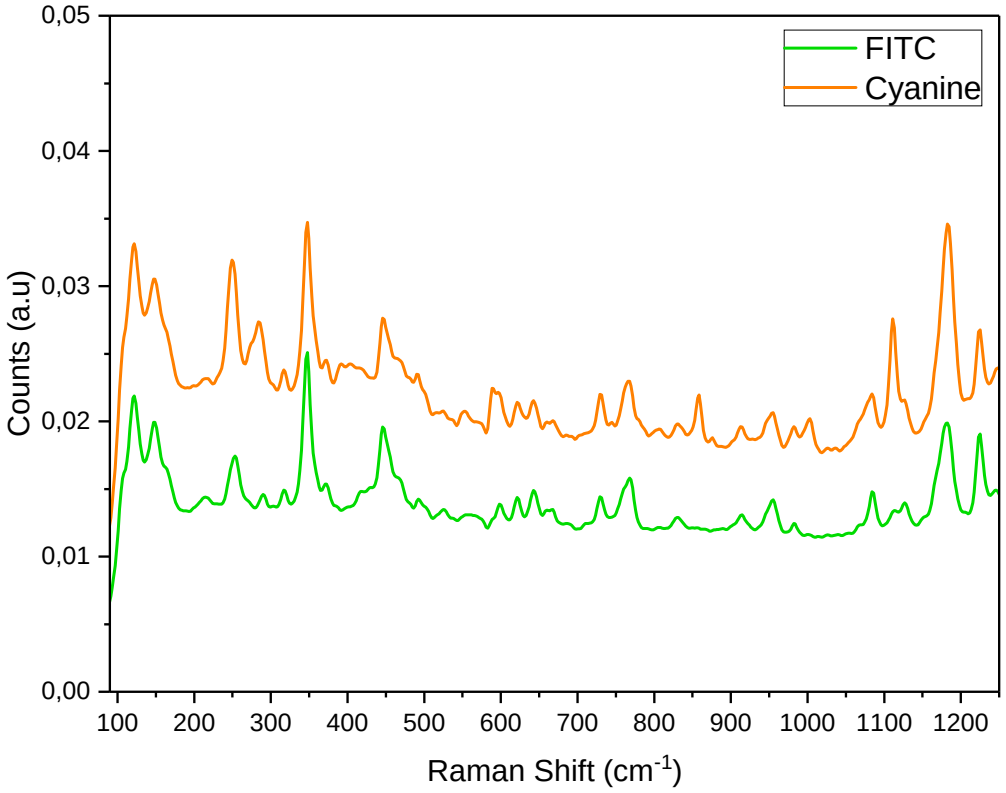

FIGURE A.1: *Raman spectra of the FITC and the Cyanine samples with a 1064 nm excitation wavelength. Results obtained with 250 mW power and 500 sec. accumulation time.*

The Raman response of the FITC (green line) and the Cyanine (orange line) samples for 1064 nm excitation wavelengths, showed on figure A.1, exhibits several vibrational modes, characteristic of the two organic fluophores and located between 90 and 1250 cm^{-1}. These characteristic modes were then used to evidence the presence of the fluorophores in our other samples at different excitation wavelength.

Figure A.2 shows the Raman spectra obtained for the DWNT-dble-ox (black line), DWNT-diamine (red line), DWNT-diamine-FITC (green line) and the DWNT@FITC (blue line) samples with a 488 nm excitation wavelength rescaled in the range of 90-1250 cm^{-1} of interest.

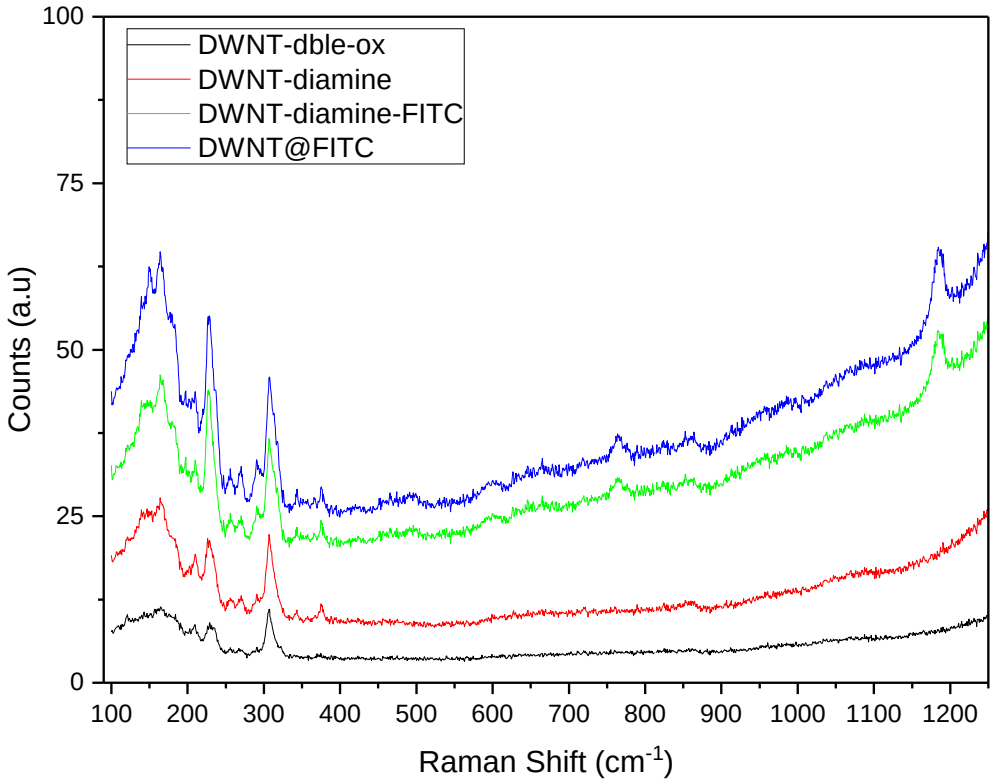

FIGURE A.2: *Raman spectra of the DWNT-dble-ox, DWNT-diamine, DWNT-diamine-FITC and the DWNT@FITC samples with a 488 nm excitation wavelength. Results obtained in 1 scan of 100 sec. accumulation time.*

By looking at figure A.2 we see that, besides the typical radial breathing modes (RBM) signatures of the DWNTs [204] clearly visible on the spectra of the DWNT-dble-ox and the DWNT-diamine samples in the range of 100-400 cm^{-1}, new vibrational modes arised between 400 and 1200 cm^{-1} when the FITC is added to the samples. Even if the intensity of this modes remained rather low, we distinguished few modes (490, 760 and 1185 cm^{-1}), also present in the Raman response of the FITC with a 1064 nm excitation wavelength (figureA.1), that confirmed the presence of the FITC in the DWNT-diamine-FITC and the DWNT@FITC samples.

Figure A.3 shows the Raman spectra obtained for the DWNT-dble-ox (black line), DWNT-diamine (red line), DWNT-diamine-Cyanine (green line) and

the DWNT@Cyanine (blue line) samples with a 488 nm excitation wavelength rescaled in the range of 90-1250 cm^{-1} of interest.

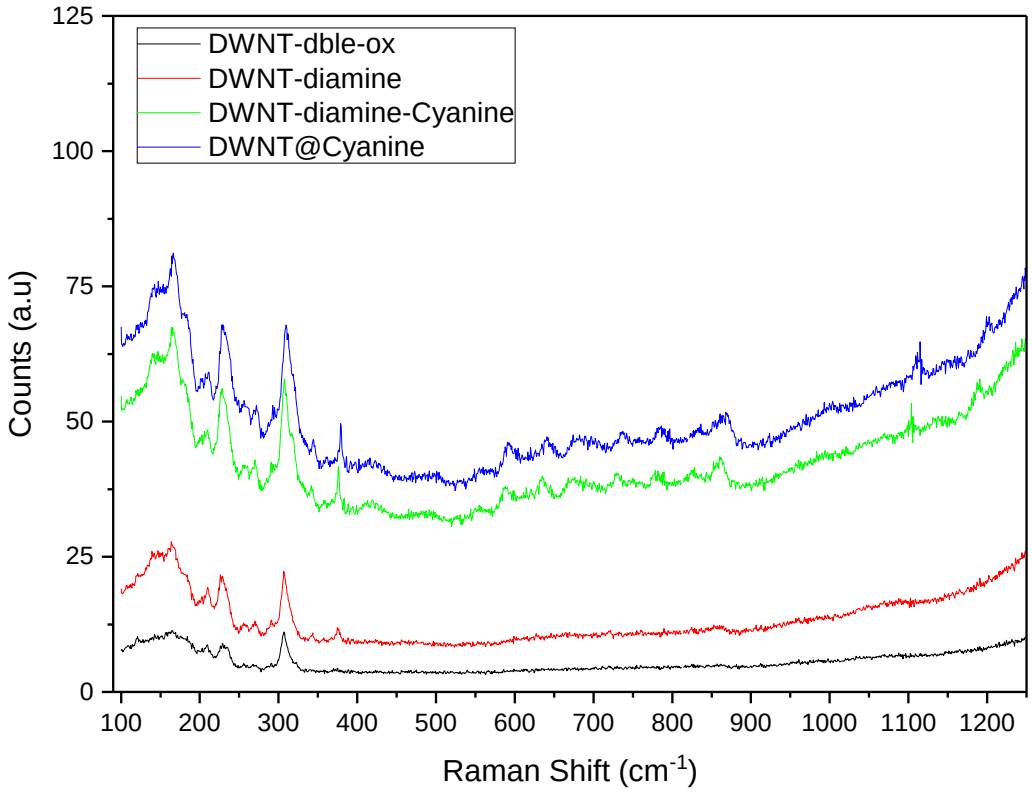

FIGURE A.3: *Raman spectra of the DWNT-dble-ox, DWNT-diamine, DWNT-diamine-Cyanine and the DWNT@Cyanine samples with a 488 nm excitation wavelength. Results obtained in 1 scan of 100 sec. accumulation time.*

Again, on figure A.3 we identified the typical radial breathing modes (RBM) signatures of the DWNTs [204] visible on the different spectra in the range of 100-400 cm^{-1}. Nevertheless, new vibrational modes arised as well between 400 and 1200 cm^{-1} when the cyanine is added to the samples. We can attribute the whole set of modes between 550 and 900 cm^{-1} and the modes at 1110 and 1200 cm^{-1} , also present in the Raman response of the Cyanine with a 1064 nm excitation wavelength (figureA.1) and again, confirmed the presence of the fluorescent molecule in the DWNT-diamine-Cyanine and the DWNT@Cyanine samples.

A.2 Infra-Red spectroscopy

The FITC-containing samples were also analyzed by means of Infra-Red (IR) spectroscopy. The samples been have prepared using the KBr tablet method. For each sample, 6 KBr tablets were prepared and were dried at 55°C for 24h in order to remove the water that easily absorb the IR wavelength. Every tablet was then left for 30 minutes in the primary vacuum of the IR spectrometer before to perform the measurements. The results presented below are a selection among the data collected in this survey and represent at best the whole set of results.

Figure A.4, shows the IR spectra in absorbance for the references Diamine-FITC (cyan line) and FITC (green line) samples, as well as for the DWNT-containing samples, DWNT-dble-ox (black line), DWNT-diamine (red line), DWNT-diamine-FITC (dark green line) and DWNT@FITC (blue line) samples.

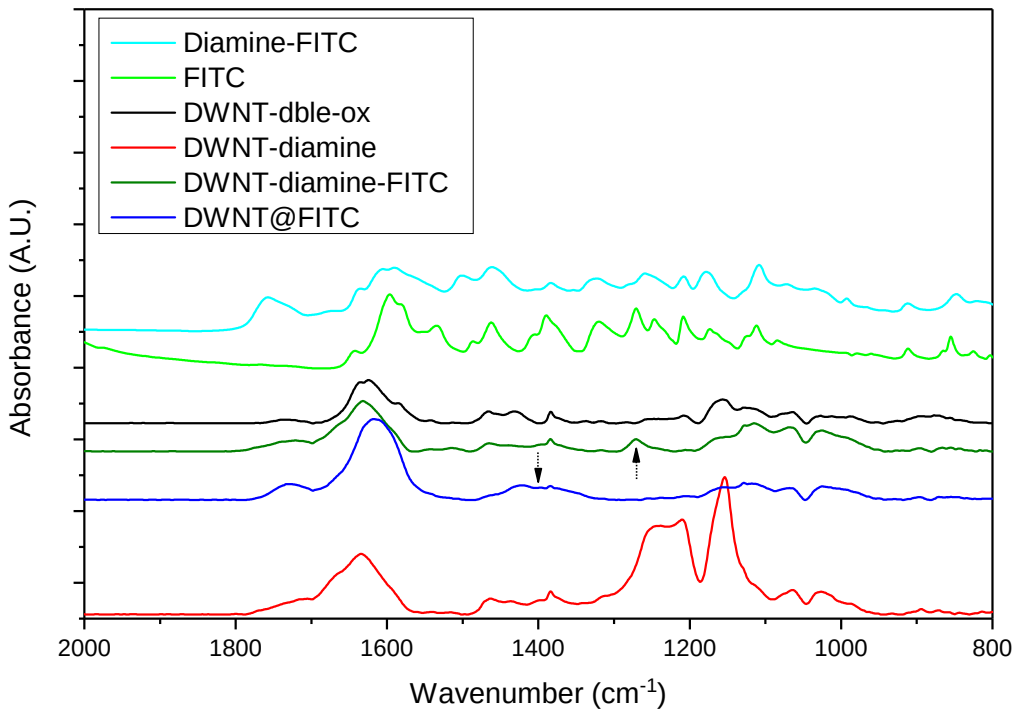

FIGURE A.4: *Infra-Red spectra of the Diamine-FITC, FITC, DWNT-dble-ox, DWNT-diamine, DWNT-diamine-FITC and DWNT@FITC samples in the low frequency range between 2000 and 800 cm^{-1}.*

Even if the vibrational bands observed on figure A.4 were of rather low intensities (absorbance around 0.001-0.005), some differences between the samples were visible. First of all, in the DWNT-diamine spectrum we observed a double set of vibrational bands around 1200 cm^{-1} and disappeared on the DWNT-diamine-FITC spectrum. This disappearance was associated to the grafting of the FITC onto the diamine during the functionalization process, and indicated us that the chemical reaction of the diamine with the FITC probably occured. Then, contrarily to what we would expect, the DWNT-diamine-FITC spectra appeared to be very similar to the one of the DWNT-dble-ox, while we would rather expect to see some signature of the reference Diamine-FITC, witnessing the covalent functionalization. Only a small vibrational band seemed to rise at 1270 cm^{-1} that could be attributed to an organic signature (arrow on the DWNT-diamine-FITC spectrum). Nevertheless, as the amount of organic molecules on the DWNTs is supposed to be very is very low, we wondered if this could explain the absence of covalent bonding signatures. Finally, we noticed for the DWNT@FITC that the vibrational band located around 1400 cm^{-1} appeared systematically wider than the other DWNT-containing samples (arrow on the DWNT@FITC spectrum), and might be the signature of the FITC adsorbed on the carbon nanotubes.

Appendix B

Multiphonon scattering

B.1 Multiphonon Scattering in Neutron Spectra

It has been shown in the chapter 2.2.2 that the neutrons interacts with atoms by giving a quantum of energy corresponding to the energy needed for creating or annealing a phonon. This is actually an approximation of what happen in reality, and the way neutrons interacts with matter is much more complex. Indeed, even if the one-phonon scattering mentioned above is a type of event statistically very likely to happen, it is not sufficient as a model for the correct description of the experimental INS Spectra. For example, Figure B.1 illustrate perfectly this fact. It shows what a calculated Density of States (DOS) would look like if the one-phonon process only would be taken into account.

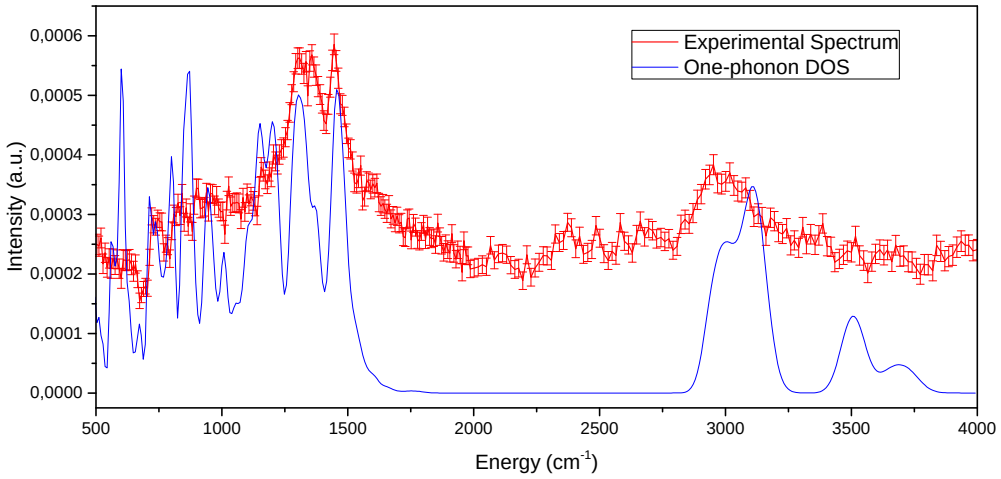

FIGURE B.1: *Experimental Spectrum of DWNT-diamine-FITC sample and comparison with its one-phonon DOS from DFT calculations*

We can clearly see that this one-phonon model cannot explain entirely the experimental results. For instance, if we trust the calculated one-phonon DOS, the whole vibrational range in between 1500 and 2750 cm^{-1} should not present any vibrational band, nevertheless it is clearly not the case according to our experimental data. Also, the experimental data seem to show the presence of noticeable vibrations at 1600 cm^{-1} and 3300 cm^{-1} which is in total contradiction with our calculated DOS.

In order to go further in the understanding of the experimental INS spectra, it is then necessary to introduce the Multiphonon Scattering. It occurs when a neutron scatters from an atom and gives more than a single quantum of energy. It is very important to pay attention to the fact that "Multiphonon Scattering" is a generic term that is used to describe different types of event and that there is often a confusion made in between this different sub-events. Indeed, this generic term regroups three different type of event: Overtones, Combinations and Phonon Wings [205]. Those events all lead to a multiple quantum of energy loss for the neutron, but the mechanisms involved and

their consequences are very different.

B.1.1 Overtones

The overtones are the results of the multiple excitation of **the same vibration**, which means that a neutron will interact with an atom by depositing N times the energy of the fundamental vibration (where N is an integer). When this neutron is detected it owns N times less energy than it should have and is interpreted exactly like if it has excited a different vibration with N times more energy than the fundamental one. (See figureB.2)

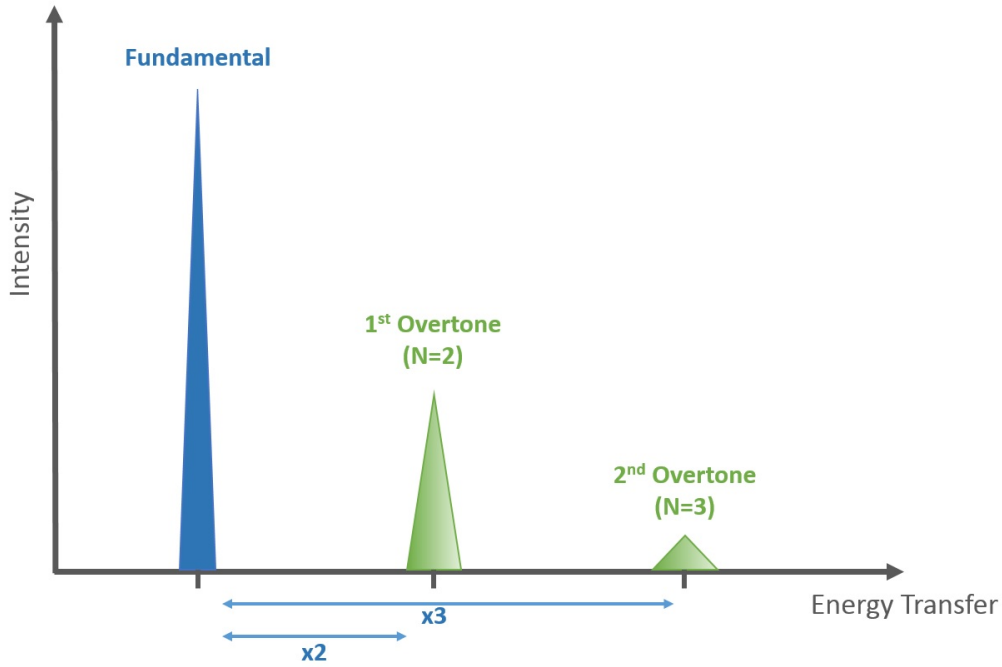

FIGURE B.2: *Schematic representation of the consequences of the Overtones events on INS spectra*

B.1.2 Combinations

The combinations correspond to the single excitation of **more than one vibration**. A neutron will interact with an atom exciting the fundamental vibration, but will have sufficient energy to excite other fundamental vibrations, either for the same atom or for different ones. Like for the overtones, when

it comes to the neutron detection, the latter has lost the sum of the energy of the fundamental vibrations exited on its way. It is then interpreted as a new vibration instead of the combination of several fundamental ones. Nevertheless, as there is obviously many combinations possible in between many fundamental modes, the result of these events on the experimental spectra is comparable to a background, increasing with the energy transfer. (See figure B.3)

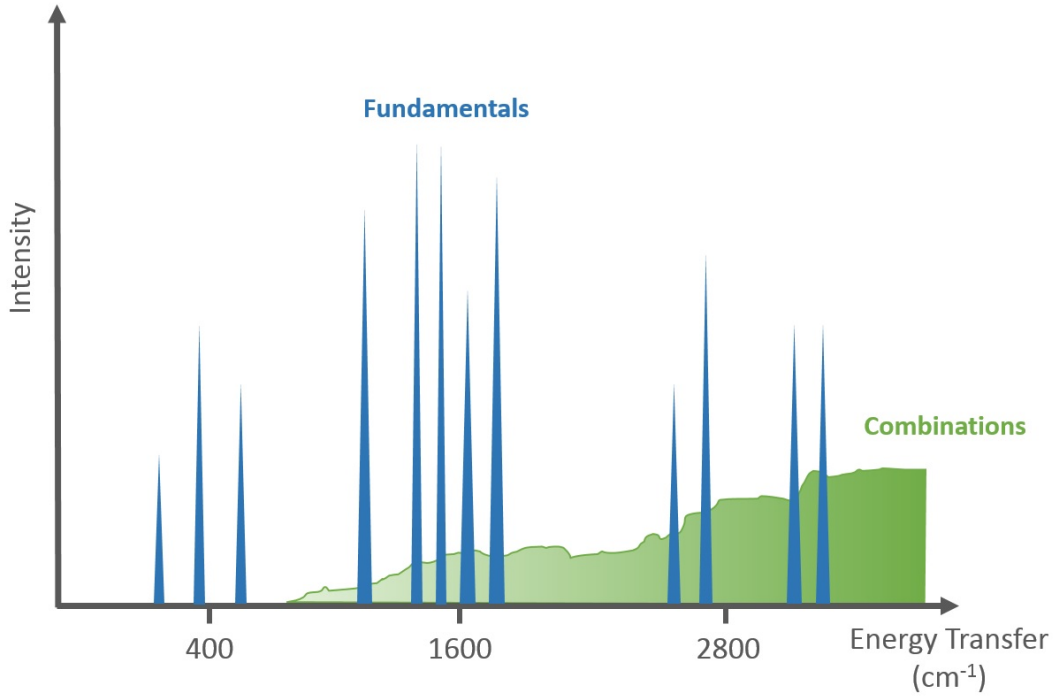

FIGURE B.3: *Schematic representation of the consequences of the Combinations events on INS spectra*

B.1.3 Phonon Wings

Finally, the Phonon wings are the result of the excitation of **an external-mode as well as the internal-mode** of interest. They are always present in INS spectra, in that sense they cannot be neglected for a full understanding of the experimental data. Phonon wings occurs when a neutron interact with the fundamental vibration of an internal-mode and have sufficient energy to interact with an external-mode as well. As the excitation of an external-mode

requires a small amount of energy, the neutrons responsible for the wings are always detected relatively close to their internal-mode fundamental origin. (See figure B.4)

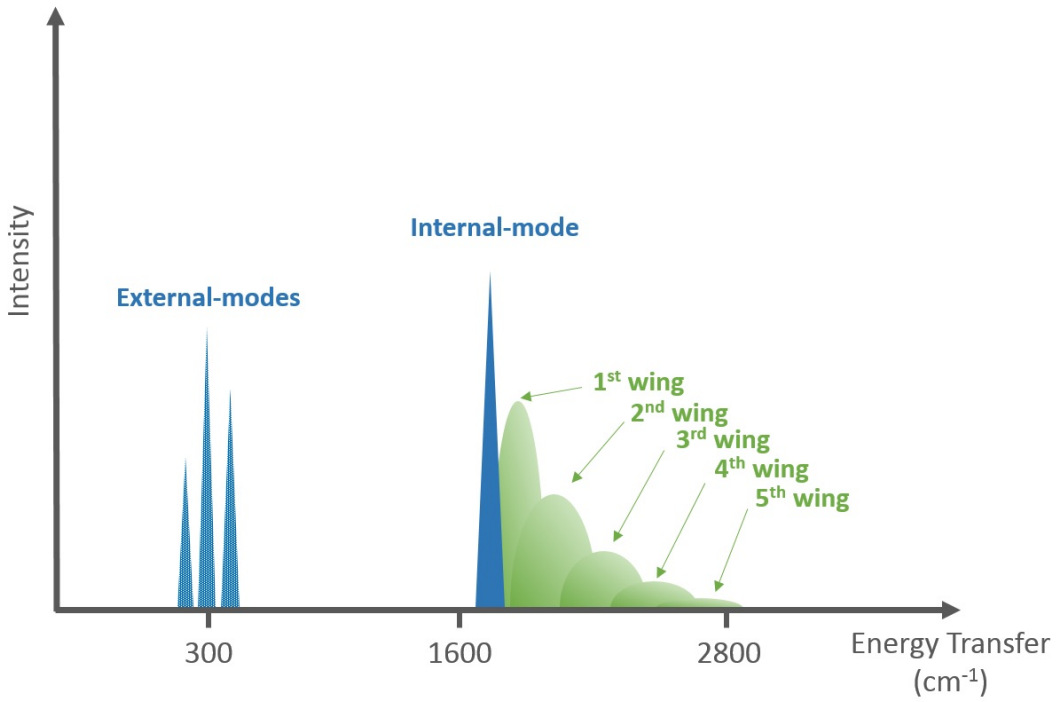

FIGURE B.4: *Schematic representation of the consequences of the Phonon Wings events on INS spectra*

The Phonon wings strength depends on many factors but the way the intensity is shared in between the fundamental internal mode (parent peak) [206, 207] and its wings is driven by the following equation:

$$I_t = \sum_n \frac{(Q^2 U_{ext}^2)^n}{n!} \exp\left(-Q^2 U_{ext}^2\right) \tag{B.1}$$

Where I_t is the total internal-mode intensity (one-phonon process), Q is the momentum-transfer factor, U_{ext} is the mean-square displacement of the external-modes and n is the phonon wings order. Note that $n = 0$ corresponds to the resultant intensity of the parent peak.

In practice, it is necessary to start with the generation of the individual shapes of the phonon wings [207]. The usual way to do it, consists in the convolution of the one-phonon external-modes DOS with itself the appropriate number of time, such as:

$$S_1(Q,\omega_{ext}) = S_0(Q,\omega_{ext}) \otimes S_0(Q,\omega_{ext})$$

$$S_2(Q,\omega_{ext}) = S_1(Q,\omega_{ext}) \otimes S_0(Q,\omega_{ext})$$

$$\dots$$

$$S_n(Q,\omega_{ext}) = S_{n-1}(Q,\omega_{ext}) \otimes S_0(Q,\omega_{ext}) \tag{B.2}$$

Where $S_n(Q,\omega_{ext})$ is the shape of the n-order phonon wing. Note that $n = 0$ corresponds to the one-phonon external-modes DOS.

These shapes are then stored and normalized. Finally, they can be combined in the appropriate ratios resulting from Eq.B.1 in order to generate the correct wing for each internal-mode. (In the case of spectrometers that scan with Q^2 proportional to the energy transfer, the relative proportion of each wing needs to be generated for each frequency.)

B.2 Application to the calculated DOS

Accordingly to the effects of the different multiphonon events presented above, the characteristic vibrational band associated to the presence of -NH_2 groups at 1600 cm^{-1} that we intend to fit in order to be able to extract quantitative information about the grafting efficiency of our process, seem to be hidden by phonon wings contributions to the spectrum in the 1500-2750 cm^{-1} region. Two different approaches have been used in this project to take into account

the phonon wings, the first one, extensively developed by Kearley and Tomkinson [205–208], lays on the very basic definition of the phonon wings and allows to simulate the influence of the external modes on specific internal modes. This method is generally very accurate to simulate the effect of the phonon wings on few vibrational bands but became hard to compute for all the modes present in a spectrum and does not take into account the effects of overtones and combinations. Another approach was develloped by Dawidowski [201, 202, 209], this method based on the auto-convolution of the calculated one-phonon DOS, allows to take into account all the contributions to the multiphonon events, is very easy to operate but is less accurate than the previous one. The phonon wings contributions to this region were thus calculated from the calculated DOS with the two methods in order to discriminate the vibrational band of interest and the multiphonon contributions. We first made the calculations with the 1st very accurate method for few vibrational bands of interest and then used the 2nd less accurate method to obtain better representations of the whole spectra. As the results we obtained with both methods were relatively similar, we kept the results of the 2nd method that represent best the experimental data on the whole measured spectral range.

B.2.1 Method 1 : The Kearley's approach

Phonon Wings shapes

Figure B.5 shows the first step of the phonon wing generation for the two main sample calculated DOS, DWNT-diamine and DWNT-diamine-FITC. The different wings have been generated by the convolution method described by Eq. B.2, and have been individually normalized and stored. This figure illustrate the fact that, both the shape and the relative positions of the different wings, is strongly influenced by the external-modes of the samples.

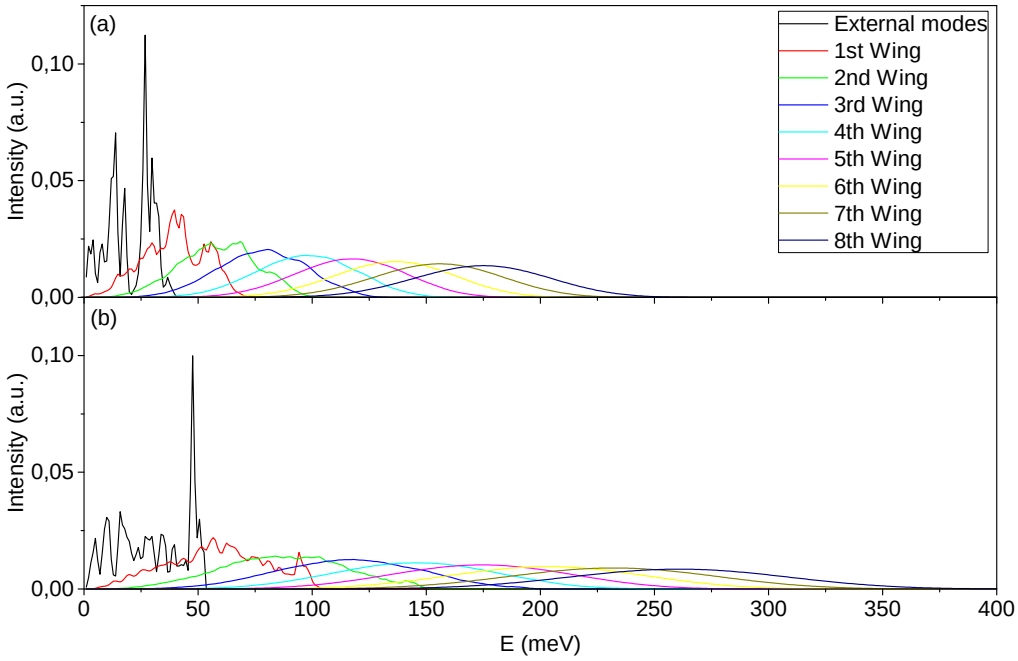

FIGURE B.5: *Comparison of the external-modes and their consequences on the shapes of the generated Phonon Wings for (a) the DWNT-diamine and (b) the DWNT-diamine-FITC samples*

Indeed, we see that the external-modes are very different for the two samples. It has a direct impact on the resulting wings since, for instance, the first-order wing (red line) generated from the DWNT-diamine external-modes presents two relatively well-defined peaks, while the first-order wing of the DWNT-diamine-FITC is rather smooth and much closer to a Gaussian-like type of shape.

Phonon Wings generation for different frequencies

Now the Phonon Wings shapes have been generated, it is required to calculate their relative individual proportion for each fundamental vibration. In order to simplify the understanding of the wings' influence, we first calculated their relative intensity using Eq.B.1 for few picked frequencies in the bending region and for two different samples. We chose to generate

the wings respectively for the fundamentals at 1128, 1192, 1312, 1448 and 1624 cm^{-1} for the DWNT-diamine, and at 1160, 1224, 1336 and 1488 cm^{-1} for the DWNT-diamine-FITC. Once the intensity of each wing have been determined for each frequency, they are shifted to their correct position. To do so, the distance of the eight wings from the center of mass of the external-modes is determined. Then, the relative eight first wings are placed so that their distance from each chosen fundamental internal-mode frequency corresponds to their distance from their original external-modes center of mass. Finally, they are summed and are added to the calculated DOS obtained with the help of DFT calculations.

Figure B.6 shows how the external-modes can drastically influence the experimental spectra through the Phonon Wings event. It compares the two cases obtained in our calculations for the grafting process. Figure B.6-a displays, for the case where 0 % of the FITC has been grafted : the DOS obtained by DFT calculations for the one-phonon process (Yellow line), the sum of the generated Phonon Wings for the frequencies mentioned above (Green line), the sum of the one-phonon DOS and the Phonon Wings covoluted with the experimental resolution (Blue line), and compares it with the experimental spectra of the DWNT-diamine sample (Red line). Figure B.6-b provides the same information but for the other case, where 25% of the diamine reacted with the FITC, and compares it with the experimental spectra of the DWNT-diamine-FITC sample.

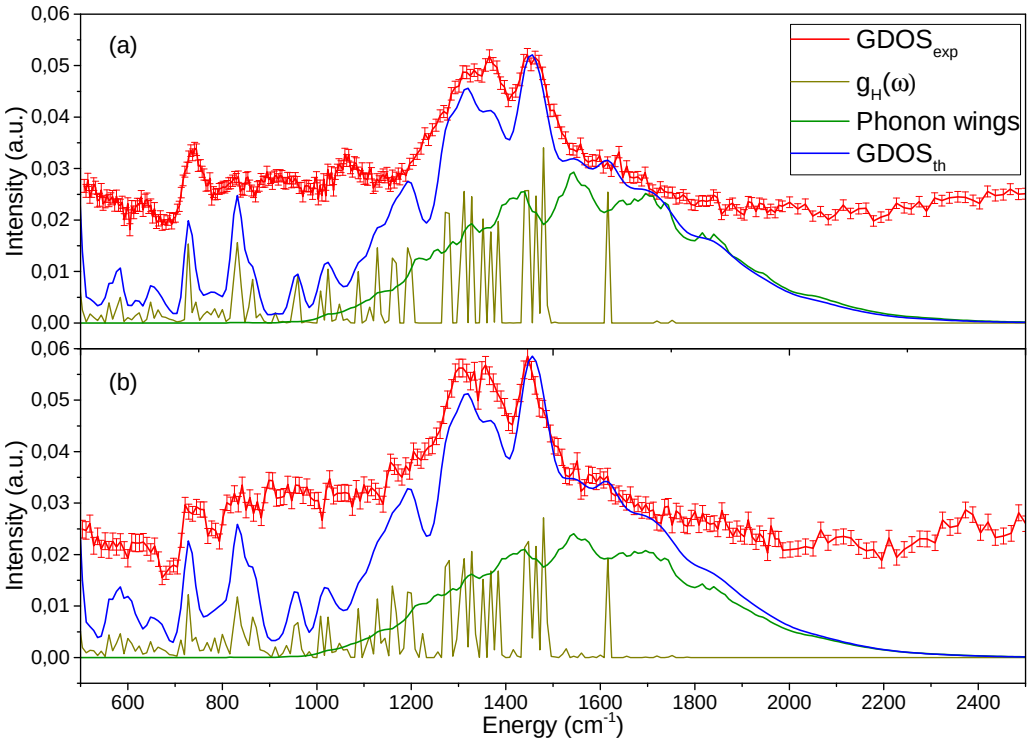

FIGURE B.6: *Comparison of resulting Phonon Wings and their influence on the calculated DOS with the experimental spectra in the bending region for (a) the DWNT-diamine and (b) the DWNT-diamine-FITC samples*

The Kearly's approach helped understanding why the two spectra on figure B.6 seem to be very similar even if the characteristic band of the -NH_2 was supposed to be strongly affected by the grafting of FITC. Indeed we clearly see that the vibrational band of interest at 1600 cm^{-1} is affected by the grafting of the FITC, but the decrease of this band is compensated by the phonon wings, resulting in a similar GDOS$_{th}$ on both spectra.

B.2.2 Method 2 : The Dawidowski's approach

This method, less accurate than the previous one, presents the advantage of being very easy to operate. Furthermore, it showed relatively similar results than the Kearley's approach in terms of phonon wings but taking into account the other multiphonon contributions.

In practice, it consists simply in the convolution of the whole one-phonon DOS with itself the appropriate number of time, such as:

$$S_1(Q,\omega) = S_0(Q,\omega) \otimes S_0(Q,\omega)$$

$$S_2(Q,\omega) = S_1(Q,\omega) \otimes S_0(Q,\omega)$$

$$\dots$$

$$S_n(Q,\omega) = S_{n-1}(Q,\omega) \otimes S_0(Q,\omega) \tag{B.3}$$

Where $S_n(Q,\omega)$ is the n-order multiphonon contribution to the spectra. Note that $n = 0$ corresponds to the one-phonon DOS. The different contribution orders are finally simply summed.

In our calculation of the multiphonon contributions, we took into account the contributions up to the 5^{th} order, and obtained the results presented in the chapter 3.1.2 and on figure B.7 below. The one-phonon DOS presented here are the same as fo the Kearley's approach, *i.e.* one model where 0% of diamine reacted with the FITC (figure B.7-a) and one model where 25% of the diamine reacted with the FITC (figure B.7-b).

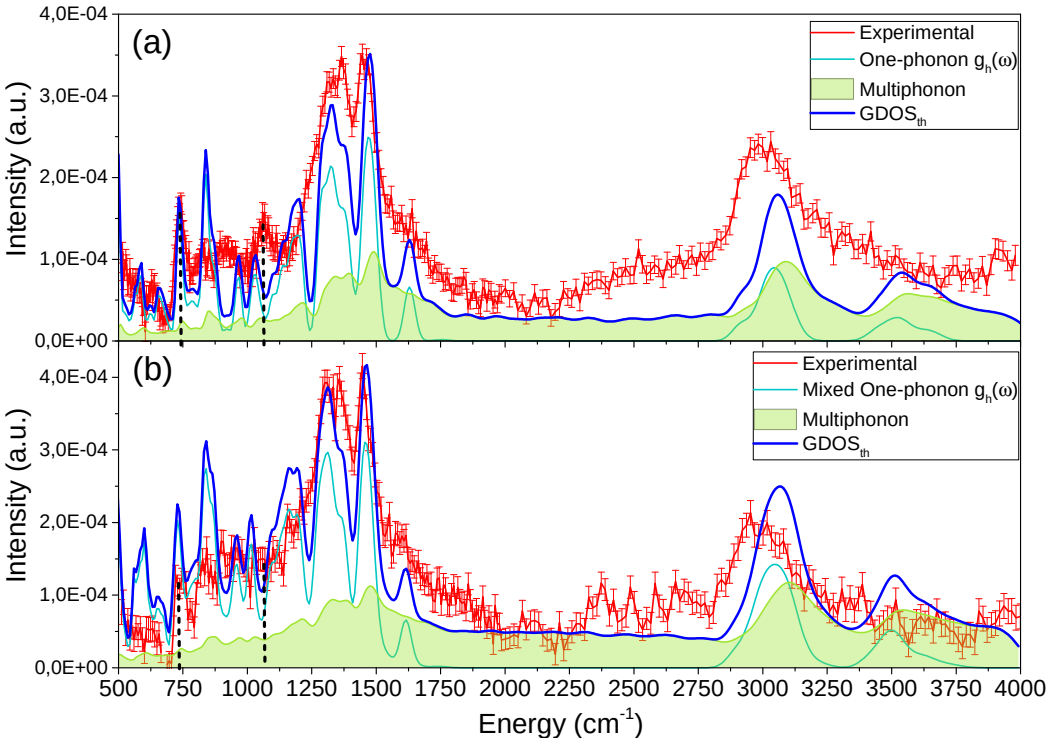

FIGURE B.7: *Comparison of resulting multiphonon contributions and their influence on the calculated DOS with the experimental spectra for (a) the DWNT-diamine and (b) the DWNT-diamine-FITC samples*

We see on figure B.7 that even if the phonon wings in the range of 1200-2000 cm^{-1} are less accurate than our results with the method 1, the resulting effect on the spectra are relatively similar. Indeed at 1600 cm^{-1}, we see that the effect of the phonon wings contributions compensate once again the intensity loss of the vibrational band of interest. Furthermore, we see that for the energy ranges of 500-1000 and 1750-2750 cm^{-1} the "background" resulting from the combination events is quite well described and reproduce best the measurements performed by means of INS spectroscopy.

Bibliography

1. Peiyan, M, Zhengyi, F, Yanli, S & al. The nano pulverization of traditional Chinese medicine Liuwei Dihuang. *Mat. Sci.* **21,** 105–108 (2006).
2. Jose-Yacaman, M, Rendon, L, Arenas, J & al. Maya blue paint: An ancient nanostructured material. *Science* **273,** 223–225 (1996).
3. Padeletti, G. & Fermo, P. How the masters in Umbria, Italy, generated and used nanoparticles in art fabrication during the Renaissance period. *Applied Physics A: Materials Science & Processing* **76,** 515–525 (Mar. 2003).
4. Freestone, I., Meeks, N., Sax, M. & Higgitt, C. The Lycurgus Cup - A Roman nanotechnology. *Gold Bulletin* **40,** 270–277 (2007).
5. Reibold, M. *et al.* Materials: Carbon nanotubes in an ancient Damascus sabre. *Nature* **444,** 286–286 (Nov. 2006).
6. Feynman, R. P. There is Plenty of Room at the Bottom (transcript talk). *Engineering and Science.* Transcripted talk. (2016) (1960).
7. Kroto, H. W., Heath, J. R., O'brien, S. C., Curl, R. F. & Smalley, R. E. C60: Buckminsterfullerene. *Nature* **318,** 162–163 (Nov. 1985).
8. Haug, H. & Koch, S. W. *Quantum Theory of the Optical and Electronic Properties of Semiconductors* Fifth Edition (World Scientific, 2009).
9. Olk, C. H. & Heremans, J. P. Scanning tunneling spectroscopy of carbon nanotubes. en. *Journal of Materials Research* **9,** 259–262 (Feb. 1994).
10. Vajtai, R. *Springer Handbook of Nanomaterials* (Springer Science & Business Media, Aug. 2013).

11. Coleman, J. N., Khan, U., Blau, W. J. & Gun'ko, Y. K. Small but strong: A review of the mechanical properties of carbon nanotube–polymer composites. en. *Carbon* **44,** 1624–1652 (Aug. 2006).

12. Guiderdoni, C. *et al.* The preparation of carbon nanotube (CNT)/copper composites and the effect of the number of CNT walls on their hardness, friction and wear properties. en. *Carbon* **58,** 185–197 (July 2013).

13. Ahmad, K. & Pan, W. Microstructure-toughening relation in alumina based multiwall carbon nanotube ceramic composites. en. *Journal of the European Ceramic Society* **35,** 663–671 (Feb. 2015).

14. Chen, T. *et al.* Aptamer-conjugated nanomaterials for bioanalysis and biotechnology applications. en. *Nanoscale* **3,** 546–556 (2011).

15. Biju, V. Chemical modifications and bioconjugate reactions of nanomaterials for sensing, imaging, drug delivery and therapy. en. *Chem. Soc. Rev.* **43,** 744–764 (2014).

16. Webster, D. M., Sundaram, P. & Byrne, M. E. Injectable nanomaterials for drug delivery: Carriers, targeting moieties, and therapeutics. en. *European Journal of Pharmaceutics and Biopharmaceutics* **84,** 1–20 (May 2013).

17. Yang, Y. *et al.* Advances in self-assembled chitosan nanomaterials for drug delivery. en. *Biotechnology Advances* **32,** 1301–1316 (Nov. 2014).

18. Goenka, S., Sant, V. & Sant, S. Graphene-based nanomaterials for drug delivery and tissue engineering. en. *Journal of Controlled Release* **173,** 75–88 (Jan. 2014).

19. Pumera, M. Graphene-based nanomaterials for energy storage. en. *Energy Environ. Sci.* **4,** 668–674 (2011).

20. Callini, E. *et al.* Nanostructured materials for solid-state hydrogen storage: A review of the achievement of COST Action MP1103. en. *International Journal of Hydrogen Energy* **41,** 14404–14428 (Aug. 2016).

21. Zhao, X., Sánchez, B. M., Dobson, P. J. & Grant, P. S. The role of nanomaterials in redox-based supercapacitors for next generation energy storage devices. en. *Nanoscale* **3,** 839 (2011).

22. Wang, L., Quadir, M. & Aguey-Zinsou, K.-F. Ni coated LiH nanoparticles for reversible hydrogen storage. en. *International Journal of Hydrogen Energy* **41,** 6376–6386 (Apr. 2016).

23. Liu, W. & Aguey-Zinsou, K.-F. Synthesis of highly dispersed nanosized LaNi5 on carbon: Revisiting particle size effects on hydrogen storage properties. en. *International Journal of Hydrogen Energy* **41,** 14429–14436 (Aug. 2016).

24. Krauss, P. R. & Chou, S. Y. Nano-compact disks with 400 Gbit/in2 storage density fabricated using nanoimprint lithography and read with proximal probe. en. *Applied Physics Letters* **71,** 3174–3176 (Nov. 1997).

25. Georgiou, T. *et al.* Vertical field-effect transistor based on graphene-WS2 heterostructures for flexible and transparent electronics. *Nat Nano* **8,** 100–103 (Feb. 2013).

26. Lee, G.-H. *et al.* Flexible and Transparent MoS $_2$ Field-Effect Transistors on Hexagonal Boron Nitride-Graphene Heterostructures. en. *ACS Nano* **7,** 7931–7936 (Sept. 2013).

27. Jang, S., Kim, S., Geier, M. L., Hersam, M. C. & Dodabalapur, A. Inkjet printed carbon nanotubes in short channel field effect transistors: influence of nanotube distortion and gate insulator interface modification. *Flexible and Printed Electronics* **1,** 035001 (Sept. 2016).

28. Rother, M., Schießl, S. P., Zakharko, Y., Gannott, F. & Zaumseil, J. Understanding Charge Transport in Mixed Networks of Semiconducting Carbon Nanotubes. en. *ACS Applied Materials & Interfaces* **8,** 5571–5579 (Mar. 2016).

29. Vidor, F. F., Meyers, T., Wirth, G. I. & Hilleringmann, U. ZnO nanoparticle thin-film transistors on flexible substrate using spray-coating technique. en. *Microelectronic Engineering* **159,** 155–158 (June 2016).

30. Datsyuk, V. *et al.* Double-walled carbon nanotube dispersion via surfactant substitution. en. *Journal of Materials Chemistry* **19,** 2729 (2009).

31. Utsumi, S. *et al.* RBM band shift-evidenced dispersion mechanism of single-wall carbon nanotube bundles with NaDDBS. en. *Journal of Colloid and Interface Science* **308,** 276–284 (Apr. 2007).

32. Hobbie, E. K. *et al.* Self-Assembly of Ordered Nanowires in Biological Suspensions of Single-Wall Carbon Nanotubes. en. *ACS Nano* **3,** 189–196 (Jan. 2009).

33. Ernst, F., Heek, T., Setaro, A., Haag, R. & Reich, S. Functional Surfactants for Carbon Nanotubes: Effects of Design. en. *The Journal of Physical Chemistry C* **117,** 1157–1162 (Jan. 2013).

34. Graf, C. *et al.* Surface Functionalization of Silica Nanoparticles Supports Colloidal Stability in Physiological Media and Facilitates Internalization in Cells. en. *Langmuir* **28,** 7598–7613 (May 2012).

35. Ding, X., Zhao, J., Liu, Y., Zhang, H. & Wang, Z. Silica nanoparticles encapsulated by polystyrene via surface grafting and in situ emulsion polymerization. en. *Materials Letters* **58,** 3126–3130 (Oct. 2004).

36. Viswanathan, G. *et al.* Single-step in situ synthesis of polymer-grafted single-wall nanotube composites. *Journal of the American Chemical Society* **125,** 9258–9259 (2003).

37. Xiong, J., Zhou, D., Zheng, Z., Yang, X. & Wang, X. Fabrication and distribution characteristics of polyurethane/single-walled carbon nanotube composite with anisotropic structure. en. *Polymer* **47,** 1763–1766 (Mar. 2006).

38. He, Y. *et al.* Surface functionalized carbon nanotubes and its effects on the mechanical properties of epoxy based composites at cryogenic temperature. en. *Polymer Bulletin* **71,** 2465–2485 (Oct. 2014).

39. Wang, K., Li, N., Ren, K., Zhang, Q. & Fu, Q. Exploring interfacial enhancement in polystyrene/multiwalled carbon nanotube monofilament induced by stretching. en. *Composites Part A: Applied Science and Manufacturing* **61,** 84–90 (June 2014).

40. Kolmakov, A., Klenov, D. O., Lilach, Y., Stemmer, S. & Moskovits, M. Enhanced Gas Sensing by Individual SnO_2 Nanowires and Nanobelts Functionalized with Pd Catalyst Particles. en. *Nano Letters* **5,** 667–673 (Apr. 2005).

41. Del Carmen Giménez-López, M. *et al.* Encapsulation of single-molecule magnets in carbon nanotubes. *Nature Communications* **2,** 407 (July 2011).

42. *Consumer Products • Topics • Nanotechnology Project* http://nanotechproject.org/topics/consumer_products/ (2017).

43. Afsset. *Les nanomatériaux : effets sur la santé de l'homme et sur l'environnement* Avis (2006). (2017).

44. World Health Organization. *Parma Declaration on Environment and Health, Fifth Ministerial Conference on Environment and Health "Protecting children's health in a changing environment"* Declaration (2010). (2017).

45. Anses. *Enjeux et mise à jour des connaissances* Avis (2014). (2017).

46. Hankin, S. M. *et al. Specific advice on fulfilling information requirements for nanomaterials under REACH (RIP-oN 2)–Final project report* tech. rep. (European Commission, 2011). (2017).

47. Aitken, R. A. *et al. Specific Advice on Exposure Assessment and Hazard/Risk Characterisation for Nanomaterials under REACH (RIP-oN 3)-Final Project Report* tech. rep. (European Commission, 2011). (2017).

48. Ellsworth, D. K., Verhulst, D., Spitler, T. M. & Sabacky, B. J. Titanium nanoparticles move to the marketplace. *Chemical innovation* **30,** 30–35 (2000).

49. Wold, A. Photocatalytic properties of titanium dioxide (TiO2). *Chemistry of Materials* **5,** 280–283 (1993).

50. Bettini, S. *et al.* Food-grade TiO2 impairs intestinal and systemic immune homeostasis, initiates preneoplastic lesions and promotes aberrant crypt development in the rat colon. *Scientific Reports* **7,** 40373 (Jan. 2017).

51. Weir, A., Westerhoff, P., Fabricius, L., Hristovski, K. & von Goetz, N. Titanium Dioxide Nanoparticles in Food and Personal Care Products. en. *Environmental Science & Technology* **46,** 2242–2250 (Feb. 2012).

52. DUSSERT, A.-S., Gooris, E. & Hemmerle, J. Characterization of the mineral content of a physical sunscreen emulsion and its distribution onto human stratum corneum. *International journal of cosmetic science* **19,** 119–129 (1997).

53. Sadrieh, N. *et al.* Lack of Significant Dermal Penetration of Titanium Dioxide from Sunscreen Formulations Containing Nano- and Submicron-Size TiO2 Particles. en. *Toxicological Sciences* **115,** 156–166 (May 2010).

54. Warheit, D. B., Webb, T. R., Reed, K. L., Frerichs, S. & Sayes, C. M. Pulmonary toxicity study in rats with three forms of ultrafine-TiO2 particles: Differential responses related to surface properties. en. *Toxicology* **230,** 90–104 (Jan. 2007).

55. Wang, J *et al.* Acute toxicity and biodistribution of different sized titanium dioxide particles in mice after oral administration. en. *Toxicology Letters* **168,** 176–185 (Jan. 2007).

56. Bermudez, E. *et al.* Pulmonary Responses of Mice, Rats, and Hamsters to Subchronic Inhalation of Ultrafine Titanium Dioxide Particles. *Toxicological Sciences* **77,** 347–357 (2004).

57. Jani, P. U., McCarthy, D. E. & Florence, A. T. Titanium dioxide (rutile) particle uptake from the rat GI tract and translocation to systemic organs after oral administration. *International Journal of Pharmaceutics* **105,** 157 –168 (1994).

58. Long, T. C., Saleh, N., Tilton, R. D., Lowry, G. V. & Veronesi, B. Titanium Dioxide (P25) Produces Reactive Oxygen Species in Immortalized Brain Microglia (BV2): Implications for Nanoparticle Neurotoxicity †. en. *Environmental Science & Technology* **40,** 4346–4352 (July 2006).

59. Hund-Rinke, K. & Simon, M. Ecotoxic Effect of Photocatalytic Active Nanoparticles (TiO2) on Algae and Daphnids (8 pp). en. *Environmental Science and Pollution Research - International* **13,** 225–232 (July 2006).

60. Dubey, A., Goswami, M., Yadav, K. & Chaudhary, D. Oxidative Stress and Nano-Toxicity Induced by TiO2 and ZnO on WAG Cell Line. en. *PLOS ONE* **10** (ed Yang, W.-X.) e0127493 (May 2015).

61. Vevers, W. F. & Jha, A. N. Genotoxic and cytotoxic potential of titanium dioxide (TiO2) nanoparticles on fish cells in vitro. en. *Ecotoxicology* **17,** 410–420 (July 2008).

62. Fabian, E. *et al.* Tissue distribution and toxicity of intravenously administered titanium dioxide nanoparticles in rats. en. *Archives of Toxicology* **82,** 151–157 (Mar. 2008).

63. Miller, R. J. *et al.* Impacts of Metal Oxide Nanoparticles on Marine Phytoplankton. en. *Environmental Science & Technology* **44,** 7329–7334 (Oct. 2010).

64. Gurr, J.-R., Wang, A. S., Chen, C.-H. & Jan, K.-Y. Ultrafine titanium dioxide particles in the absence of photoactivation can induce oxidative damage to human bronchial epithelial cells. en. *Toxicology* **213,** 66–73 (Sept. 2005).

65. Renwick, L. C. Increased inflammation and altered macrophage chemotactic responses caused by two ultrafine particle types. en. *Occupational and Environmental Medicine* **61,** 442–447 (May 2004).

66. Grassian, V. H., O'Shaughnessy, P. T., Adamcakova-Dodd, A., Pettibone, J. M. & Thorne, P. S. Inhalation Exposure Study of Titanium Dioxide Nanoparticles with a Primary Particle Size of 2 to 5 nm. en. *Environmental Health Perspectives* **115,** 397–402 (Dec. 2006).

67. Warheit, D. B. Pulmonary Instillation Studies with Nanoscale TiO2 Rods and Dots in Rats: Toxicity Is not Dependent upon Particle Size and Surface Area. en. *Toxicological Sciences* **91,** 227–236 (Feb. 2006).

68. Sayes, C. M. Correlating Nanoscale Titania Structure with Toxicity: A Cytotoxicity and Inflammatory Response Study with Human Dermal Fibroblasts and Human Lung Epithelial Cells. en. *Toxicological Sciences* **92,** 174–185 (Mar. 2006).

69. Braydich-Stolle, L. K. *et al.* Crystal structure mediates mode of cell death in TiO2 nanotoxicity. en. *Journal of Nanoparticle Research* **11,** 1361–1374 (Aug. 2009).

70. Jorio, A. & Dresselhaus, G. *Carbon Nanotubes : Advanced Topics in the Synthesis, Structure, Properties and Applications* (2015) (Springer Science & Business Media, 2001).

71. Iijima, S. Helical microtubules of graphitic carbon. *nature* **354,** 56 (1991).

72. Bethune, D. *et al.* Cobalt-catalysed growth of carbon nanotubes with single-atomic-layer walls. *Nature* **363,** 605–607 (1993).

73. Lijima, S. & Ichihashi, T. Single-shell carbon nanotubes of 1-nm diameter. *Nature* **364,** 737 (1993).

74. Wildoer, J. W., Venema, L. C., Rinzler, A. G., Smalley, R. E. & Dekker, C. Electronic structure of atomically resolved carbon nanotubes. *Nature* **391,** 59 (1998).

75. Odom, T. W., Jin-Lin, H., Kim, P. & Lieber, C. M. Atomic structure and electronic properties of single-walled carbon nanotubes. *Nature* **391,** 62 (1998).

76. Berber, S., Kwon, Y.-K. & Tománek, D. Unusually high thermal conductivity of carbon nanotubes. *Physical review letters* **84,** 4613 (2000).

77. Monthioux, M. *et al.* in *Springer handbook of nanotechnology* 43–112 (Springer, 2007). (2016).

78. Charlier, J.-C. & Michenaud, J.-P. Energetics of multilayered carbon tubules. *Physical review letters* **70,** 1858 (1993).

79. Saito, R, Matsuo, R, Kimura, T, Dresselhaus, G & Dresselhaus, M. Anomalous potential barrier of double-wall carbon nanotube. *Chemical Physics Letters* **348,** 187–193 (2001).

80. *Nanoethics and Nanotoxicology* en (eds Houdy, P., Lahmani, M. & Marano, F.) (2016) (Springer Berlin Heidelberg, Berlin, Heidelberg, 2011).

81. Karousis, N., Tagmatarchis, N. & Tasis, D. Current Progress on the Chemical Modification of Carbon Nanotubes. en. *Chemical Reviews* **110,** 5366–5397 (Sept. 2010).

82. Chen, Y. *et al.* Light Control of Charge Transfer and Excitonic Transitions in a Carbon Nanotube/Porphyrin Hybrid. en. *Advanced Materials* **29,** 1605745 (May 2017).

83. Tao, L., Chen, G., Mantovani, G., York, S. & Haddleton, D. M. Modification of multi-wall carbon nanotube surfaces with poly(amidoamine) dendrons: Synthesis and metal templating. en. *Chemical Communications,* 4949 (2006).

84. Gul, H., Lu, W., Xu, P., Xing, J. & Chen, J. Magnetic carbon nanotube labelling for haematopoietic stem/progenitor cell tracking. *Nanotechnology* **21,** 155101 (Apr. 2010).

85. Singh, P. *et al.* Polyamine functionalized carbon nanotubes: synthesis, characterization, cytotoxicity and siRNA binding. en. *Journal of Materials Chemistry* **21,** 4850 (2011).

86. Delgado, J. L. *et al.* The first synthesis of a conjugated hybrid of C60–fullerene and a single-wall carbon nanotube. en. *Carbon* **45,** 2250–2252 (Oct. 2007).

87. Lin, Y., Lu, F., Tu, Y. & Ren, Z. Glucose Biosensors Based on Carbon Nanotube Nanoelectrode Ensembles. en. *Nano Letters* **4,** 191–195 (Feb. 2004).

88. Sánchez-Pomales, G., Santiago-Rodríguez, L. & Cabrera, C. R. DNA-functionalized carbon nanotubes for biosensing applications. *Journal of nanoscience and nanotechnology* **9,** 2175–2188 (2009).

89. Pulikkathara, M. X., Kuznetsov, O. V. & Khabashesku, V. N. Sidewall Covalent Functionalization of Single Wall Carbon Nanotubes Through

Reactions of Fluoronanotubes with Urea, Guanidine, and Thiourea. en. *Chemistry of Materials* **20,** 2685–2695 (Apr. 2008).

90. Mickelson, E. *et al.* Fluorination of single-wall carbon nanotubes. *Chemical physics letters* **296,** 188–194 (1998).

91. Liu, M., Yang, Y., Zhu, T. & Liu, Z. Chemical modification of single-walled carbon nanotubes with peroxytrifluoroacetic acid. en. *Carbon* **43,** 1470–1478 (June 2005).

92. Bulusheva, L. G. *et al.* Thermal Behavior of Fluorinated Double-Walled Carbon Nanotubes. en. *Chemistry of Materials* **18,** 4967–4971 (Oct. 2006).

93. Bulusheva, L. G. *et al.* Stability of Fluorinated Double-Walled Carbon Nanotubes Produced by Different Fluorination Techniques. en. *Chemistry of Materials* **22,** 4197–4203 (July 2010).

94. Gaillard, C. *et al.* Carbon Nanotubes Carrying Cell-Adhesion Peptides do not Interfere with Neuronal Functionality. en. *Advanced Materials* **21,** 2903–2908 (July 2009).

95. Samorì, C. *et al.* Enhanced anticancer activity of multi-walled carbon nanotube–methotrexate conjugates using cleavable linkers. en. *Chem. Commun.* **46,** 1494–1496 (2010).

96. Benincasa, M. *et al.* Antifungal Activity of Amphotericin B Conjugated to Carbon Nanotubes. en. *ACS Nano* **5,** 199–208 (Jan. 2011).

97. Zydziak, N., Yameen, B. & Barner-Kowollik, C. Diels–Alder reactions for carbon material synthesis and surface functionalization. en. *Polymer Chemistry* **4,** 4072 (2013).

98. Luksirikul, P., Ballesteros, B., Tobias, G., Moloney, M. G. & Green, M. L. H. Sidewall functionalisation of carbon nanotubes by addition of diarylcarbene derivatives. en. *Journal of Materials Chemistry* **21,** 19080 (2011).

99. Gao, C., He, H., Zhou, L., Zheng, X. & Zhang, Y. Scalable Functional Group Engineering of Carbon Nanotubes by Improved One-Step Nitrene Chemistry. en. *Chemistry of Materials* **21,** 360–370 (Jan. 2009).

100. Yadav, S. K. *et al.* PDMS/MWCNT nanocomposite actuators using silicone functionalized multiwalled carbon nanotubes via nitrene chemistry. en. *Journal of Materials Chemistry C* **1,** 5463 (2013).

101. Dyke, C. A. & Tour, J. M. Overcoming the Insolubility of Carbon Nanotubes Through High Degrees of Sidewall Functionalization. en. *Chemistry - A European Journal* **10,** 812–817 (Feb. 2004).

102. Price, B. K., Hudson, J. L. & Tour, J. M. Green Chemical Functionalization of Single-Walled Carbon Nanotubes in Ionic Liquids. en. *Journal of the American Chemical Society* **127,** 14867–14870 (Oct. 2005).

103. Ménard-Moyon, C., Fabbro, C., Prato, M. & Bianco, A. One-Pot Triple Functionalization of Carbon Nanotubes. en. *Chemistry - A European Journal* **17,** 3222–3227 (Mar. 2011).

104. Baek, Y.-K. *et al.* Label-free detection of DNA hybridization using pyrene-functionalized single-walled carbon nanotubes: effect of chemical structures of pyrene molecules on DNA sensing performance. *Journal of nanoscience and nanotechnology* **11,** 4210–4216 (2011).

105. Salice, P., Gambarin, A., Daldosso, N., Mancin, F. & Menna, E. Noncovalent Interaction between Single-Walled Carbon Nanotubes and Pyrene-Functionalized Gold Nanoparticles in Water-Soluble Nanohybrids. en. *The Journal of Physical Chemistry C* **118,** 27028–27038 (Nov. 2014).

106. Liu, Q. *et al.* Carbon Nanotubes as Molecular Transporters for Walled Plant Cells. en. *Nano Letters* **9,** 1007–1010 (Mar. 2009).

107. Serag, M. F. *et al.* Functional Platform for Controlled Subcellular Distribution of Carbon Nanotubes. en. *ACS Nano* **5,** 9264–9270 (Nov. 2011).

108. Liu, Z., Sun, X., Nakayama-Ratchford, N. & Dai, H. Supramolecular Chemistry on Water-Soluble Carbon Nanotubes for Drug Loading and Delivery. en. *ACS Nano* **1,** 50–56 (Aug. 2007).

109. Liu, Z. *et al.* Supramolecular Stacking of Doxorubicin on Carbon Nanotubes for In Vivo Cancer Therapy. en. *Angewandte Chemie International Edition* **48,** 7668–7672 (Sept. 2009).

110. Tian, Z. *et al.* Supramolecular assembly and antitumor activity of multiwalled carbon nanotube–camptothecin complexes. *Journal of nanoscience and nanotechnology* **11,** 953–958 (2011).

111. Guo, Y. *et al.* In vivo Imaging and Drug Storage by Quantum-Dot-Conjugated Carbon Nanotubes. en. *Advanced Functional Materials* **18,** 2489–2497 (Sept. 2008).

112. Ehli, C. *et al.* Interactions in Single Wall Carbon Nanotubes/Pyrene/Porphyrin Nanohybrids. en. *Journal of the American Chemical Society* **128,** 11222–11231 (Aug. 2006).

113. Iancu, C. *et al.* Enhanced laser thermal ablation for the in vitro treatment of liver cancer by specific delivery of multiwalled carbon nanotubes functionalized with human serum albumin. en. *International Journal of Nanomedicine,* 129 (Jan. 2011).

114. Chen, H., Xi, F., Gao, X., Chen, Z. & Lin, X. Bienzyme bionanomultilayer electrode for glucose biosensing based on functional carbon nanotubes and sugar–lectin biospecific interaction. en. *Analytical Biochemistry* **403,** 36–42 (Aug. 2010).

115. Pang, X., Imin, P., Zhitomirsky, I. & Adronov, A. Amperometric Detection of Glucose Using a Conjugated Polyelectrolyte Complex with

Single-Walled Carbon Nanotubes. en. *Macromolecules* **43,** 10376–10381 (Dec. 2010).

116. Zheng, M. *et al.* DNA-assisted dispersion and separation of carbon nanotubes. *Nature Materials* **2,** 338–342 (Apr. 2003).

117. Cheung, W., Pontoriero, F., Taratula, O., Chen, A. M. & He, H. DNA and carbon nanotubes as medicine. en. *Advanced Drug Delivery Reviews* **62,** 633–649 (Apr. 2010).

118. Neves, V *et al.* Design of double-walled carbon nanotubes for biomedical applications. *Nanotechnology* **23,** 365102 (Sept. 2012).

119. Britz, D. A. & Khlobystov, A. N. Noncovalent interactions of molecules with single walled carbon nanotubes. en. *Chemical Society Reviews* **35,** 637 (2006).

120. Arlt, M *et al.* Delivery of carboplatin by carbon-based nanocontainers mediates increased cancer cell death. *Nanotechnology* **21,** 335101 (Aug. 2010).

121. Feazell, R. P., Nakayama-Ratchford, N., Dai, H. & Lippard, S. J. Soluble Single-Walled Carbon Nanotubes as Longboat Delivery Systems for Platinum(IV) Anticancer Drug Design. en. *Journal of the American Chemical Society* **129,** 8438–8439 (July 2007).

122. Sanz, V. *et al.* Chloroquine-enhanced gene delivery mediated by carbon nanotubes. en. *Carbon* **49,** 5348–5358 (Dec. 2011).

123. Li, R. *et al.* Folate and iron difunctionalized multiwall carbon nanotubes as dual-targeted drug nanocarrier to cancer cells. en. *Carbon* **49,** 1797–1805 (Apr. 2011).

124. Marega, R. *et al.* Functionalized Fe-Filled Multiwalled Carbon Nanotubes as Multifunctional Scaffolds for Magnetization of Cancer Cells. en. *Advanced Functional Materials* **23,** 3173–3184 (July 2013).

125. Alvarez, L. *et al.* High-pressure behavior of polyiodides confined into single-walled carbon nanotubes: A Raman study. en. *Physical Review B* **82.** (2017) (Nov. 2010).

126. Chorro, M. *et al.* 1D-confinement of polyiodides inside single-wall carbon nanotubes. en. *Carbon* **52,** 100–108 (Feb. 2013).

127. Alvarez, L. *et al.* Charge Transfer Evidence between Carbon Nanotubes and Encapsulated Conjugated Oligomers. en. *The Journal of Physical Chemistry C* **115,** 11898–11905 (June 2011).

128. Almadori, Y. *et al.* Chromophore Ordering by Confinement into Carbon Nanotubes. en. *The Journal of Physical Chemistry C* **118,** 19462–19468 (Aug. 2014).

129. Alvarez, L. *et al.* One-Dimensional Molecular Crystal of Phthalocyanine Confined into Single-Walled Carbon Nanotubes. en. *The Journal of Physical Chemistry C* **119,** 5203–5210 (Mar. 2015).

130. Alvarez, L. *et al.* Supramolecular organization of pi-conjugated molecules monitored by single-walled carbon nanotubes. *Journal of Nanophotonics* **10,** 012514–012514 (2016).

131. Belhboub, A. *et al.* Enhancing the Infrared Response of Carbon Nanotubes From Oligo-Quaterthiophene Interactions. en. *The Journal of Physical Chemistry C* **120,** 28802–28807 (Dec. 2016).

132. Pantarotto, D., Briand, J.-P., Prato, M. & Bianco, A. Translocation of bioactive peptides across cell membranes by carbon nanotubesElectronic supplementary information (ESI) available: details of the synthesis and characterization, cell culture, TEM, epifluorescence and confocal microscopy images of CNTs 1, 2 and fluorescein. en. *Chemical Communications,* 16 (2004).

133. Heller, D. A., Baik, S., Eurell, T. E. & Strano, M. S. Single-walled carbon nanotube spectroscopy in live cells: towards long-term labels and optical sensors. *Advanced Materials* **17,** 2793–2799 (2005).

134. Kostarelos, K. *et al.* Cellular uptake of functionalized carbon nanotubes is independent of functional group and cell type. *Nature Nanotechnology* **2,** 108–113 (Feb. 2007).

135. Jin, H., Heller, D. A. & Strano, M. S. Single-Particle Tracking of Endocytosis and Exocytosis of Single-Walled Carbon Nanotubes in NIH-3T3 Cells. en. *Nano Letters* **8,** 1577–1585 (June 2008).

136. Firme, C. P. & Bandaru, P. R. Toxicity issues in the application of carbon nanotubes to biological systems. en. *Nanomedicine: Nanotechnology, Biology and Medicine* **6,** 245–256 (Apr. 2010).

137. Lacerda, L. *et al.* Dynamic Imaging of Functionalized Multi-Walled Carbon Nanotube Systemic Circulation and Urinary Excretion. en. *Advanced Materials* **20,** 225–230 (Jan. 2008).

138. Murphy, F. A. *et al.* Length-Dependent Retention of Carbon Nanotubes in the Pleural Space of Mice Initiates Sustained Inflammation and Progressive Fibrosis on the Parietal Pleura. en. *The American Journal of Pathology* **178,** 2587–2600 (June 2011).

139. Yan, L., Zhao, F., Li, S., Hu, Z. & Zhao, Y. Low-toxic and safe nanomaterials by surface-chemical design, carbon nanotubes, fullerenes, metallofullerenes, and graphenes. en. *Nanoscale* **3,** 362–382 (2011).

140. Jia, G. *et al.* Cytotoxicity of Carbon Nanomaterials: Single-Wall Nanotube, Multi-Wall Nanotube, and Fullerene. en. *Environmental Science & Technology* **39,** 1378–1383 (Mar. 2005).

141. Serag, M. F. *et al.* Trafficking and Subcellular Localization of Multiwalled Carbon Nanotubes in Plant Cells. en. *ACS Nano* **5,** 493–499 (Jan. 2011).

142. Cherukuri, P., Bachilo, S. M., Litovsky, S. H. & Weisman, R. B. Near-Infrared Fluorescence Microscopy of Single-Walled Carbon Nanotubes in Phagocytic Cells. en. *Journal of the American Chemical Society* **126,** 15638–15639 (Dec. 2004).

143. Leeuw, T. K. *et al.* Single-Walled Carbon Nanotubes in the Intact Organism: Near-IR Imaging and Biocompatibility Studies in Drosophila. en. *Nano Letters* **7,** 2650–2654 (Sept. 2007).

144. Robinson, J. T. *et al.* High performance in vivo near-IR (>1 μm) imaging and photothermal cancer therapy with carbon nanotubes. en. *Nano Research* **3,** 779–793 (Nov. 2010).

145. Neves, V. *et al.* Uptake and Release of Double-Walled Carbon Nanotubes by Mammalian Cells. en. *Advanced Functional Materials* **20,** 3272–3279 (Oct. 2010).

146. Wang, R. *et al.* Cytotoxicity Screening of Single-Walled Carbon Nanotubes: Detection and Removal of Cytotoxic Contaminants from Carboxylated Carbon Nanotubes. en. *Molecular Pharmaceutics* **8,** 1351–1361 (Aug. 2011).

147. Kataura, H. *et al.* Optical properties of single-wall carbon nanotubes. *Synthetic metals* **103,** 2555–2558 (1999).

148. Wild, E. & Jones, K. C. Novel Method for the Direct Visualization of in Vivo Nanomaterials and Chemical Interactions in Plants. en. *Environmental Science & Technology* **43,** 5290–5294 (July 2009).

149. Ustione, A. & Piston, D. A simple introduction to multiphoton microscopy. en. *Journal of Microscopy* **243,** 221–226 (Sept. 2011).

150. Lu, F. *et al.* Advances in Bioapplications of Carbon Nanotubes. en. *Advanced Materials* **21,** 139–152 (Jan. 2009).

151. Liu, Z. *et al.* Drug delivery with carbon nanotubes for in vivo cancer treatment. *Cancer research* **68,** 6652–6660 (2008).

152. Klingeler, R., Hampel, S. & Büchner, B. Carbon nanotube based biomedical agents for heating, temperature sensoring and drug delivery. *International journal of hyperthermia* **24,** 496–505 (2008).

153. De Volder, M. F., Tawfick, S. H., Baughman, R. H. & Hart, A. J. Carbon nanotubes: present and future commercial applications. *science* **339,** 535–539 (2013).

154. Flahaut, E., Durrieu, M., Remy-Zolghadri, M., Bareille, R. & Baquey, C. Investigation of the cytotoxicity of CCVD carbon nanotubes towards human umbilical vein endothelial cells. en. *Carbon* **44,** 1093–1099 (May 2006).

155. Bottini, M. *et al.* Multi-walled carbon nanotubes induce T lymphocyte apoptosis. en. *Toxicology Letters* **160,** 121–126 (Jan. 2006).

156. Cheng, J., Flahaut, E. & Cheng, S. H. Effect of carbon nanotubes on developing zebrafish (Danio rerio) embryos. *Environmental Toxicology and Chemistry* **26,** 708–716 (2007).

157. Salvador-Morales, C. *et al.* Binding of pulmonary surfactant proteins to carbon nanotubes; potential for damage to lung immune defense mechanisms. en. *Carbon* **45,** 607–617 (Mar. 2007).

158. Mouchet, F *et al.* Characterisation and in vivo ecotoxicity evaluation of double-wall carbon nanotubes in larvae of the amphibian Xenopus laevis. en. *Aquatic Toxicology* **87,** 127–137 (Apr. 2008).

159. Crouzier, D. *et al.* Carbon nanotubes induce inflammation but decrease the production of reactive oxygen species in lung. en. *Toxicology* **272,** 39–45 (June 2010).

160. Saria, R. *et al.* Short term exposure to multi-walled carbon nanotubes induce oxidative stress and DNA damage in Xenopus laevis tadpoles. en. *Ecotoxicology and Environmental Safety* **107,** 22–29 (Sept. 2014).

161. Bortolamiol, T. *Nanotubes de carbone biparois : fonctionnalisation et détection in vitro* PhD thesis (Université Paul Sabatier, Mar. 2015).

162. Lorne, T. *et al.* Competition between covalent and non-covalent grafting of fluorescein isothiocyanate on double-walled carbon nanotubes: A quantitative approach. en. *Carbon* (2017).

163. Bortolamiol, T. *et al.* Double-walled carbon nanotubes: Quantitative purification assessment, balance between purification and degradation and solution filling as an evidence of opening. en. *Carbon* **78,** 79–90 (Nov. 2014).

164. Lin, Y.-H. *et al.* In vivo MR/optical imaging for gastrin releasing peptide receptor of prostate cancer tumor using Gd-TTDA-NP-BN-Cy5.5. en. *Bioorganic & Medicinal Chemistry* **19,** 1085–1096 (Feb. 2011).

165. Maether, M.-P., Lapin, K., Muntean, A., Payrastre, C. & Escudier, J.-M. Oligonucleotide Labelling Using a Fluorogenic "Click" Reaction with a Hemicarboxonium Salt. en. *Molecules* **18,** 12966–12976 (Oct. 2013).

166. Obaya, N., Payrastre, C. & Madaule, Y. Synthesis of new pentacarbon chain streptocyanines (pentamethinium salts). *Tetrahedron* **57,** 9137–9147 (2001).

167. Squires, G. L. *Introduction to the Theory of Thermal Neutron Scattering* (Courier Corporation, 1978).

168. Lovesey, S. *Theory of neutron scattering from condensed matter* (Clarendon Press, 1984).

169. *Vibrational spectroscopy with neutrons: with applications in chemistry, biology, materials science and catalysis* (ed Mitchell, P. C. H.) *Series on neutron techniques and applications* **vol. 3.** OCLC: ocm61901497 (World Scientific, Hackensack, NJ, 2005).

170. *Neutron physics* eng (eds Koester, L. & Steyerl, A.) *Springer tracts in modern physics* **80.** OCLC: 2954079 (Springer, Berlin, 1977).

171. Ivanov, A., Jimenéz-Ruiz, M. & Kulda, J. IN1-LAGRANGE – the new ILL instrument to explore vibration dynamics of complex materials. *Journal of Physics: Conference Series* **554,** 012001 (Nov. 2014).

172. Lorne, T., Flahaut, E., Jimenéz-Ruiz, M. & Rols, S. *[dataset] Understanding the Grafting of fluorescent molecules on double-walled carbon nanotubes. Institut Laue-Langevin (ILL) doi:10.5291/ILL-DATA.7-05-432* 2015.

173. Lorne, T., Flahaut, E., Jimenéz-Ruiz, M. & Rols, S. *[dataset] Understanding the Grafting of fluorescent molecules on double-walled carbon nanotubes. Institut Laue-Langevin (ILL) doi:10.5291/ILL-DATA.7-05-461* 2016.

174. Parr, R. G. & Weitao, Y. *Density-Functional Theory of Atoms and Molecules* (Oxford University Press, 1989).

175. Sholl, D. S. & Steckel, J. A. *Density functional theory: a practical introduction* OCLC: ocn245025462 (Wiley, Hoboken, N.J, 2009).

176. Zbiri, M. *et al.* Introduction to the density functional formalism and some illustrative applications to magnetism. *Ecole thématique de la Société Française de la Neutronique* **12,** 77–104 (2011).

177. Maradudin, A. A. *Theory of lattice dynamics in the harmonic approximation* (London, Academic Press., 1971).

178. Dove, M. T. *Introduction to lattice dynamics* (Cambridge university press, 1993).

179. Dove, M. Introduction to the theory of lattice dynamics. *?cole th?matique de la Soci?t? Fran?aise de la Neutronique* **12,** 123–159 (2011).

180. Hartree, D. The Wave Mechanics of an Atom with a Non-Coulomb Central Field II: Some Results and Discussion. *Proc. Camb. Phil. Soc* **24,** 111 (1928).

181. Fock, V. Z. Physik, 1930, 61, 126; V. Fock. *Z. Physik* **62,** 795 (1930).

182. Slater, J. C. A simplification of the Hartree-Fock method. *Physical Review* **81,** 385 (1951).

183. Thomas, L. H. The calculation of atomic fields. *Mathematical Proceedings of the Cambridge Philosophical Society* **23,** 542–548 (1927).

184. Fermi, E. A statistical method for determining some properties of the atoms and its application to the theory of the periodic table of elements. *Z. Phys* **48,** 73–79 (1928).

185. Hohenberg, P. & Kohn, W. Inhomogeneous electron gas. *Physical review* **136,** B864 (1964).

186. Kohn, W. & Sham, L. J. Self-consistent equations including exchange and correlation effects. *Physical review* **140,** A1133 (1965).

187. Perdew, J. P., Burke, K. & Erzerhof, M. Generalized Gradiant Approximation Made Simple. *Physical Review Letters* **77** (Oct. 1996).

188. Wang, Y. & Perdew, J. P. Correlation hole of the spin-polarized electron gas, with exact small-wave-vector and high-density scaling. *Physical Review B* **44,** 13298 (1991).

189. Perdew, J. P. & Wang, Y. Pair-distribution function and its coupling-constant average for the spin-polarized electron gas. *Physical Review B* **46,** 12947 (1992).

190. Lee, C., Yang, W. & Parr, R. G. Development of the Colle-Salvetti correlation-energy formula into a functional of the electron density. *Physical review B* **37,** 785 (1988).

191. Becke, A. D. Density-functional thermochemistry. III. The role of exact exchange. en. *The Journal of Chemical Physics* **98,** 5648 (1993).

192. Moulder, Stickle, Sobol & Bomben. *Handbook of X-ray Photoelectron Spectroscopy* (Jill Chastain, 1992).

193. Seah, M. P. & Dench, W. A. Quantitative electron spectroscopy of surfaces: A standard data base for electron inelastic mean free paths in solids. *Surface and interface analysis* **1,** 2–11 (1979).

194. SIEGBAHN, K. Electron spectroscopy for atoms, molecules, and condensed matter. *Physics 1981-1990*, 63 (1993).

195. Hofmann, S. *Auger- and X-Ray Photoelectron Spectroscopy in Materials Science* DOI: 10.1007/978-3-642-27381-0. (2017) (Springer Berlin Heidelberg, Berlin, Heidelberg, 2013).

196. Wagner, C. *et al. NIST Standard Reference Database 20, Version 4.1* 2012. https://srdata.nist.gov/xps/.

197. *BIOVIA Materials Studio 2016* 2016. http://accelrys.com/products/materials-studio/.

198. Agostinelli, E. *et al.* Polyamines: fundamental characters in chemistry and biology. en. *Amino Acids* **38,** 393–403 (Feb. 2010).

199. Marques, M. P. M. & Batistadecarvalho, L. A. E. Vibrational spectroscopy studies on linear polyamines. *Biochemical Society Transactions* **35,** 374–380 (2007).

200. *First general workshop, [held in Torremolinos, near Málaga from 5 - 8 November 1998]* eng (eds Morgan, D. M. L. & Europäische Kommission) (Off. for Off. Publ. of the European Communities, Luxembourg, 2000).

201. Dawidowski, J., Bermejo, F. J. & Granada, J. R. Efficient procedure for the evaluation of multiple scattering and multiphonon corrections in inelastic neutron-scattering experiments. *Physical Review B* **58,** 706 (1998).

202. Dawidowski, J. *et al.* Analysis of multiple scattering and multiphonon contributions in inelastic neutron scattering experiments. *Nuclear Instruments and Methods in Physics Research Section B: Beam Interactions with Materials and Atoms* **195,** 389–399 (2002).

203. Finn, P. & Jolly, W. L. Nitrogen ls binding energies of some azide, dinitrogen, and nitride complexes of transition metals. *Inorganic Chemistry* **11,** 1434–1435 (1972).

204. Ren, W., Li, F., Chen, J., Bai, S. & Cheng, H.-M. Morphology, diameter distribution and Raman scattering measurements of double-walled carbon nanotubes synthesized by catalytic decomposition of methane. *Chemical Physics Letters* **359,** 196–202 (2002).

205. Kearley, G. J., Tomkinson, J. & Penfold, J. New constraints for normal-mode analysis of inelastic neutron-scattering spectra: Application to the HF 2- ion. *Zeitschrift für Physik B Condensed Matter* **69,** 63–67 (1987).

206. Tomkinson, J. & Kearley, G. J. Phonon wings in inelastic neutron scattering spectroscopy: The harmonic approximation. en. *The Journal of Chemical Physics* **91,** 5164–5169 (Nov. 1989).

207. Kearley, G. J. A review of the analysis of molecular vibrations using INS. *Nuclear Instruments and Methods in Physics Research Section A: Accelerators, Spectrometers, Detectors and Associated Equipment* **354,** 53–58 (1995).

208. Tomkinson, J. & Kearley, G. J. The calculation of phonon wing intensities: anisotropic effects. *Nuclear Instruments and Methods in Physics*

Research Section A: Accelerators, Spectrometers, Detectors and Associated Equipment **354,** 169–170 (1995).

209. Dawidowski, J. *et al.* Method of analysis of multiphonon and multiple-scattering effects in inelastic neutron scattering experiments. *Applied Physics A: Materials Science & Processing* **74,** s166–s168 (Dec. 2002).